

**Exploring the Role of HCN1 Pathogenic Variants
in Developmental and Epileptic Encephalopathies:
Insights from *Hcn1*^{G380D} and *Hcn1*^{M142I} Mouse Models**

Inaugural Dissertation

zur

Erlangung des Doktorgrades

Dr. nat. med.

der Medizinischen Fakultät

und

der Mathematisch-Naturwissenschaftlichen Fakultät

der Universität zu Köln

vorgelegt von

Jacquelin Kasemir

aus Waldbröl, Deutschland

Copy Star Copyshop, Köln

2025

Betreuer/in:

Prof. Dr. Dirk Isbrandt

Referent/in:

Prof. Dr. Johannes Vogt

Prof. Dr. Matteo Bergami

Datum der mündlichen Prüfung:

16.01.2025

Contents

Contents	I
List of Figures.....	V
List of Tables	VII
List of Abbreviations	VIII
Abstract (English).....	XI
Abstract (German).....	XIII
1. Introduction	1
1.1 Epilepsy	1
1.2 The hippocampal circuitry in the mouse	1
1.3 Hippocampal oscillations in the mouse brain	3
1.4 Channelopathies	3
1.5 HCN channels	4
1.5.1 HCN1 channel expression.....	6
1.5.2 HCN1 channels and epilepsy	6
1.6 The aim of this study.....	7
2. Materials and Methods.....	8
2.1 Animals and husbandry	8
2.2 Genotyping.....	9
2.2.1 Isolation of mouse DNA	9
2.2.2 Polymerase chain reaction.....	9
2.2.3 Agarose gel electrophoresis	9
2.2.4 DNA enzyme restriction.....	11
2.3 Perfusion and fixation of brain tissue	12

2.4	Slice preparation.....	12
2.5	Survival curves and body weight.....	12
2.6	Behavioral experiments	13
2.6.1	Reflex tests in neonates	13
2.6.2	Open field	14
2.6.3	Elevated plus maze.....	14
2.6.4	Spontaneous alternation in the Y-maze.....	15
2.6.5	Pole test.....	15
2.6.6	Object Recognition and Object Location Memory task.....	15
2.6.7	Contextual Fear Conditioning.....	16
2.6.8	Data collection and analysis of behavioral experiments	16
2.7	Telemetric electrocorticogram recordings.....	17
2.7.1	Implantation of radio transmitters.....	17
2.7.2	Drug testing with radio transmitter-implanted animals.....	18
2.7.3	Data analysis of ECoG recordings.....	18
2.8	<i>In vivo</i> recordings of hippocampal network activity.....	20
2.8.1	Implantation of the head plate.....	20
2.8.2	Data acquisition in the MHC	21
2.8.3	Data analysis of MHC recordings.....	22
3.	Results.....	24
3.1	High mortality rate, reduced body weight, and spontaneous epileptic seizures in GD and MI mice	24
3.2	Reduced firing rate and HCN1 protein expression in hippocampal CA1 pyramidal neurons in GD and MI mice	27
3.3	Behavioral comorbidities in GD and MI mice.....	29

3.3.1	Slight changes in neonatal development of GD mice	29
3.3.2	Locomotor hyperactivity in GD and MI, and motor coordination deficits in GD mice	32
3.3.3	Changes in cognitive functions in GD and MI mice	35
3.3.4	Changes in anxiety-like behavior in GD and MI	37
3.4	Reduced cortical low and high gamma oscillation frequency and power during REM sleep in GD mice	40
3.4.1	Beta oscillation frequency during REM sleep in GD mice	42
3.5	Anti-seizure medications paradoxically induce epileptic seizures in GD and MI mice	43
3.6	Changes in hippocampal gamma oscillations in GD and MI mice	45
3.7	Reduced ripple oscillation frequency and decreased neuron firing rates <i>in vivo</i> in GD mice	50
3.8	Floxed GD mice exhibited spontaneous epileptic seizures comparable to GD mice	53
3.9	Removing the G380D mutation from Gad2 ⁺ interneurons resulted in seizure-free GDGAD mice	55
3.9.1	DeltaFosB immunoreactivity in the hippocampus	57
3.9.2	Reduced cortical low and high gamma oscillation frequency and power during REM sleep in GDGAD mice	59
4.	Discussion	62
4.1	Dysfunctional HCN1 channels result in epileptic seizures	63
4.2	Paradoxical response to anti-seizure medications in both GD and MI mice	64
4.3	Behavioral comorbidities are potentially due to <i>HCN1</i> mutations	65
4.4	Alterations in cortical oscillations in GD mice result from dysfunctional HCN1 channels	66
4.5	Alterations in hippocampal oscillations in GD mice result from dysfunctional HCN1 channels	68

4.6	The HCN1 G380D variant results in an interneuronopathy	70
4.7	Future prospects	72
4.8	Conclusions	74
	References.....	76
	Acknowledgement.....	87
	Statutory Declaration.....	88
	Curriculum Vitae	89

List of Figures

Figure 1: Schematic representation of the basic anatomy of the hippocampus in a mouse brain (from Neves et al., 2008).	2
Figure 2: Schematic structure of HCN channels.	5
Figure 3: Oscillation frequency and power detected by the method <i>fooof</i> .	19
Figure 4: A head-fixed mouse in the Mobile HomeCage (MHC) recorded with different types of silicon probes.	22
Figure 5: High mortality rate, reduced body weight, and spontaneous epileptic seizures in GD and MI mice (modified figure from Merseburg et al., 2022).	26
Figure 6: In CA1 pyramidal neurons, HCN1 protein expression and I_h -dependent voltage sag were diminished in both GD and MI mice (modified figure from Merseburg et al., 2022).	28
Figure 7: Neonatal body weight development of GD mice was slightly impaired.	31
Figure 8: Locomotor hyperactivity in GD and MI, and motor coordination deficits in GD mice.	34
Figure 9: Cognitive functions in GD and MI animals were mildly affected.	36
Figure 10: Changes in anxiety-like behavior in GD and MI mice.	39
Figure 11: Reduced cortical low and high gamma oscillation frequency and power during REM sleep in GD mice.	41
Figure 12: Beta oscillations during REM sleep and a reduced aperiodic exponent during SWS were observed in GD mice.	43
Figure 13: Anti-seizure medications (ASMs) induced epileptic seizures in GD and MI mice (modified figure from Merseburg et al., 2022).	45
Figure 14: Increased low gamma oscillation frequency in stratum lacunosum moleculare (SLM) during movement periods in GD mice.	47
Figure 15: Reduced high gamma oscillation frequency in stratum pyramidale (SP) during immobility in GD mice.	48

Figure 16: Reduced aperiodic exponent during movement and immobility in stratum lacunosum moleculare (SLM) and stratum pyramidale (SP) in GD mice.	49
Figure 17: Reduced ripple frequency oscillations during immobility and decreased neuron firing rates of putative pyramidal neurons (Pyr) in GD mice.	52
Figure 18: FLHGD mice exhibited spontaneous epileptic seizures similar to those observed in GD mice.....	54
Figure 19: GDGAD mice did not exhibit spontaneous epileptic seizures, but still had behavioral comorbidities.	56
Figure 20: DeltaFosB immunoreactivity in hippocampal brain tissue in different mouse models (modified figure from Weber, Bachelor's Thesis, 2024).....	58
Figure 21: Reduced cortical low and high gamma oscillation frequency and power during REM sleep in GDGAD mice, as observed in GD animals.....	60
Figure 22: The aperiodic exponent was not different during SWS in GDGAD mice compared to WT, as observed in GD mice.	61

List of Tables

Table 1: Nucleotide sequences of primers used for PCR and product size in base pairs (bp).....	10
Table 2: Ingredients and their amounts in μl for 50 μl PCR reaction mix.	10
Table 3: PCR programs used for the different mouse lines. Duration is given in seconds (s).	11

List of Abbreviations

ANOVA = analysis of variance
 ASM = anti-seizure medication
 au = arbitrary units
 bp = base pairs
 CA = cornu ammonis
 Ca^{2+} = calcium
 cAMP = cyclic adenosine monophosphate
 CFC = contextual fear conditioning
 cm = centimeter
 CNBD = cyclic nucleotide-binding domain
 DEE = developmental and epileptic encephalopathy
 dNTP = deoxyribonucleotide triphosphate
 DSI = Data Science International
 E/I = excitation/inhibition
 ECoG = electrocorticogram
 EDTA = ethylenediaminetetraacetic acid
 EIEE = early-infantile epileptic encephalopathies
 Emx1 = empty spiracles homeobox 1
 EPM = elevated plus maze
 FW = forward
fooof = fitting-oscillations-and-one-over-f
 GABA = gamma-aminobutyric acid
 Gad2 = glutamate decarboxylase 2
 GD = *Hcn1*^{G380D}
 GEFS+ = generalized epilepsy with febrile seizures-plus
 GFAP = glial fibrillary acidic protein
 H₂O = water

HCl = hydrogen chloride

Hz = hertz

i.p. = intraperitoneal

I_h = hyperpolarizing current

ILAE = International League Against Epilepsy

IPSC = inhibitory postsynaptic current

IPSP = inhibitory postsynaptic potential

ITI = intertrial interval

K^+ = potassium

LANUV = Landesamt für Natur, Umwelt und Verbraucherschutz

LEC = lateral entorhinal cortex

LEV = levetiracetam

LFP = local field potential

LTG = lamotrigine

mA = milliamperes

MEC = medial entorhinal cortex

MI = *HcnI*^{M142I}

mIPSC = miniature inhibitory postsynaptic current

MHC = Mobile HomeCage

Mut = mutant

mV = millivolt

Na^+ = sodium

NaCl = sodium chloride

NDNF⁺ = neuron-derived neurotrophic factor positive

NOEE = neonatal-onset epileptic encephalopathy

NPY = neuropeptide Y

ns = not significant

OF = open field

OLM = object location memory
ORM = object recognition memory
P = postnatal day
PCR = polymerase chain reaction
PHT = phenytoin
PSD = power-spectrum-density
PV+ = parvalbumin-positive
Pyr = pyramidal neurons
REM = rapid eye movement
Rev = reverse
RMP = resting membrane potential
s = seconds
SLM = stratum lacunosum moleculare
SP = stratum pyramidale
SST+ = somatostatin-positive
SWS = slow-wave-sleep
Syt2 = synaptotagmin 2
t = time
T_m = melting temperature
TEA = tris acetate ethylenediaminetetraacetic acid
TLE = temporal lobe epilepsy
UV = ultraviolet
vs. = versus
VIP+ = vasoactive intestinal polypeptide positive
VPA = valproate acid
WFA = *Wisteria floribunda* agglutinin
WT = wild type

Abstract (English)

Developmental and epileptic encephalopathies (DEEs) are a group of severe neurological disorders that start in early life. They are characterized by frequent, often treatment-resistant seizures, and cognitive impairments. These disorders are frequently caused by *de novo* mutations in genes encoding voltage-gated ion channels. Notably, *de novo* mutations in the hyperpolarization-activated cyclic nucleotide-gated non-selective cation channel 1 (HCN1), which influence neuronal excitability, synaptic transmission, and rhythmic activity in neurons, particularly in cortex and hippocampus, have been identified in DEE patients.

Patients with the p.G391D variant in *HCN1* suffer from neonatal-onset epileptic encephalopathy characterized by severe intellectual disabilities, microcephaly, a resistance to anti-seizure medications (ASMs), and early death. Moreover, patients with the p.M153I variant suffer from early-infantile epileptic encephalopathy, displaying milder intellectual disabilities, and ASMs resistance. Two knockin mouse lines, *Hcn1*^{G380D} (GD) and *Hcn1*^{M142I} (MI), were generated, each carrying a heterozygous mutation homologous to those found in human patients.

As shown previously, both GD and MI mice exhibit spontaneous epileptic seizures and locomotor hyperactivity. The current study aimed to further investigate behavioral comorbidities, such as motor coordination deficits, impaired spatial working memory, and altered anxiety behavior, with GD mice exhibiting more severe impairments than MI mice. Administration of ASMs, like lamotrigine or phenytoin, which are sodium channel blockers, induced epileptic seizures in both mouse models – a phenomenon also reported in patients with a pathogenic *HCN1* variant. Interictal electrocorticogram (ECoG) recordings revealed reduced low and high gamma oscillations during rapid eye movement (REM) sleep in GD mice. Additionally, hippocampal CA1 silicon probe depth recordings in awake head-fixed GD mice in the Mobile HomeCage (MHC) showed reduced high gamma oscillations in stratum pyramidale (SP) during immobility and decreased ripple oscillation frequencies. Together, these findings suggest an underlying interneuronopathy in GD animals.

Since HCN1 channels are expressed in the soma and distal dendrites of pyramidal neurons, the G380D mutation leads to reduced HCN1 protein expression in the hippocampus, and *in vitro* studies have shown decreased action potential firing in these neurons. *In vivo* CA1 unit analysis confirmed this finding, demonstrating reduced firing rates of pyramidal neurons in SP. Furthermore, HCN1 is found in axon terminals of parvalbumin-positive (PV+) interneurons. Preliminary results indicated similar

firing rates of these neurons in SP between GD and wild-type (WT) animals but suggested potential feed-forward inhibition deficits.

To further investigate the role of HCN1 dysfunction in interneurons in GD mice, a new mouse line was generated in which the G380D mutation is flanked by loxP sites, allowing the conditional cre recombinase-mediated removal of the disease allele. By using Gad2-cre mice, the GD allele was deleted in all GABAergic neurons. These mice (GDGAD) still show locomotor hyperactivity and attenuated gamma-oscillations during REM sleep but do not exhibit spontaneous epileptic seizures. Together, these findings support our hypothesis and provide conclusive evidence for an interneuronopathy in GD mice.

Abstract (German)

Entwicklungs- und epileptische Enzephalopathien (DEE) sind eine Gruppe schwerer neurologischer Störungen, die im frühen Kindesalter beginnen. Sie sind durch häufige, wiederkehrende und oft therapieresistente epileptische Anfälle gekennzeichnet, wobei auch kognitive Beeinträchtigungen auftreten können. Diese Erkrankungen werden häufig durch *de novo* Mutationen in Genen verursacht, die spannungsgesteuerte Ionenkanäle kodieren. Insbesondere wurden bei einigen DEE-Patienten *de novo* Mutationen im hyperpolarisationsaktivierten, zyklisch-nukleotidgesteuerten unspezifischen Kationenkanal 1 (HCN1) festgestellt, die die neuronale Erregbarkeit, synaptische Übertragung und rhythmische Aktivität von Neuronen im Kortex und im Hippocampus beeinflussen.

Patienten mit der p.G391D-Variante im *HCN1*-Gen leiden an einer neonatalen epileptischen Enzephalopathie, die durch schwere geistige Behinderungen, Mikrozephalie, einer Resistenz gegen antiepileptische Medikamente (ASMs) und einen frühen Tod gekennzeichnet sind. Darüber hinaus gibt es Patienten mit der p.M153I-Variante, welche an einer frühkindlichen epileptischen Enzephalopathie leiden, eine mildere geistige Behinderung haben und ASM-Resistenz zeigen. Um diese Krankheiten näher zu untersuchen, wurden zwei Knock-in Mauslinien – *Hcn1*^{G380D} (GD) und *Hcn1*^{M142I} (MI) – erzeugt, die jeweils eine heterozygote Mutation im *Hcn1* Gen tragen, welche homolog zu den beim Menschen gefundenen Mutationen sind.

Wie bereits gezeigt wurde, weisen sowohl GD- als auch MI-Mäuse spontane epileptische Anfälle und lokomotorische Hyperaktivität auf. Die aktuelle Studie zielt darauf ab, weitere Verhaltenskomorbiditäten wie motorische Koordinationsdefizite, Beeinträchtigungen des räumlichen Arbeitsgedächtnisses und verändertes Angstverhalten weiter zu untersuchen, wobei die Ergebnisse zeigten, dass GD-Mäuse schwerere Beeinträchtigungen aufwiesen als MI-Mäuse. Die Verabreichung von ASMs wie Lamotrigin oder Phenytoin, bei denen es sich um Natriumkanalblocker handelt, löste in beiden Mausmodellen epileptische Anfälle aus – ein Phänomen, welches auch bei Patienten mit einer pathogenen *HCN1*-Variante beobachtet wurde. Aufzeichnungen von interiktalen Elektrokortikogrammen (ECoG) zeigten bei GD-Mäusen reduzierte Gamma-Oszillationen während des REM-Schlafs. Darüber hinaus wurden bei Tiefenaufnahmen des Hippocampus in der CA1-Region stratum pyramidale (SP) bei wachen, kopffixierten GD-Mäusen im Mobile HomeCage (MHC) ebenfalls reduzierte Gamma-Oszillationen während der immobilen Phase festgestellt, sowie

verringerte Ripple-Oszillationen. Diese Ergebnisse deuten auf eine zugrundeliegende Interneuronopathie bei GD-Tieren hin.

Da HCN1-Kanäle im Soma und in distalen Dendriten von Pyramidenzellen exprimiert werden, resultiert die G380D-Mutation in einer verringerten HCN1-Proteinexpression im Hippocampus, und *in vitro*-Studien haben ein verringertes Feuern von Aktionspotenzialen in diesen Neuronen gezeigt. Dies wurde durch weitere Analysen von einzelnen Neuronen *in vivo* bestätigt, welche ebenfalls verringertes Aktionspotential-Feuerverhalten in Pyramidenzellen im SP aufwiesen. Darüber hinaus ist HCN1 in den terminierenden Axonen von parvalbumin-positiven (PV+) Interneuronen zu finden. Vorläufige Ergebnisse deuten darauf hin, dass PV+ Interneurone in GD-Mäusen und in Wildtyp (WT)-Kontrolltieren ein ähnliches Feuerverhalten zeigten, wobei hier mögliche Defizite bei der Feed-Forward-Hemmung vermutet werden.

Um die Rolle der HCN1-Dysfunktion in Interneuronen bei GD-Tieren weiter zu untersuchen, wurde eine neue Mauslinie erzeugt, bei denen die G380D-Mutation von loxP-Seiten flankiert ist, was die konditionale, cre-Rekombinase-vermittelte Entfernung des betroffenen Allels ermöglichte. Durch die Verwendung von Gad2-cre-Mäusen wurde das GD-Allel in allen GABAergen Neuronen entfernt. Diese Mäuse (GDGAD) zeigten weiterhin lokomotorische Hyperaktivität, sowie reduzierte Gamma-Oszillationen im REM-Schlaf, wiesen jedoch keine spontanen epileptischen Anfälle auf. Zusammenfassend unterstützen diese Ergebnisse unsere Hypothese und liefern überzeugende Hinweise auf eine Interneuronopathie bei GD-Mäusen.

1. | Introduction

1.1 | Epilepsy

Epilepsy is a prevalent neurological disorder affecting approximately 4 % of the global population, regardless of age, background, or geographical region. It is characterized by recurrent epileptic seizures caused by abnormal, excessive, or synchronous neuronal activity in the brain. These seizures arise from spontaneous, recurrent, and unprovoked neuronal discharges that disrupt normal brain function (Blumenfeld, 2003; Fisher et al., 2014). The transformation of normal brain tissue to seizure-generating tissue is termed epileptogenesis (Jacobs et al., 2009).

In addition to seizures, epilepsy can lead to significant cognitive, behavioral, and emotional changes, adversely impacting physical and psychological health, and overall the quality of life (Ottman, 1997). Anti-seizure medications (ASMs) have been developed to improve patient outcomes, and these pharmacological treatments help most patients manage their condition. However, approximately one-third of epilepsy patients exhibit a resistance to pharmacotherapy, which is associated with an increased risk of death and injury due to higher seizure frequency (Löscher et al., 2020).

A specific subgroup of epilepsies, known as developmental and epileptic encephalopathies (DEEs), has an early onset – often in childhood or even *in utero* – and frequent seizures that significantly impact cognitive and behavioral functions (Raga et al., 2021). Approximately 30 % of DEE patients have at least one pathogenic mutation in identified genes, many of which are associated with ligand- and voltage-gated ion channels (Noebels, 2017; Wang and Frankel, 2021).

1.2 | The hippocampal circuitry in the mouse

The hippocampus is a critical brain structure that plays a central role in learning, memory, and spatial navigation. It is distinguished by its unique architecture, which includes the subregions cornu ammonis 1 (CA1), CA2, CA3, and the dentate gyrus. Within the CA1 region, there are further subdivisions into the layers stratum oriens, stratum pyramidale, stratum radiatum, and stratum lacunosum moleculare, arranged from apical to distal (Jayet Bray et al., 2010).

Given that the hippocampus is involved in numerous brain functions, maintaining strong connections with other brain structures is essential. The trisynaptic pathway is such a key circuit that connects the entorhinal cortex with the hippocampus, establishing a strong connection. In this pathway, principal cells such as pyramidal neurons and stellate cells in layer II of the medial entorhinal cortex (MEC) connect to the dendrites of granule cells from the dentate gyrus via the perforant pathway. Moreover, mossy fibers from granule cells connect to apical dendrites of pyramidal neurons in CA3. These CA3 pyramidal neurons synapse onto apical dendrites of pyramidal neurons in CA1 via the Schaffer collaterals, completing the trisynaptic loop. Other important pathways connecting the entorhinal cortex with the hippocampus originate from MEC layer III and the lateral entorhinal cortex (LEC) layer III, where they synapse onto distal dendrites of CA1 pyramidal neurons (Neves et al., 2008; Yamamoto and Tonegawa, 2017). Additionally, CA1 pyramidal neurons provide feedback by synapsing onto principal neurons MEC layer V, which in turn modulate neurons in other layers of the entorhinal cortex (Basu and Siegelbaum, 2015; Fig. 1). In some epilepsy studies, structural and morphological abnormalities in the hippocampus are strongly associated with epileptic phenotypes. Furthermore, epileptogenesis is often detected as hippocampal pathophysiology, resulting in epileptic seizures (Nakahara et al., 2018).

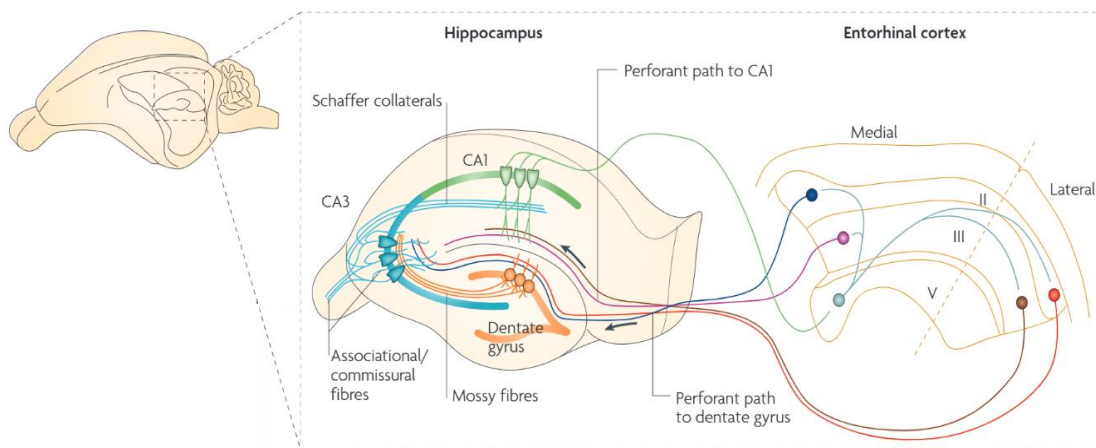


Figure 1: Schematic representation of the basic anatomy of the hippocampus in a mouse brain (from Neves et al., 2008). The hippocampus consists of compartments that include the cornu ammonis 1 (CA1, green), CA3 (blue), and the dentate gyrus (orange). The scheme indicates the trisynaptic loop. In the medial entorhinal cortex (MEC) layer II, neurons project to granule cells of the dentate gyrus. Mossy fibers from granule cells project to CA3 pyramidal neurons, which furthermore project to CA1 pyramidal neurons via Schaffer collaterals.

1.3 | Hippocampal oscillations in the mouse brain

The interaction between hippocampal circuitry and brain oscillations, such as theta and gamma rhythms, are essential for normal brain function. These oscillations, reflected as changes in local field potentials (LFPs), are generated by coordinated and synchronized activity of neurons, facilitating cognitive processes like learning and memory (Colgin, 2016; Etter et al., 2023). Theta oscillations typically have a frequency of 6-9 Hz, while gamma oscillations range from 40-100 Hz. Both theta and gamma oscillations are prominent during active phases in mice, such as movement and exploration, as well as during rapid eye movement (REM) sleep (Buzsáki et al., 2003). In contrast, slow-wave-sleep (SWS) is characterized by slow delta oscillations ranging from 0.5-4 Hz (van Dorp et al., 2024).

In the hippocampal CA1 layer, theta oscillations are in phase within stratum oriens and exhibit a 180° phase reversal in stratum lacunosum moleculare. Notably, faster movements such as running are associated with increased theta frequencies (Buzsáki et al., 2003). Theta-gamma coupling in the hippocampus, that is the modulation of gamma power by slower theta oscillations, is crucial for sorting and processing information, particularly during memory tasks. Theta oscillations are driven by rhythmic excitation by entorhinal cortex afferents, while gamma oscillations depend on the interaction between gamma-aminobutyric acid (GABAergic) inhibitory interneurons and pyramidal cells in CA3 and CA1 (Butler et al., 2018; Colgin and Moser, 2010). Additionally, theta rhythms are generated by the medial septum, which also influences the entorhinal cortex (Buzsáki, 2002). Moreover, in CA1 stratum pyramidale, fast oscillation events known as ripples occur during periods of immobility and SWS. These ripples, with frequencies of 140-200 Hz, are critical for memory consolidation processes (Girardeau et al., 2009). They are generated by synchronic pyramidal neuron firing that drive parvalbumin positive (PV+) interneuron firing. This reciprocal inhibition leads to a unique synchronous phase-locked event (Buzsáki et al., 2003; Schlingloff et al., 2014).

1.4 | Channelopathies

Ion channels are crucial for regulating neuronal excitability in excitable tissues such as the CNS. Mutations in genes encoding for specific ion channels can lead to pathological alterations, such as changes in expression patterns, up- or downregulation of specific channel currents, or abnormal channel function (George, 2004). These alterations are collectively known as channelopathies (Kim,

2014). Dysfunctional ion channels, particularly in neurons, can result in epileptic phenotypes (Bernard and Shevell, 2008; Kim, 2014). Affected ion channels may include voltage-gated sodium (Na^+), potassium (K^+), and calcium (Ca^{2+}) channels, as well as GABA_A receptors (Kullmann, 2002). For instance, loss-of-function mutations in *SCN1A* encoding the $\text{Na}_v1.1$ voltage-gated Na^+ channel are associated with Dravet Syndrome. This disease is characterized by generalized epilepsy with febrile seizures-plus (GEFS+) with an early-onset, prolonged seizures, and cognitive impairments (Catterall, 2018). The epilepsy phenotype is linked to dysfunctional inhibitory interneurons, which is called an interneuronopathy (Catterall, 2018; Incorpora, 2009).

GABA_A receptors are ligand-gated channels that generate a chloride influx upon opening, resulting in synaptic inhibition. Pathogenic variants in genes encoding for GABA_A receptors can result in childhood absence epilepsy with febrile seizures and GEFS+, whereas a loss-of-function mutation contributes to network hyperexcitability and seizures (Lerche et al., 2013; Meisler et al., 2001).

Moreover, alterations in hyperpolarization-activated cyclic nucleotide-gated non-selective cation (HCN) channels have been implicated in pharmacological epilepsy models, further highlighting their role in channelopathies (Dyhrfeld-Johnsen et al., 2009; Merseburg et al., 2022).

1.5 | HCN channels

One distinct family of ion channels is HCN channels. They belong both to the superfamily of voltage-gated K^+ channels and cyclic-nucleotide gated (CNG) channels (Lüthi and McCormick, 1998). HCN channels play a crucial role in regulating rhythmic electrical activity in neurons and cardiac pacemaker cells (Combe and Gasparini, 2021; Depuydt et al., 2022). In mammals, HCN subunits are encoded by four genes (*HCN1-HCN4*). The HCN1-4 subunits can assemble as either homo- or heterotetramers (Fig. 2C). Each subunit contains six transmembrane domains (S1-S6), whereas the S4 domain serves as the positively charged voltage sensor, and S5 and S6 domains form the pore region (Santoro and Shah, 2020). The pore domain includes the K^+ selectivity filter characterized by the glycine-tyrosine-glycine (GYG) motif, which is essential for ion conduction. Upon hyperpolarization of the membrane potential to between -70 to -100 mV, the resulting current I_h (h = hyperpolarization) in neurons allows the conduction of both Na^+ and K^+ ions. The activation upon hyperpolarization results in a channel opening around the resting membrane potential (RMP) of neurons (Huang et al., 2009). During this

process, Na^+ flows into the cell and K^+ flows to the extracellular space, with an ion exchange ratio of 1:3, respectively (Fig. 2A). This ion exchange generates a small depolarizing current due to Na^+ influx along its electrochemical gradient and results in a positive shift of the membrane potential towards action potential firing (Robinson and Siegelbaum, 2003).

Another key feature of HCN channels is their modulation by cyclic nucleotides. This voltage dependent modulation is regulated by the binding of cyclic adenosine monophosphate (cAMP) to the cyclic nucleotide-binding domain (CNBD) located at the carboxy terminus of each subunit. This binding induces conformational changes in the carboxy terminus, increasing the probability of the channel opening (Craven and Zagotta, 2006; Wahl-Schott and Biel, 2009). Moreover, the sensitivity to cAMP modulation varies among the four subunits: HCN1 exhibits the lowest responsiveness to cAMP, HCN2 and HCN4 show the highest responsiveness, and HCN3 is considered cAMP insensitive (Santoro et al., 1998).

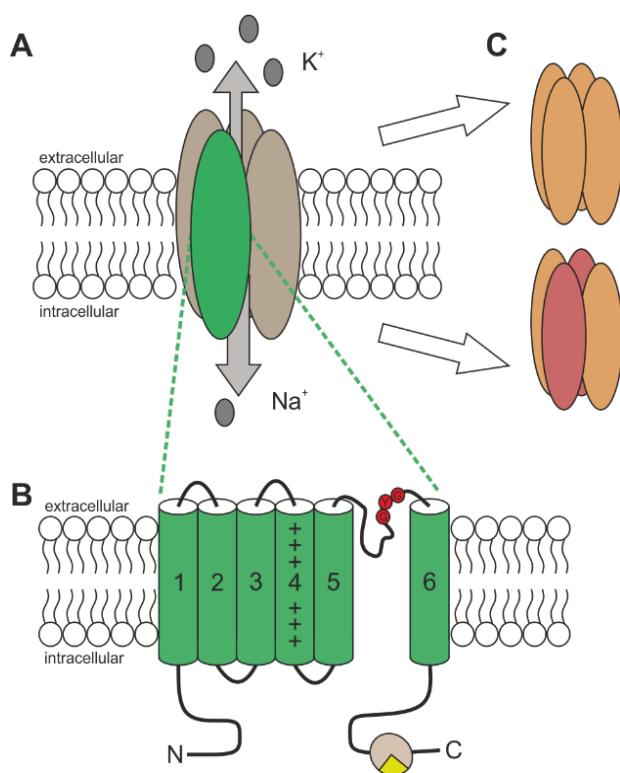


Figure 2: Schematic structure of HCN channels.

A: HCN channels (light grey) located in the cell membrane, consist of four subunits and conduct sodium (Na^+) and potassium (K^+) ions. At hyperpolarized membrane potentials, Na^+ flows in and K^+ out of the cell. **B:** Each subunit consists of six transmembrane domains (S1-S6). The S4 domain comprises of a positively charged voltage sensor. S5 and S6 form the pore and include the glycine-tyrosine-glycine (GYG, red dots) motif responsible for K^+ selectivity. The amino (N) and carboxy (C) termini are located intracellularly. The C-terminus consists of the cyclic nucleotide-binding domain (CNBD, yellow). **C:** Four subunits are arranged into a tetrameric structure, whereas the subunits assemble either into homotetramers composed of one isoform (orange), or into heterotetramers composed of two isoforms (orange, red).

1.5.1 | HCN1 channel expression

The HCN1 subunit is mainly expressed in the central and peripheral nervous system, with a significant presence in neocortex, hippocampus, and cerebellum. Specifically, HCN1 channels are found in pyramidal neurons and PV+ interneurons, also known as basket cells (Santoro and Shah, 2020). In cortex and hippocampus, pyramidal neurons express HCN1 channels both at the soma and in distal dendrites, with an HCN1 density in the dendrites that is seven times greater than at the soma (Gasparini and DiFrancesco, 1997; Lörincz et al., 2002). In PV+ basket cells, the expression of HCN1 channels is limited to axonal terminals (Bock et al., 2022; Notomi and Shigemoto, 2004). In the MEC, HCN1 subunits are co-expressed with T-type Ca^{2+} channels ($\text{Ca}_v3.2$) in axonal terminals that synapse onto layer III neurons. Within these synaptic terminals, the HCN1-mediated depolarizing current I_h inhibits T-type Ca^{2+} channel activity, thereby reducing glutamate release (Huang et al., 2017, 2011). Additionally, in layer II of the MEC, stellate cells projecting to the dentate gyrus express HCN1 channels in their axonal terminals (Bender et al., 2007; Nolan et al., 2007). In the cerebellum, HCN1 is expressed in Purkinje neurons, which are responsible for the major output of the cerebellar cortex through their GABAergic inhibitory function. Here, the axon initial segment of Purkinje neurons is surrounded by axonal terminations of PV+ basket cells, forming a structure known as the “pinceau”, where HCN1 channels are concentrated (Southan et al., 2000; Zhou et al., 2020).

1.5.2 | HCN1 channels and epilepsy

In the last years, the connection between epilepsy and altered HCN1 function has gained increasing attention. For example, in temporal lobe epilepsy (TLE) patients – a condition characterized by unprovoked seizures originating in the temporal lobe and predominantly observed in adults – a reduction of the HCN1-mediated current I_h was observed in neocortical neurons. Notably, I_h density values were further reduced with increasing seizure frequency (Bender et al., 2003; Wierschke et al., 2010). Furthermore, a study of Dravet syndrome patients identified six unrelated patients with a *de novo* mutation in *HCN1* instead of the typical *SCN1A* mutation. These patients exhibited early-onset DEE, impaired cognition and motor skills, as well as paradoxical responses to ASMs (Nava et al., 2014).

The growing interest in *HCN1* mutations and their role in epilepsy has led to the identification of additional *de novo* mutations in human patients. The p.Gly391Asp (G391D) variant – located at the S6 transmembrane domain – is of particular interest. This *de novo* mutation was found in two unrelated patients with neonatal-onset epileptic encephalopathy (NOEE), characterized by a seizure onset within a few hours after birth, daily tonic and prolonged seizures, severe intellectual disabilities, microcephaly, and a resistance to ASMs. Another pathogenic variant, p.Met153Ile (M153I), located at the S1 domain was identified in two unrelated patients with early-infantile epileptic encephalopathies (EIEE) with a seizure onset at five and nine months, weekly focal and tonic-clonic seizures, mild intellectual disabilities, and ASM resistance (Marini et al., 2018). Thus, pathogenic variants in *HCN1* alter HCN1 channel function and result in therapy-resistant epilepsy phenotypes with a clinical presentation overlapping with Dravet syndrome.

1.6 | The aim of this study

This study aims to analyze two knockin mouse lines generated by the CRISPR/Cas9 technique. Each mouse line carries a human point mutation in the gene encoding for HCN1 channels. Mice with the human point mutation G391D are referred to as *Hcn1*^{G380D} (GD), while those with the human point mutation M153I are referred to as *Hcn1*^{M142I} (MI). My previous research already revealed that both GD and MI mice exhibit spontaneous epileptic seizures, high mortality rates, reduced body weights, and behavioral comorbidities such as locomotor hyperactivity and altered gait (Kasemir, Master's thesis, 2020). This study focuses on further analyzing their behavior, particularly concerning motor coordination, memory, and anxiety. Additionally, the aim is to investigate cortical and hippocampal brain oscillations to understand how altered HCN1 channel function and epileptic seizures affect these networks. By generating a conditional GD mouse line, it was possible to selectively remove the G380D mutation in a neuron type-specific manner. This approach is used to assess how the phenotype reflects the human disorder and whether this disease can be restricted to specific neuron types to identify the cause of this type of epilepsy.

2. | Materials and Methods

2.1 | Animals and husbandry

Animals (mice, *Mus musculus*) were kept in type II long plastic cages. They lived under standard housing conditions, including a temperature of $21 \pm 2^\circ\text{C}$, around 50 % relative humidity, and water and rodent chow *ad libitum* (*ssniff Spezialitäten GmbH*, Germany). Mice were transferred to clean cages every week and kept in an inverted 12:12 dark light cycle, with light turning on at 10 pm.

All mice used for this study were maintained on a C57BL/6J background. Based on *de novo* point mutations found in human patients (p.G391D and p.M153I; Marini et al., 2018), the two mouse lines *HcnI*^{G380D} (further referred to as GD) and *HcnI*^{M142I} (further referred to as MI) carrying the corresponding heterozygous human point mutation were generated using the CRISPR/Cas9 technique (Merseburg et al., 2022; Tröder et al., 2018).

To study the GD mouse line and the corresponding point mutation in more detail, a new mouse line called *HcnI*^{(G380D)loxP/+} (further referred to as FLHGD) was generated. Here, the G380D mutation was flanked by loxP sites, which serve as recognition sequences for the cre-recombinase enzyme. With this enzyme, it was possible to remove the G380D mutation from specific neuron types. Because FLHGD mice seemed to have an even higher mortality rate than GD mice, they received 100 mg/kg levetiracetam (LEV; *Sun Pharmaceutical Industries Europe BV*, Netherlands) in their drinking water to reduce epileptiform spiking activity (Bleakley et al., 2023).

Crossing FLHGD male mutant mice with glutamate decarboxylase 2 (Gad2)-cre female mice (Strain #:010802, *Gad2*^{tm2(cre)Zjh}/J, *The Jackson Laboratory*) resulted in a cell specific deletion of the G380D mutation in all Gad2+ interneurons. This new mouse line was designated as GDGAD (*HcnI*^{(G380D)loxP/+}, Gad2-cre). Since FLHGD male mutants, pregnant Gad2-cre females, and their litters received LEV in their drinking water (to continue treating FLHGD offspring with LEV), GDGAD mice were also treated with LEV until they were approximately six weeks old. After confirming the genotype, GDGAD animals received normal drinking water.

Wild type (WT) littermates without a mutation from GD, MI, FLHGD, and GDGAD were used in this study as control animals. All experiments were approved by the Landesamt für Natur, Umwelt und Verbraucherschutz (LANUV) North Rhine-Westphalia, Germany.

2.2 | Genotyping

2.2.1 | Isolation of mouse DNA

DNA isolation was conducted from ear biopsies. Biopsies were lysed in 100 µl lysis buffer (100 mM NaCl, 50 mM Tris/HCl pH 8.0, 1 mM EDTA, 0.2 % Nonidet P-40, 0.2 % Tween 20, 0.1 mg/ml Proteinase K). The lysis was carried out at 54°C overnight under constant shaking, followed by 45 minutes at 85°C to inactivate Proteinase K.

2.2.2 | Polymerase chain reaction

To genotype the animals, a polymerase chain reaction (PCR) was performed. The sequences of the primers used for each mouse line are listed in Table 1. The reaction mix contained a volume of 50 µl per tube, with specific amounts of different ingredients listed in Table 2. The PCR reactions were executed in a thermoblock (*Biometra Trio AnalytikJena*, Germany) according to the programs specified in Table 3. The hybridization temperature was adjusted to the expected melting temperature (T_m) of the primers.

2.2.3 | Agarose gel electrophoresis

For agarose gel electrophoresis, 1.8 % agarose gels were prepared with agarose powder (*VWR life science, Sigma-Aldrich*, Germany) dissolved in 1x TAE buffer (40 mM Tris, 10 mM acetic acid, 1 mM EDTA pH 8.0). Following PCR reaction, 15 µl of the product mixed with loading dye was loaded into wells of the agarose gel, along with 5 µl DNA PANladder I (100 bp, *PAN-BiotechTM*, Germany), and electrophoretically separated in 1x TAE buffer at 135 V.

Table 1: Nucleotide sequences of primers used for PCR and product size in base pairs (bp).

Mouse line	PCR	Primer	Primer sequence	Product size
GD	WT	G380D WT FW G380D WT Rev	5' – ACGGTGATGACACTTGTTTCAGT – 3' 5' – TGGATCAAAGCTGTGGCATGGC – 3'	468 bp
	Mut	G380D Mut FW G380D Mut Rev	5' – ACCTGCTACGCAATGTTTGTTGAT – 3' 5' – GGCACTACACGCTAGGAA – 3'	354 bp
MI	WT	HCN1 FW3 HCN1 Rev4	5' – CAA CAT TTG TTT GTT CTC CTC ACC – 3' 5' – ATG ATC GAA TGC CAC GTT GA – 3'	248 bp
FLHGD	WT	GDFL FW1 GDFL Rev1	5' – TCC GTG AAC CCA CCT TCT AC – 3' 5' – CCT GAT GCC ACC TCT CAA AT – 3'	1032 bp
	loxP	GDFL FW2 GDFL Rev2	5' – GTT CAG TAA TCC CAA TAA CTT CG – 3' 5' – GAT TGG GCA CTA CAC ATA ACT TC – 3'	836 bp
	Mut	G380D Mut FW HCN1 Rev2	5' – ACC TGC TAC GCA ATG TTT GTT GAT – 3' 5' – TGG AAC CTG AAC CGT AGT AAC ACC – 3'	621 bp
Gad2-cre	Gad2	Gad2 FW Gad2 Rev	5' – CTT CTT CCG CAT GGT CAT CT – 3' 5' – CAC CCC ACT GGT TTT GAT TT – 3'	250 bp
	cre	cre FW cre Rev	5' – GCA GCT AAA CAT GCT TCA TC – 3' 5' – GCT AAG TGC CTT CTC TAC ACC – 3'	365 bp

Table 2: Ingredients and their amounts in µl for 50 µl PCR reaction mix.

Ingredients	Amount [µl]
10x PCR Buffer	5.0
dNTPs (25 mM)	0.5
Taq-Polymerase	0.25
FW primer (20 pmol)	0.5
Rev primer (20 pmol)	0.5
DNA template (diluted 1:5)	2.0
H ₂ O	41.25

Table 3: PCR programs used for the different mouse lines. Duration is given in seconds (s).

Mouse line	Cycle	Step description	Temperature and duration					
GD	1	initial denaturation	<u>WT and Mut</u>					
		denaturation	95°C	3 min				
	2 – 9	annealing	94°C	30 s				
		elongation	71°C	45 s				
	10 – 45	denaturation	72°C	45 s				
		annealing	94°C	30 s				
MI	2 – 9	annealing	64°C	45 s				
		elongation	72°C	45 s				
	10 – 45	denaturation	94°C	30 s				
		annealing	64°C	45 s				
	46	elongation	72°C	45 s				
		final elongation	72°C	5 min				
FLHGD	1	initial denaturation	<u>WT and Mut</u>					
		denaturation	95°C	6 min				
	2 – 10	annealing	94°C	30 s				
		elongation	62°C	30 s				
	11 – 46	denaturation	72°C	30 s				
		annealing	94°C	30 s				
Gad2-cre	11 – 46	annealing	54°C	30 s				
		elongation	72°C	30 s				
	47	final elongation	72°C	5 min				
	1	initial denaturation	<u>WT</u>					
		denaturation	95°C	3 min	<u>loxP</u>	95°C	3 min	<u>Mut</u>
FLHGD	2 – 10	annealing	94°C	30 s	94°C	30 s	94°C	30 s
		elongation	62°C	1 min	71°C	1 min	72°C	1 min
	11 – 46	denaturation	72°C	1 min	72°C	1 min	72°C	45 s
		annealing	94°C	30 s	94°C	30 s	94°C	30 s
	47	annealing	54°C	1 min	61°C	1 min	64°C	1 min
		elongation	72°C	1 min	72°C	1 min	72°C	45 s
Gad2-cre	47	final elongation	72°C	10 min	72°C	10 min	72°C	10 s
	1 (1)	initial denaturation	<u>Gad2</u>					
		denaturation	95°C	5 min	<u>cre</u>	95°C	5 min	
	2 – 12 (2 – 36)	annealing	94°C	30 s	94°C	30 s		
		elongation	64°C	30 s	55°C	45 s		
Gad2-cre	13 – 43	denaturation	72°C	30 s				
		annealing	94°C	30 s				
	44 (37)	elongation	54°C	30 s				
		final elongation	72°C	30 s	72°C	30 s		
	44 (37)	final elongation	72°C	5 min	72°C	5 min		

2.2.4 | DNA enzyme restriction

For the MI mouse line, genotype identification included enzyme restriction of the PCR product. Enzyme restriction was performed with the DpnII enzyme (*New England Biolabs*[®], Germany). This enzyme cut at the base pair sequences *GATC*, which was found in the genome of heterozygous MI animals due to the mutation. For a 30 µl reaction mix, 1 µl DpnII enzyme, 3 µl DpnII buffer, 10 µl DNA and 16 µl H₂O were used and incubated at 37°C for two hours. The product was mixed with loading dye and gel electrophoresis was performed as described before (2.2.3). Results that showed

two bands in the gel indicated that the enzyme was active and that those mice carry the heterozygous MI mutation.

2.3 | Perfusion and fixation of brain tissue

To perform fixation of brain tissue, animals were first anesthetized via intraperitoneal (i.p.) injection of 10 µl/g bodyweight ketamine-xylazine solution (12 % Ketanest, 8 % Sedaxylan in 0.9 % NaCl solution). When mice stopped responding to pain stimuli such as pinching of the hind paws, they were fixed on their back onto a Styrofoam board. A thoracotomy was performed to expose the heart. A 25-gauge cannula connected to the perfusion system was inserted into the left ventricle, and the right atrium was perforated with sharp scissors. The animal was perfused with 100 ml of 1 x phosphate buffered saline (PBS), which was pumped into the heart via the cannula, followed by around 50 ml of 4 % paraformaldehyde (PFA) solution (*Roti® Histofix 4 %*, Roth). Afterwards, animals were decapitated, their brains were carefully removed and stored in 4 % PFA for 24 hours at 4°C. On the next day, the solution was replaced by 1 x PBS and stored at 4°C for further use.

2.4 | Slice preparation

For sagittal sectioning of mouse brains, one hemisphere was cut with a vibratome (*Leica Biosystems*, Germany) into 40 µm slices. Brain slices were then mounted onto microscope slides (*SuperFrost® Plus*, *Thermo Fisher Scientific*, USA) and dried for approximately 30 minutes. They were embedded in DAPI Fluoromount-G® (*SouthernBiotech*, USA) and covered with a coverslip (*Carl Roth®*, Germany).

2.5 | Survival curves and body weight

Survival curves of mice were analyzed with the help of the online animal facility software PyRAT® (*Scionics Computer Innovation GmbH*, Germany) for the different mouse lines. WT littermates were used as control animals. The results were illustrated in a survival graph, where the age in weeks was plotted against the probability of survival in percent. Each tic illustrates a death, either due to the end

of the experiment (scored as 0) or due to sudden death (scored as 1), whereby a sudden death had an impact in the survival rate, decreasing the number. The following number of animals was used in a previous study (Kasemir, Master's thesis, 2020): WT GD male (96), GD male (55), WT GD female (56), GD female (66), WT MI male (45), MI male (43), WT MI female (44), MI female (39).

Body weights in grams (g) of mice were collected by the animal care takers. GDGAD mice were weighted once upon weaning at postnatal day (P) 28 and the data was saved in PyRAT. Body weight data from other mouse lines were previously conducted and the following number of animals was used in a previous study (Kasemir, Master's thesis, 2020): WT GD male (42), GD male (30), WT GD female (33), GD female (24), WT MI male (19), MI male (22), WT MI female (30), MI female (23).

2.6 | Behavioral experiments

All behavioral experiments were performed during the dark phase of the light cycle, the time during which mice are active. At the time of behavioral testing, neonatal mice were between P2 and P8, and adult mice were between 8 and 20 weeks old.

2.6.1 | Reflex tests in neonates

Reflexes were tested in neonates from P2 to P8 and included the righting reflex, the cliff avoidance reflex, and the geotactic reflex. Each reflex test was repeated twice with an intertrial interval (ITI) of 30 seconds. The cliff avoidance test was performed by placing the pup on a raised platform approximately 10 cm high, with its head and front paws at the edge of the platform. Successful avoidance of the edge was indicated by the body turning approximately 90°, directing the head and front paws away from the edge. The righting reflex assessed the pup's ability to turn from a supine position to the normal prone position. The test was considered successful after the animal turned to the prone position and all four paws were touching the ground. For the geotactic reflex test, the pup was placed onto an inclined plexiglass plate (35°) with its nose facing downwards, testing its ability to turn 180° facing upwards. For all tests, the maximum trial duration was 30 seconds, whereby a failure was noted at 30 seconds, due to either pup taking longer than 30 seconds or failing to perform the task. The

analysis included the latency to successfully end the task and mean and standard error of the mean (SEM) of the two trials were plotted.

2.6.2 | Open field

The open field test was used to characterize locomotion, exploration, and risk-assessment behavior. The experimental arena was a brightly illuminated (100 lux) box (50 x 50 x 40 cm). The adult mouse was placed into the arena facing one corner of the box and was allowed to move freely for 15 minutes. Tracks were video-recorded and analyzed using the tracking-system EthoVision XT 16 (*Noldus*, The Netherlands). The arena was divided into a border area (imaginary 5 cm wide border at the inside wall of the box) and a center area (imaginary 20 x 20 cm square in the middle of the box). The different parameters, such as locomotor activity, velocity, and occupation ratio (time (t) center subtracted by time in border divided by time in center plus time in border $(t_{\text{center}} - t_{\text{border}})/(t_{\text{center}} + t_{\text{border}})$) were obtained with EthoVision XT 16.

2.6.3 | Elevated plus maze

The elevated plus maze (EPM) test was performed to measure anxiety-like behavior. The EPM consisted of four arms arranged as a cross (30 x 5 cm, 75 cm high), with a 5 x 5 cm center area in the middle. Two opposing arms were open on both sides and at the outer edges (open arms, OA), while the other two arms were enclosed on both sides and at the outer edge by a 17 cm high wall (closed arm, CA). The mouse started in the center area facing an OA and moved freely in the arena for five minutes. The animal was tracked with the software EthoVision XT 16, and parameters included the cumulative duration in OAs vs. CAs, and the arm preference (time in OA subtracted by time in CA divided by time in OA plus time in CA $(t_{\text{OA}} - t_{\text{CA}})/(t_{\text{OA}} + t_{\text{CA}})$) for the first three minutes of the task.

2.6.4 | Spontaneous alternation in the Y-maze

The Y-maze was used to investigate spatial short-term memory, considering a rodent's natural tendency to explore new environments. The arena was a Y-shaped maze consisting of three equally sized arms (34 x 5 x 30 cm) and was dimly illuminated (10 lux). The mouse was placed in the center of the maze, which connects the three arms (A, B, and C). It was allowed to move freely for a maximum duration of 15 minutes or until it completed 24 arm visits. An entry into any arm was considered as a transition. Alternation behavior was defined as consecutive entries into all three arms without repeated entries and was expressed as a percentage of total arm entries.

2.6.5 | Pole test

This experiment assessed motor coordination of the animals. The mouse was positioned at the tip of a vertical wooden pole (60 cm long, 7 mm diameter) and had to rotate 180° and climb down the pole using all four paws. The pole was divided into three sections, with a turn in the first two sections of the pole being considered a success, whereas a turn at the lower section was considered a failure in completing the task. Additionally, the task was considered unsuccessful, when the mouse was not climbing down but sliding down or falling from the pole. Three repetitions were conducted with an ITI of 30 seconds and the time needed for completing the task was measured.

2.6.6 | Object Recognition and Object Location Memory task

These tests aim to investigate spatial long-term memory of the animals. The experimental area consisted of a box (50 × 50 × 40 cm) illuminated with 100 lux. To provide orientation, distal cues were placed outside the arena. Before training, mice were acclimated to the box for five minutes. Subsequently, around one hour later, mice returned to the box for the training session in the presence of two identical objects, allowing them to freely explore until they reached a total object interaction time of 20 seconds, or a maximum trial duration of 15 minutes. Mice that explored the objects for less than 20 seconds during the 15-minute training period were excluded. Twenty-four hours after the training session, mice were placed back into the box with two objects. For the object recognition memory (ORM) test, one object was replaced with a new object, while maintaining the same positions

as during the training session. For the object location memory (OLM) test, one of the two familiar objects from the training session was moved to a different position. The decision on which object to replace or move was randomized and balanced. Additionally, for OLM, besides the distal cues outside the arena, intra-maze cues were used. Different objects were selected for each test (blue boxes and magic cube for ORM, screw-top jars for OLM). Throughout the entire experiment, animal behavior was tracked using EthoVision XT 16. Object interaction was quantified as the time the mouse's nose was within 2 cm of the object. Relative exploration times in seconds were expressed as a discrimination index, meaning time spend at the new/moved object subtracted by the time spent at the familiar object divided by the time spend at the new/moved object plus time spent at the familiar object ($(t_{\text{new/moved}} - t_{\text{familiar}})/(t_{\text{new/moved}} + t_{\text{familiar}})$).

2.6.7 | Contextual Fear Conditioning

The contextual fear conditioning (CFC) experiment investigated learning the association between an unconditioned stimulus (electric shock) and a conditioned stimulus (context). A novel environment served as a context, which was a chamber constructed of plexiglass walls (23.5 x 23.5 x 19.5 cm), illuminated with 8 lux, and with a metal grid floor from which an electric shock was administered. Initially, mice were placed into the chamber and allowed to explore for 120 seconds. Electric shocks (0.35 mA with a duration of one second) were administered at intervals of 120, 160, and 200 seconds. Conditioning was concluded after a total of 240 seconds. To assess memory recall and the association of the electric shock with the context, animals were placed back into the chamber 24 hours later. Here, the time during which mice remained in absolute immobility (minimum one second, referred to as freezing time) was measured using the EthoVision XT 16 software.

2.6.8 | Data collection and analysis of behavioral experiments

Experimental set-up illustrations were performed using BioRender (*Science Suite Inc.*, Canada). Graph visualization of data and statistical analysis were performed with GraphPad Prism 10 (*GraphPad Software*, USA). The comparison of two groups was performed with the nonparametric Mann-Whitney *U* test. Repeated measurements were analyzed with a two-way analysis of variance

(ANOVA). Before-after plots were analyzed with a parametric paired t -test. All tests were two-tailed, and significance levels were denoted by one to three asterisks (* $p \leq 0.05$, ** $p \leq 0.01$, *** $p \leq 0.001$). Unless otherwise stated, data points without asterisks or labeled as “ns” indicate non-significant differences ($p > 0.05$). Data are represented as scatter dot plots with mean \pm SEM. For ORM and OLM, before-after plots with symbols and lines were used. Success rates in percent (%) are indicated with bar plots including the mean. Latencies in seconds (s) are indicated as mean \pm SEM. From a previous study (Kasemir, Master’s thesis, 2020), the following number of animals was included in the analysis for OF: WT GD (13), GD (10), WT MI (12), MI (12).

2.7 | Telemetric electrocorticogram recordings

2.7.1 | Implantation of radio transmitters

For telemetric electrocorticogram (ECoG) recordings, adult mice (age eight to 24 weeks) were implanted with radio transmitters (model ETA-F10, weight approximately 1.6 g, *Data Science International* (DSI), USA). Approximately 30 minutes before surgery, mice received the analgesic buprenorphine (0.0125 mg/kg_{body weight}) via i.p. injection. Mice were pre-anesthetized with 4 % isoflurane in 100 % oxygen. The animal was placed on a heating pad, body temperature was monitored with a rectal probe and maintained at 37°C. The animal’s head was fixed in a stereotaxic frame and isoflurane was decreased to 1.8 % in 100 % oxygen. After shaving the fur of the head and disinfecting the skin, a medial skin incision was performed to expose the skull. The skullcap was cleaned with a cotton swab and hardened with dental cement (*OptiBondTM*, Kerr Dental, Germany) and ultraviolet (UV)-light. Using a dental drill, a hole was made above the dorsal hippocampus (2 mm lateral and 2 mm caudal from bregma), where the recording electrode was placed. Another hole was drilled above the cerebellum (1 mm posterior from lambda and 1-3 mm lateral to the midline) for the reference electrode (diameter 0.6 mm). The electrode wires were placed inside the holes and fixed with dental glue (*Tetric EvoFlow*, *M+W Dental*, Germany). The radio transmitter was implanted subcutaneously in a pouch on the back of the animal. At the end of surgery, the skin was closed using the tissue glue *GLUture®* (*World Precision Instruments (WPI)*, USA). After surgery, the animal received 5.0 mg/kg_{body weight} of the analgesic carprofen (*Norbrook® Laboratories Limited*, Ireland) subcutaneously. Animals were allowed to recover from surgery for five days, during which they were

scored daily. Transmitters were turned on with a magnet. Animals were placed in their home cages onto a receiver board, which was used to detect the ECoG signal, motor activity, as well as synchronized video recordings.

2.7.2 | Drug testing with radio transmitter-implanted animals

To test ASMs in animals implanted with radio-transmitters, the anticonvulsive drugs lamotrigine (LTG) and phenytoin (PHT), which are sodium channel blockers, were used. LTG (*Sigma-Aldrich*, Germany) powder was dissolved in 0.9 % NaCl and administered via i.p. injection at a dose of 23 mg/kg_{body weight}. For PHT (Phenhydan, *Desitin*, Germany) injection, the drug was diluted in 21 % cyclodextrin in 1 x PBS, pH was adjusted to 8.0, and mice were injected with a dose of 30 mg/kg_{body weight}. As a control, mice were also injected with vehicle (0.9 % NaCl) one week before or after ASM injection. The ECoG signal and the synchronized video were monitored for each mouse for at least 24 hours post-injection. The responses to each ASMs were scored using a modified Racine's scale and plotted in a diagram. Three out of four GD mice and four out of seven MI mice had been injected once with LTG, and after one week, they received an injection of PHT. In addition to the injections performed in Prof. Isbrandt's laboratory, several LTG and PHT injections were conducted in Prof. Siegelbaum's laboratory at Columbia University, New York, NY. Besides LTG and PHT, a group of mice was injected with sodium valproate (VPA; 250 mg/kg_{body weight} valproic acid, sodium salt, *Tocris*, UK) dissolved in 0.9 % NaCl. In these experiments at Prof. Siegelbaum's laboratory, no ECoG recordings were performed, and seizure stages were noted by the experimenter using a modified Racine's scale.

2.7.3 | Data analysis of ECoG recordings

The implantation of radio transmitters allowed a continuous recording of the ECoG signal and the behavior in the home cage over several days (6-12 days). Telemetric ECoG signals together with synchronized video recordings were acquired and saved using Ponemah (*DSITM*, USA) and the Media Recorder (*Noldus 4.0*, The Netherlands). With the software NeuroScore (*DSITM*, USA), the recordings were visualized, and epileptic seizures were detected using an automated spike detection tool (absolute

threshold: threshold value 200 μV , maximum value 2000 μV ; spike duration: 0.1-250 ms) and manually verified by the experimenter. Visualization of the seizures was performed with a custom script in MATLAB[®] (*The MathWorks*, USA).

With the help of the video recordings, it was possible to grade the behavior of the mouse during a seizure using a modified Racine's scale (Van Erum et al., 2019). The following values were used for scoring: 0 = normal behavior, 1 = mouth and facial movements, 2 = head nodding, 3 = forelimb clonus, 4 = rearing with forelimb clonus/falling, 5 = wild running and jumping, and 6 = laying on the side with fore- and hindlimb clonus. For the analysis, the highest stage of an individual seizure was plotted. For seizure quantification, the following number of animals was already used in a previous study (Kasemir, Master's thesis, 2020): GD (3), MI (9).

For analyzing the interictal activity of animals, 24-hour recordings with baseline activity of each mouse were exported from NeuroScore via edf-files. From this file, periods of REM sleep, SWS, and active periods (ACTIVE) were investigated using spectral analysis and additionally, multitaper spectra were computed using the Chronux toolbox (www.chronux.org). ACTIVE included periods of wakefulness with movements as well as immobility. Power-spectrum-density (PSD) plots were generated for REM, SWS and ACTIVE periods with custom-written MATLAB[®] scripts. To quantify identified differences from the power spectra analysis of recorded mice for the three different brain states (REM, SWS, ACTIVE), the MATLAB[®] function 'findpeaks' was used to detect frequency peaks and their amplitude after subtracting a fit of the 'aperiodic exponent'.

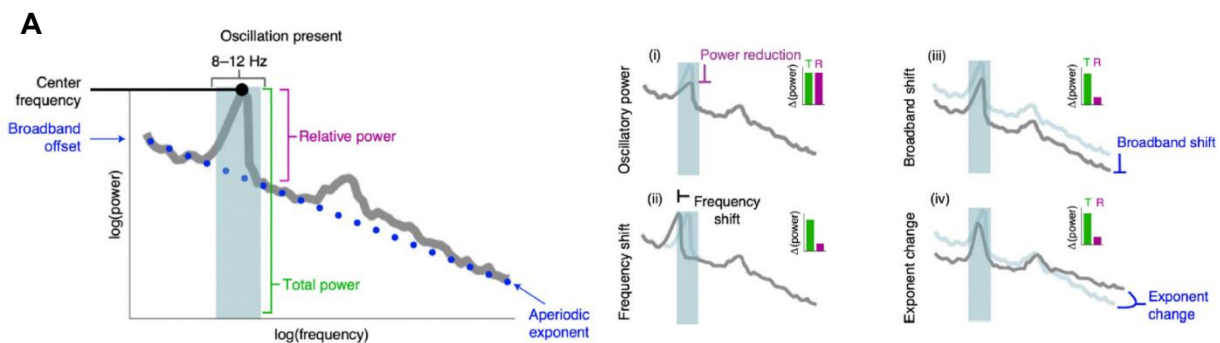


Figure 3: Oscillation frequency and power detected by the method *fooof*. **A:** Example of an 8-12 Hz oscillation peak (blue-shaded area) with a detected center frequency peak, the total and relative power of the peak, the broadband offset and the aperiodic exponent indicated by the blue dotted line. **(i)** Example of an oscillatory power reduction, **(ii)** a left sided frequency shift towards lower frequencies, **(iii)** a broadband shift towards lower power and **(iv)** a change in the aperiodic exponent towards flatter values (modified figure from Donoghue et al., 2020).

By using the open-source toolbox “fitting-oscillation-and-one-over-f” (*foooof*; version 1.0.0; Donoghue et al., 2020), the method allowed to include two main components for neural power spectra analysis: first, the aperiodic component, which is the one-over-f ($1/f^x$) background activity and is characterized by decreasing power at higher frequencies, and second, the periodic component representing the oscillatory activity, which appears as peaks in the power spectrum. *Fooooof* works by fitting the aperiodic component (finding the aperiodic exponent x in $1/f^x$) to the power spectrum and subtracting this aperiodic fit to isolate the periodic component (Fig. 3). Additionally, the aperiodic exponent thought to reflect local excitation/inhibition (E/I) balance (Wiest et al., 2023). Changes in the aperiodic exponent to either steeper or flatter values, as seen in the example, suggest stronger or reduced inhibition, respectively (Fig. 3A (iv)).

For each of the three different brain states, a theta (frequency range: 5-18 Hz, aperiodic mode: “bend knee”, number of peaks: 1, peak bandwidth: 1-12 Hz), beta (frequency range: 19-31 Hz, aperiodic mode: “fixed knee”, number of peaks: 1, peak bandwidth: 2-10 Hz), low and high gamma (frequency range: 32-198 Hz, aperiodic mode: “fixed knee”, number of peaks: 2, peak bandwidth: 20-60 Hz) frequency peak with a corresponding power value were identified in almost each animal. Graphical visualization and statistical analysis of frequency and power were performed using GraphPad Prism 10. The data are depicted in a scatter dot plot, and statistical significance was assessed using a nonparametric one-way ANOVA test (Kruskal-Wallis). Significance levels were denoted by one to three asterisks (* $p \leq 0.05$, ** $p \leq 0.01$, *** $p \leq 0.001$). Unless otherwise stated, data points without asterisks or labeled as “ns” indicate non-significant differences ($p > 0.05$).

2.8 | *In vivo* recordings of hippocampal network activity

The *in vivo* experiments were performed during the active phase of the animals and, thus, during the dark period of the light cycle. The mice used for this experiment were between six and 32 weeks old.

2.8.1 | Implantation of the head plate

For *in vivo* acute recordings of brain activity in the Mobile HomeCage[®] (MHC; *Neurotar*, Finland), mice first were implanted with a head plate (magnetic stainless steel, model 13, round opening,

11 mm, weight approximately 0.9-1.3 g, *Neurotar*, Finland). Around 30 minutes before the surgery, mice were administered buprenorphine (0.0125 mg/kg_{body weight}) via i.p. injection. Mice were pre-anesthetized with 4 % isoflurane in 100 % oxygen. The animal was placed on a heating pad and body temperature was maintained at 37°C with a rectal probe. The animal's head was fixed in a stereotaxic frame and isoflurane was decreased to 1.8 % in 100 % oxygen. After shaving the fur of the head and disinfecting the skin, a medial skin incision was performed to expose the skull. The periosteum was removed using a 3 % hydrogen peroxide solution and a swab. Sterile saline solution was applied to neutralize the hydrogen peroxide and cleanse the skull. The exposed skull surface was dried and coated with dental cement (*OptiBond™*, Kerr Dental, Germany) and cured with UV-light. An approximately 0.8 mm diameter hole was drilled over the cerebellum with a sterile microdrill. A skull screw, previously soldered to a wire and connected to the head plate, was inserted and fixed with dental glue, and served as a grounding electrode. The head plate was then adjusted to sit straight on the head, and fixed with dental glue (*Tetric EvoFlow*, *M+W Dental*, Germany). After the bregma-lambda distance was measured, a 0.8-1 mm diameter hole was drilled into the skull above the dorsal hippocampus (2 mm lateral and 1.7 mm caudal from bregma) for electrode insertion. The hole was sealed with a viscous two-component silicone gel and then sealed with a self-hardening silicone compound (*Kwik-Cast™*, *WPI*, USA). Postoperative analgesia was provided by a single subcutaneous injection of carprofen (5.0 mg/kg_{body weight}). The mice recovered from the surgery for five days, before starting *in vivo* recordings.

2.8.2 | Data acquisition in the MHC

Before recording, mice habituated to the MHC. Using air pressure, the MHC was suspended so that the head-fixed mouse could still move within the recording arena (round, diameter approximately 20 cm). Habituation was performed for around half an hour for three consecutive days.

For MHC recordings, the animals were head-fixed in the MHC arena. Silicon probes (32-channels; linear, Poly3, and Buz32; *Neuronexus*, Michigan, USA, Fig. 4) were labeled with DiI (*Thermo Fisher Scientific*, USA) or DiO (*Biotium*, USA) to track the electrode trace. Using micromanipulators and the program Pathway MPM Control (*NewScale Technologies*, USA), the electrode was slowly inserted into the hippocampus through the existing craniotomy above the dorsal hippocampus. Brain activity was acquired for one to two hours with Cheetah (version 6.4.1, *Neuralynx*, USA) and at the same time,

the animal's movement was recorded via the Locomotion Tracker Software (version 3.0.0.64 b3, *Neurotar*, Finland). After recording, the electrode was slowly removed, and the craniotomy was covered with silicone gel and Kwik-Cast. The silicone could then be easily removed before the next recording and reapplied after subsequent recordings. This allowed for acute brain wave recordings in the same animal over several days and weeks. Overall, animals were recorded two to three times per week and a maximum of once per day. Upon completion of the experiments, animals were anesthetized with ketamine/xylazine and transcardially perfused (see 2.3). The brain was then explanted for further examination of the electrode location.

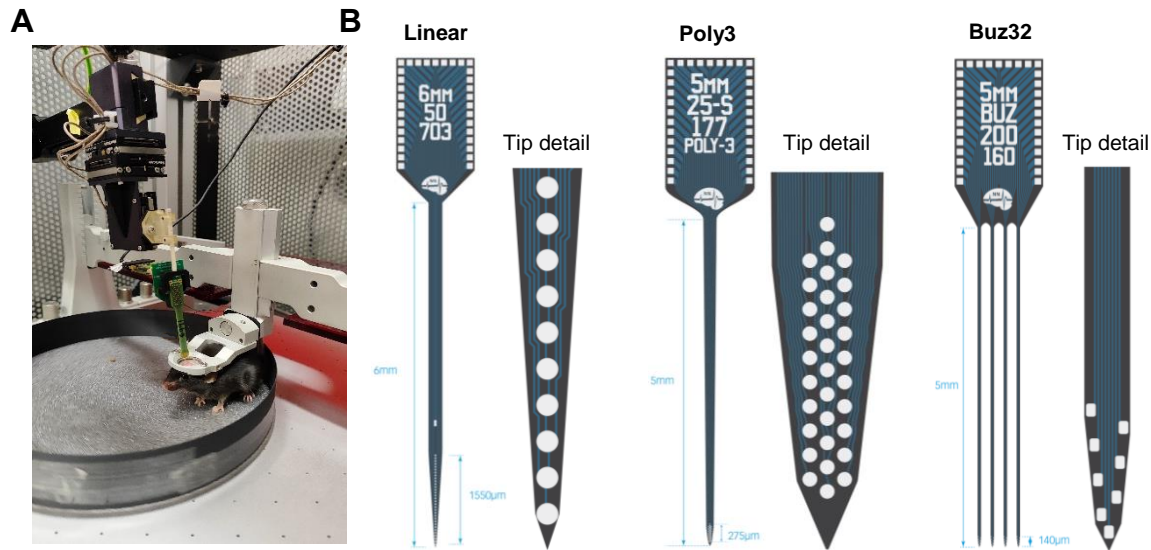


Figure 4: A head-fixed mouse in the Mobile HomeCage (MHC) recorded with different types of silicon probes. **A:** Moving head-fixed mouse in the MHC. **B:** Different types of silicon probes (from left to right: linear, Poly3, Buz32) with an overview image and the tip detail modified from ©Neuronexus, USA.

2.8.3 | Data analysis of MHC recordings

Acquired data during MHC recordings were further analyzed with specific MATLAB[®] scripts. First, periods of movement (RUN) and immobility (NORUN) were identified with the help of the locomotion tracker that recorded the animal's movement during the hippocampal recording, using a custom script in MATLAB[®].

Identification of each layer of the hippocampus was performed with the custom script *Brainwave*, and then used to generate PSD plots from stratum lacunosum moleculare (SLM) as well as stratum pyramidale (SP). Furthermore, as described in 2.7.3, the *foof* analysis was performed to identify all

frequency peaks as well as their amplitude in SLM and SP during RUN and NORUN periods for each recording (theta frequency range: 3-30 Hz, aperiodic mode: “bend knee”, number of peaks: 1, peak bandwidth: 1-12 Hz; low gamma frequency range: 30-100 Hz, aperiodic mode: “fixed knee”, number of peaks: 1, peak bandwidth: 10-80 Hz; high gamma frequency range: 100-200 Hz, aperiodic mode: “fixed knee”, number of peaks: 1, peak bandwidth: 10-60 Hz). For detection and visualization, 50 Hz noise and its harmonics were removed from the PSD plots by interpolating the data two seconds before and after 50, 100, 150 and 200 Hz noise peaks.

With the MATLAB[®] function *FindRipples* and a custom-made script, ripples were extracted from a predefined channel from recordings of a linear silicon probe. This ripple channel did not include unit firing, and as a reference channel, one channel below the predefined SLM channel was used. The following parameters were used to detect ripple activity: ripple duration: 25-150 ms, minimum-inter-ripple-merge: 40 ms, ripple band: 70-200 Hz. An average ripple PSD plot was generated after manually adjusting and removing false detections. Detected ripple frequencies and their amplitude were extracted for further statistical analysis.

Using Poly3 and Buz32 silicon probes (Fig. 4), MHC recordings from WT and GD mice were conducted to extract properties of neuron firing in the CA1 area of the hippocampus. Therefore, identified neurons were clustered using KlustaKwik 2.0 and manually curated using *Klusters* (version 1.6.2; Hazan et al., 2006; klusters.sourceforge.net). Further analysis with this predefined section of neurons was performed using the MATLAB[®] toolbox *CellExplorer* (version 1.7.2; Petersen et al., 2021; cellexplorer.org). The differentiation between putative pyramidal neurons (Pyr), putative inhibitory interneurons (IN), and wide-shaped interneurons (Wide-IN) was automatically conducted by *CellExplorer*, whereas further analysis focused on Pyr and IN. The mean waveform and autocorrelogram of two representative neurons (Pyr and IN) were conducted by *CellExplorer* and illustrated via MATLAB[®]. The cumulative probability distribution of the firing rate for Pyr and IN during RUN and NORUN periods was conducted by *CellExplorer* and plotted via GraphPad Prism 10. For statistical analysis regarding the *fooof* and ripple analysis, the average frequency and amplitude per animal was plotted. With the software GraphPad Prism 10, data were depicted in a scatter dot plot, and statistical significance was assessed using a nonparametric one-way ANOVA test (Kruskal-Wallis). Significance levels were denoted by one to three asterisks (* $p \leq 0.05$, ** $p \leq 0.01$, *** $p \leq 0.001$). Unless otherwise stated, data points without asterisks or labeled as “ns” indicate non-significant differences ($p > 0.05$).

3. | Results

3.1 | High mortality rate, reduced body weight, and spontaneous epileptic seizures in GD and MI mice

As investigated in previous studies (Kasemir, Master's thesis, 2020), heterozygous GD animals showed a significant decrease in survival as compared to WT littermates. In male and female GD mice, this increasing mortality started around three weeks of age and at 11 weeks, only around 75 % of the GD animals were still alive (Fig. 5A). In MI mice, heterozygous males also showed a decreased survival rate, where at 17 weeks, around 89 % of male MI mice were still alive (Fig. 5B, left). In female MI mice, the survival rate was more severely affected as compared to male animals, where at 22 weeks only 55 % of female MI mice were still alive (Fig. 5B, right). Body weights were significantly lower in male and female GD mice compared to WT littermates. Starting at four weeks, male GD mice had on average, a body weight of 24.4 ± 0.5 g, which was around 5 g less than WT littermates at 16 weeks (Fig. 5C, left). The same was true for female GD mice, with a body weight difference of around 5 g compared to WT littermates at 16 weeks (female WT: 23.9 ± 0.5 g, female GD: 19.4 ± 0.6 g; Fig. 5C, right). In male MI mice, similar results were obtained, with body weights around 28.8 ± 0.9 g at 16 weeks, compared to WT with 32 ± 1.4 g (Fig. 5D, left). Interestingly, female MI mice did not differ in body weight when compared to WT littermates over different ages. At 16 weeks, both groups had body weights around $24 \text{ g} \pm 2.2 \text{ g}$ (Fig. 5D, right).

Given the high mortality rate, together with spontaneously observed deaths and mice found dead in their home cages, ECoG recordings were performed in adult animals to investigate cortical brain activity and spontaneous epileptic seizures in more detail. GD mice, independent of sex, exhibited spontaneous epileptic seizures. One example seizure is shown in Figure 5E, with the upper trace illustrating the ECoG signal with the seizure marked with a red bar underneath. The seizure itself showed a successive increase in frequency and amplitude of spikes, followed by a depression period (Fig. 5E, middle trace). The time-frequency spectrogram revealed a strong 8 Hz frequency band during the seizure that slowly decreased to around 2 Hz towards the end of the seizure (Fig. 5E, lower trace). Additionally, the behavior during the seizures was quantified using a modified Racine's scale (see 2.7.3). Of a total of eight GD animals, six exhibited spontaneous seizures during the recorded time period. The highest behavioral seizure stage of each individual seizure was scored and represented as the percentage of the total amount of seizures (Fig. 5F). Male and female GD mice showed seizures

between stage 1 and 5, whereas the highest seizure stage of 6 was not observed in GD animals (Fig. 5F). MI mice, like GD mice, also exhibited spontaneous epileptic seizures, with an increase in frequency (8-16 Hz) and amplitude of spikes during the seizure, followed by a depression period (Fig. 5G). Out of 12 ECoG-recorded animals, ten mice exhibited spontaneous epileptic seizures. In contrast to the seizure severity of GD mice, MI male and female mice predominantly showed seizures that increased up to stage 6 of the modified Racine's scale (Fig. 5H).

These findings demonstrate the severe impact of GD and MI mutations on survival, growth, and neurological function, including a predisposition to spontaneous epileptic seizures with varying severity between the two mutations.

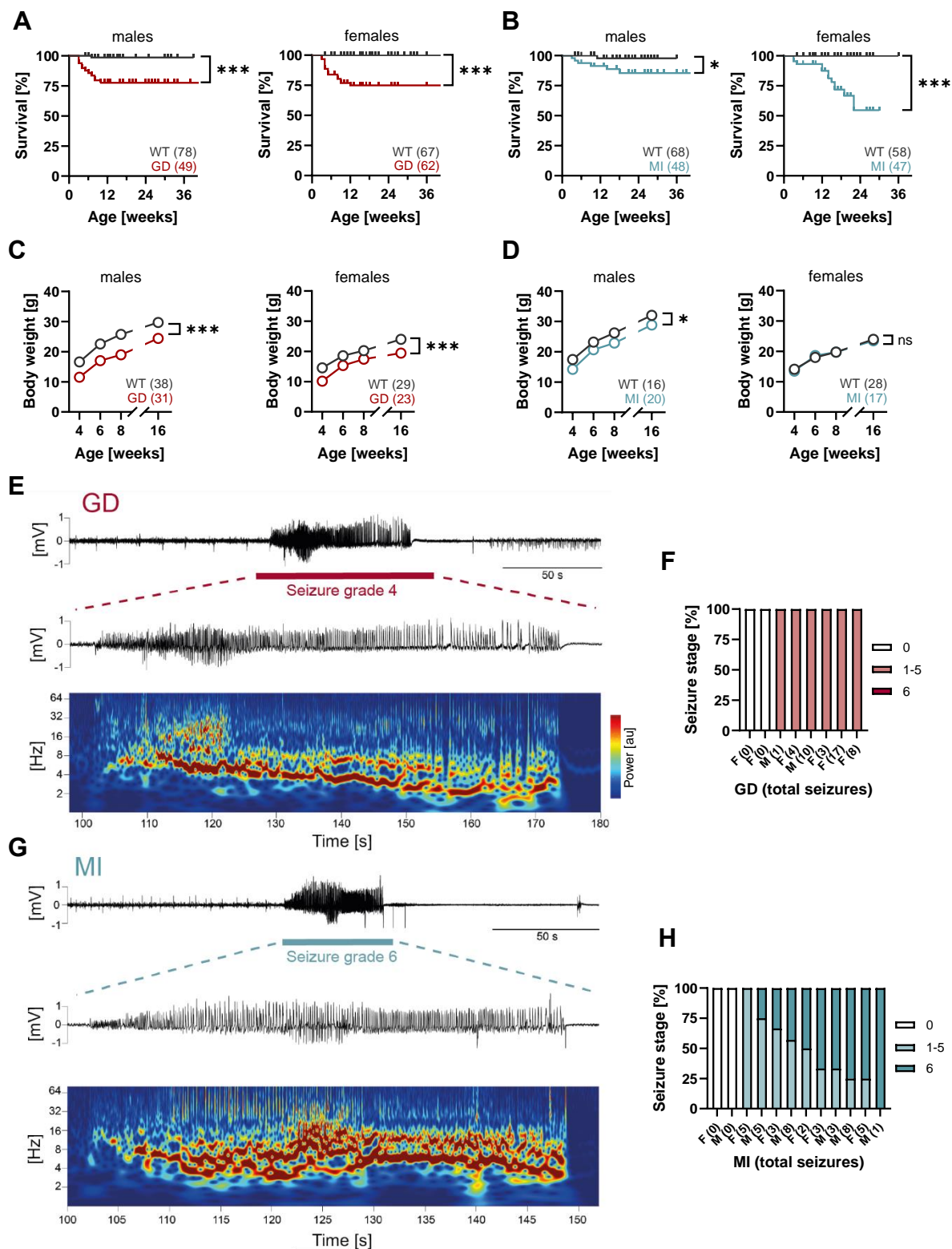


Figure 5: High mortality rate, reduced body weight, and spontaneous epileptic seizures in GD and MI mice (modified figure from Merseburg et al., 2022).

Figure 5 continued on the next page.

Figure 5 continued: **A:** Kaplan-Meier survival curves of male and female GD mice and **B:** male and female MI mice compared to WT littermates (* $p < 0.05$, *** $p < 0.001$, log-rank Mantel-Cox test). Each tic represents a death which was scored as 1 if it was a sudden death. **C:** Body weights of male and female GD mice and **D:** MI mice at different ages compared to WT littermates (ns = not significant, * $p < 0.05$, *** $p < 0.001$, effect of *genotype*, mixed-effects model having *age* x *genotype* as grouping factors). The number of animals used for each individual experiment are depicted in brackets. Data represent mean \pm SEM for body weights (note that smaller error bars may be hidden by the circles representing the mean). **E:** Example of a spontaneous seizure from a GD mouse. Upper trace: ECoG signal in mV with the red bar marking the duration of the seizure and the behavioral seizure stages 4. Middle trace: zoomed in area of the ECoG signal in mV. Lower trace: corresponding time-frequency spectrogram in seconds and Hz, respectively. Warm colors indicate high power; cold colors indicate low power. **F:** The highest seizure stage of GD mice (M = male, F = female) reached during the recording period is plotted as percentage of total seizures. GD mice did not reach the highest behavioral seizure stage of 6. Numbers in brackets indicate the number of total seizures that were detected during the ECoG recording. **G:** Same as **E:** but here, a spontaneous seizure of a MI mouse is depicted. **H:** Same as **F:** but here, more MI mice reached the highest seizure stage of 6 during the recorded period.

3.2 | Reduced firing rate and HCN1 protein expression in hippocampal CA1 pyramidal neurons in GD and MI mice

Analyses of intrinsic properties of neurons carrying the GD or MI mutation were performed in collaboration with Prof. Steven Siegelbaum's laboratory at Columbia University, New York, NY. First, HCN1 protein distribution in hippocampal CA1 pyramidal neurons was investigated by antibody labeling (Fig. 6A). In WT brains, the labeling of the HCN1 subunit revealed the expected distribution in pyramidal neurons, showing a gradient of increasing expression of the protein along the somatodendritic axis of apical dendrites (Fig. 6A, left). In GD and MI brains, the gradient was also present (Fig. 6A, middle and right), but after quantification of signal intensity, for GD, there was a strong and significant decrease in HCN1 protein expression (Fig. 6B, left). The same was true for MI, although with a smaller but significant decrease in protein expression along the apical dendrites of pyramidal neurons (Fig. 6B, right). These results were confirmed by whole-cell patch-clamp recordings, which demonstrated a significant reduction in the firing properties of GD and MI neurons (Fig. 6C), a reduction in the sag ratio of MI neurons, and a loss of the voltage sag in GD neurons upon injecting hyperpolarizing currents (Fig. 6D).

The RMP in GD neurons was significantly increased to more positive potentials than in WT cells, indicating a "leak" sodium current in this channel due to the mutation. On the other hand, in MI neurons, the RMP was not different compared to WT (Fig. 6E).

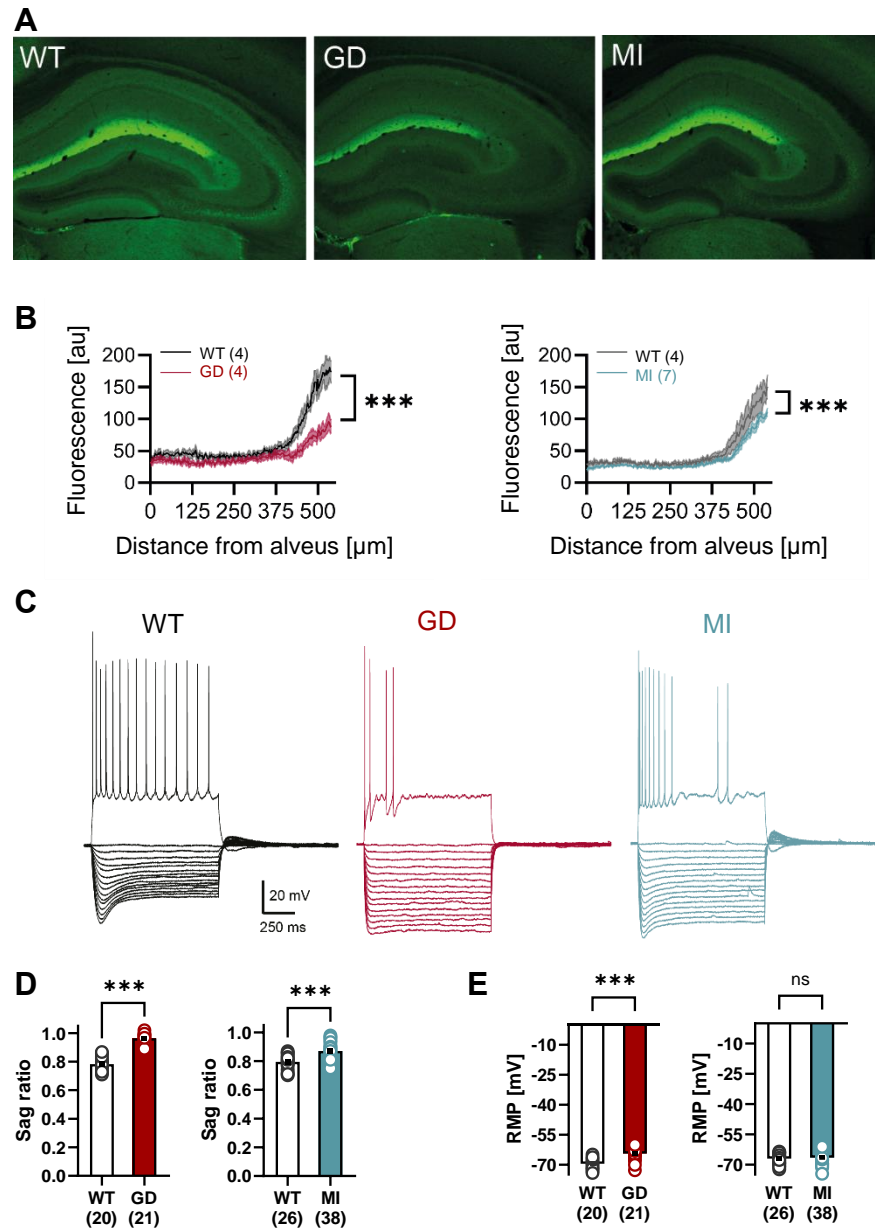


Figure 6: In CA1 pyramidal neurons, HCN1 protein expression and I_h -dependent voltage sag were diminished in both GD and MI mice (modified figure from Merseburg et al., 2022). **A:** HCN1 protein expression visualized by immunofluorescent labeling in adult WT, GD, and MI mice. **B:** Fluorescence in arbitrary units (au) was quantified along the somatodendritic axis of pyramidal neurons, showing a strong decrease of HCN1 protein labeling in distal dendrites especially in GD (***) $p < 0.001$, effect of *genotype* \times *distance from alveus*, two-way repeated-measures ANOVA). **C:** Representative sample traces from whole-cell current-clamp recordings in CA1 pyramidal neurons obtained from WT, GD, and MI. For all samples, a holding potential of -70 mV was used, with a series of hyperpolarizing and depolarizing current steps in 25 pA increases applied in the negative and positive direction (depolarizing step at +200 pA is shown). **D:** Reduced sag ratio in response to hyperpolarizing current steps (***) $p < 0.001$, Student's *t*-test) in both, GD (left) and MI (right). **E:** Resting membrane potential (RMP) in mV was shifted to more positive values in GD (left), but not in MI (right), compared to WT (***) $p < 0.001$, Student's *t*-test). **D+E:** Number of cells are indicated in the bar graph, number of animals used: GD WT (6), GD (5), MI WT (6), MI (5). Data represent mean \pm SEM. All results were obtained in collaboration with Prof. Siegelbaum's laboratory at Columbia University, New York, NY.

These findings suggest that both GD and MI mutations disrupt normal HCN1 channel function in hippocampal neurons, with the GD mutation causing a more severe neuronal phenotype, including a complete loss of the voltage sag and altered RMP, likely due to a dominant-negative effect of the GD mutation and abnormal gating.

3.3 | Behavioral comorbidities in GD and MI mice

Besides spontaneous epileptic seizures, heterozygous GD and MI mice additionally displayed behavioral comorbidities that ranged from alterations in locomotion and memory to changes in anxiety.

3.3.1 | Slight changes in neonatal development of GD mice

The two human patients that carried the p.G391D variant both exhibited a seizure onset at 30 and 48 hours after birth and died with 14 and 15 months of age, respectively. Already in their early life, they exhibited microcephaly and a severe intellectual disability (Marini et al., 2018). To investigate how this early life phenotype can be translated to our mouse model, GD pups underwent neonatal reflex tests during the first week of life (Fig. 7, see methods 2.6.1), and body weights were monitored from P1 to P8. Both, WT and GD (male as well as female) pups increased their body weight within a week from 1.5 ± 0.1 g to 4.2 ± 0.2 g for WT males and 3.9 ± 0.2 g for GD males, and from 1.5 ± 0.1 g to 4.3 ± 0.2 g for WT females and 3.7 ± 0.2 g for GD females (Fig. 7A). Notably, only female GD pups exhibited lower body weights as compared to WT littermates (significant effect of *age* x *genotype*, Fig. 7A right).

In the next step, cliff avoidance behavior, righting reflexes and geotactic reflexes were analyzed. The cliff avoidance behavior (Fig. 7B) tested the ability to turn 90° away from a cliff. WT and GD pups (both genders) increased their performance from 20.2 ± 2.7 s for WT and 16 ± 3.1 s for GD at P2 up to 4 ± 0.5 s for WT and 7.2 ± 1.6 s for GD at P8, with no difference observed within genotypes (Fig. 7C). During the righting reflex, the pup's coordination, balance, and motor skills were investigated by the ability to turn from supine to prone position (Fig. 7D). Both WT and GD pups increased their performance significantly from P2 to P8. At P2, the average time for righting in WT pups was 24.2 ± 2.4 s and at P8 decreased to 2.6 ± 0.3 s. In GD pups, the performance increased from

26 ± 2.2 s at P2 to 3.1 ± 0.8 s at P8, with a significant genotype effect (Fig. 7E). Similar results were seen for the geotactic reflex test, where the pup's sense of orientation relative to gravity was investigated (Fig. 7F). Here, starting at P2 with 29.9 ± 0.04 s and 28.8 ± 1.1 s to complete the task, WT animals decreased the time needed for turning to 10.4 ± 1.9 s and GD successfully turned within 6 ± 1.3 s at P8. For the righting reflex test, a significant genotype effect was observed between both groups from P2 to P8 (Fig. 7G).

These findings suggest that while GD pups demonstrated comparable neonatal reflexes after the first week of life, the female body weights were significantly reduced compared to WT littermates. Thus, at least these types of tests do not reflect the severe neurological phenotypes observed in human patients carrying the p.G391D variant.

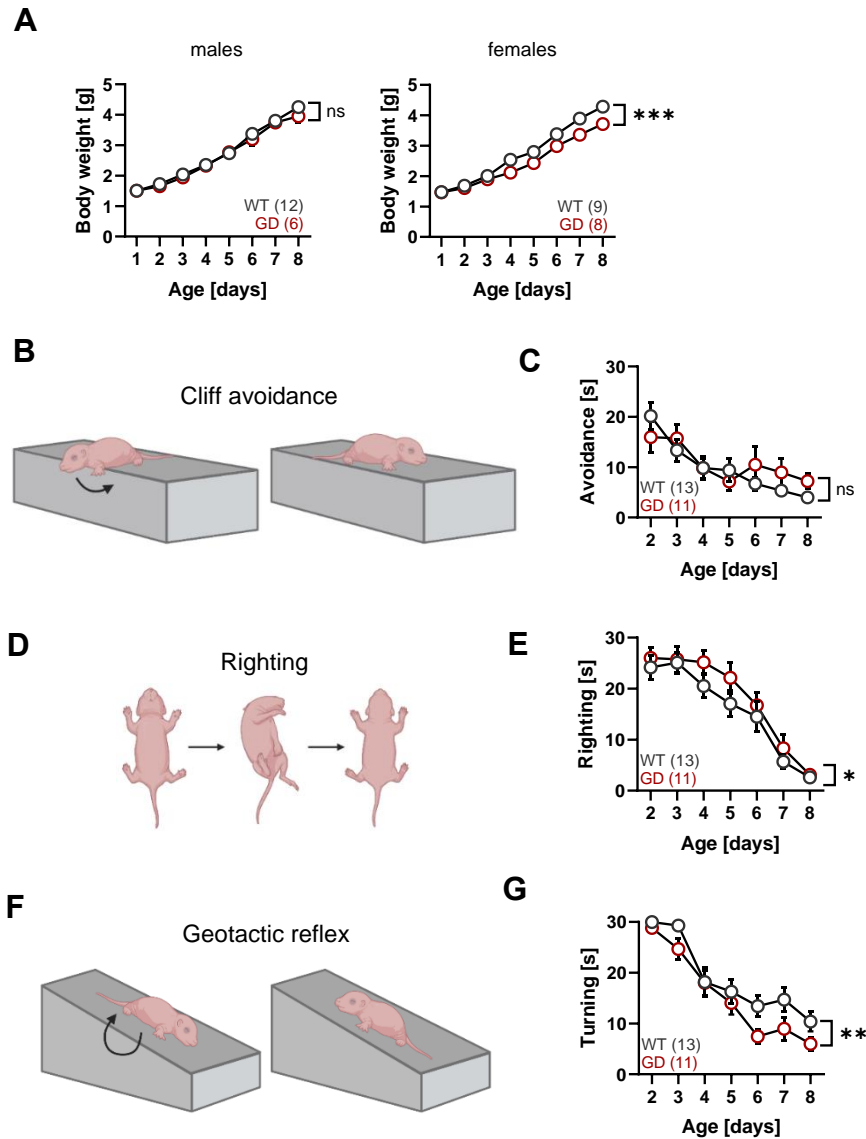


Figure 7: Neonatal body weight development of GD mice was slightly impaired. **A:** Body weight from P1 to P8 for male (ns = not significant, effect of *age* x *genotype*, two-way repeated-measures ANOVA) and female pups (*** $p < 0.001$, effect of *age* x *genotype*, two-way repeated-measures ANOVA). **B:** Schematic representation of the cliff avoidance reflex, **D:** the righting reflex, and **F:** the geotactic reflex (created by BioRender.com). **C:** Latency to avoid the cliff, **E:** righting, and **G:** turning in seconds. Righting and geotactic reflex had a significant difference between both groups, whereas avoidance was not significantly different (ns = not significant, * $p < 0.05$, ** $p < 0.01$, effect of *genotype*, two-way repeated-measures ANOVA). The number of animals used for each experiment is depicted in brackets. Data represent mean \pm SEM (note that smaller error bars may be hidden by the circles representing the mean).

3.3.2 | Locomotor hyperactivity in GD and MI, and motor coordination deficits in GD mice

The open field (OF) test was used to evaluate exploratory behavior and locomotion in a novel environment (Fig. 8A). Heterozygous GD and MI mice exhibited a significant increase in mean distance moved (WT GD: 60 ± 2.4 m, GD: 112.7 ± 10.2 m; WT MI: 68.4 ± 2.8 m, MI: 106.7 ± 3.5 m) and mean running velocity (WT GD: 6.7 ± 0.3 cm/s, GD: 12.5 ± 1.1 cm/s; WT MI: 7.6 ± 0.3 cm/s, MI: 11.9 ± 0.4 cm/s) during the 15-minute-trial, which was indicative of locomotor hyperactivity (Fig. 8B, first and third column). Additionally, GD mice failed to habituate to the OF arena, as was seen by their distance moved across the first two five-minute-intervals (38.5 ± 3.7 m to 38.8 ± 4.1 m), whereas WT GD littermates demonstrated a reduction in movement over time (22.3 ± 0.9 m to 19.3 ± 1.0 m). In contrast, MI mice exhibited habituation to the arena (5 to 10 to 15 min: 39.6 ± 1.7 m to 35.8 ± 1.4 m to 31.3 ± 0.9 m), similar to WT MI littermates (5 to 10 to 15 min: 26.8 ± 1.2 m to 21.6 ± 1.1 m to 19.9 ± 1.1 m; Fig. 8B, second column).

Moreover, analysis of time spent in the border zone versus the center zone of the OF arena revealed that both GD and MI mice spend more time in the border zone (indicated by values near -1, GD: -0.9 ± 0.02 , MI: -0.9 ± 0.01), whereas WT littermates spent significantly more time at the center zone (WT GD: -0.8 ± 0.02 , WT MI: -0.8 ± 0.04 ; Fig. 8B, forth column). Typically, increased time spent at the border rather than the center of an arena is indicative of increased anxiety levels, as mice tend to stay near walls to avoid open arenas. However, this usually comes along with less movement, which was not observed for the GD and MI mice, and it appeared that their behavior is more indicative of persistent locomotion around the border, resulting in an occupation ratio near -1.

The pole test is a valuable experiment for assessing motor coordination (Fig. 8C). Across three consecutive trials, GD mice displayed poor performance in grabbing the pole's tip, turning 180° to face downwards, and climbing down the pole. In nearly all trials, GD mice slid down or fell from the pole, which was noted as failure. This was reflected in lower success rates (trial 1: 5.6 %, trial 2: 5.6 %, trial 3: 11.1 %), and represented a significant decrease in the performance compared to WT GD littermates (trial 1: 90.9 %, trial 2: 100 %, trial 3: 100 %; Fig. 8D, first row).

In contrast, MI mice successfully completed the task with no difficulties, achieving a 100 % success rate as WT MI littermates. There was no difference detected in the mean latency to turn between WT MI littermates and MI mice (WT: trial 1: 18.2 ± 2.5 s, trial 2: 12.6 ± 0.8 s, trial 3: 15.2 ± 2.1 s; MI: trial 1: 20.6 ± 6.8 s, trial 2: 9.7 ± 0.8 s, trial 3: 14.9 ± 5.9 s; Fig. 8D, second row).

In summary, while both GD and MI mice displayed locomotor hyperactivity compared to WT littermates, GD mice exhibited more pronounced motor coordination deficits.

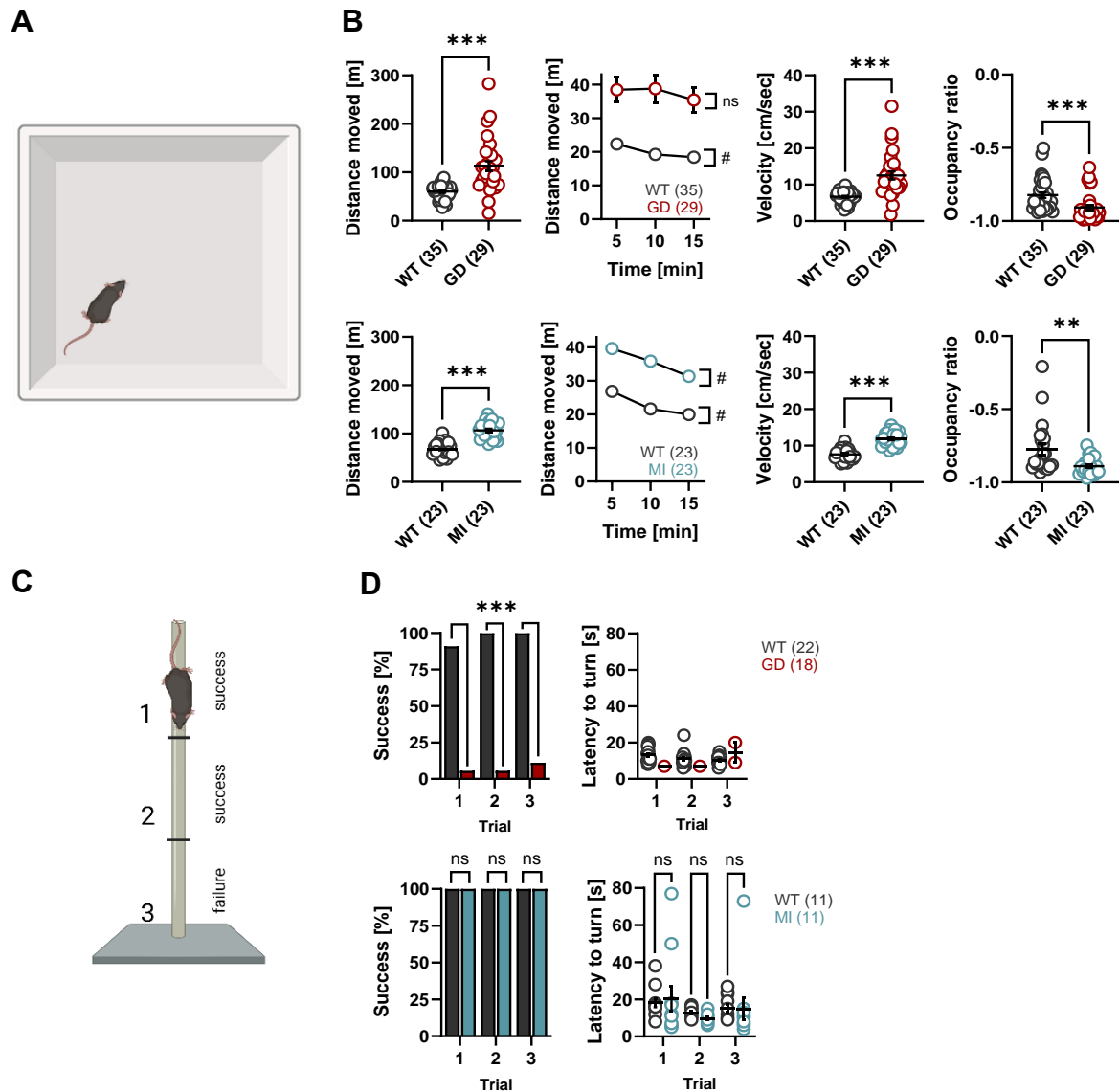


Figure 8: Locomotor hyperactivity in GD and MI, and motor coordination deficits in GD mice. **A:** Schematic representation of the open field arena (created by BioRender.com). **B:** GD (top) and MI (bottom) mice showed an increase in the total distance moved as well as distance over time, with increased velocity in both groups. The decreased occupation ratio indicated that they spent more time at the border area than in the center area of the arena compared to WT littermates (** $p < 0.01$, *** $p < 0.001$, Mann-Whitney U test). Each dot indicates an individual animal with mean \pm SEM presented. For distance moved over time, GD mice did not habituate to the arena (ns = not significant # $p < 0.05$, effect of *time*, two-way repeated-measures ANOVA having *genotype* and *time* as grouping factors). Data represent mean \pm SEM (note that smaller error bars may be hidden by the circles representing the mean). **C:** Schematic representation of the pole test (created by BioRender.com). **D:** Mean success rate of mice (ns = not significant, *** $p < 0.001$, Fisher's exact probability test) and latency to turn (ns = not significant, two-way repeated measures ANOVA with *group* \times *trial*, only performed for WT and MI mice) indicated a severe impairment in motor coordination in GD mice, but not for MI mice when comparing with WT littermates. For latency, each dot indicates an individual animal with mean \pm SEM presented. The number of animals used for each experiment is depicted in brackets.

3.3.3 | Changes in cognitive functions in GD and MI mice

The spontaneous alternation task is used in rodents to test their naturalistic behavior for alternating between different arms in a maze and is strongly dependent on several brain regions like hippocampus and neocortex (Hölter et al., 2015). In the Y-maze, mice must alternate spontaneously between three arms, and consecutively visit each arm to have one successful alternation, until 24 arm-visits were performed (Fig. 9A). Here, GD mice did not perform above chance level (mean arm alternation: 46.4 ± 4.1 %) and showed a significantly decreased alternation rate between the arms compared to WT GD littermates (mean arm alternation: 65.5 ± 1.3 %). However, some GD mice performed above the chance level, which indicates that there might be different genotype-effects in those mice. In contrast, MI mice showed no changes in alternation rates, where both WT MI littermates and MI mice performed at 61 ± 2.6 % and 63 ± 1.9 % above chance level, respectively (Fig. 9B, first column). The time mice spent in the arena was stopped after 24 arm visits. Here, both GD and MI mice had reduced latencies (GD: 3.7 ± 0.3 min; MI: 3.8 ± 0.2 min) compared to WT littermates (WT GD: 8.1 ± 0.4 min, WT MI: 5.7 ± 0.3), reflecting the locomotor hyperactivity in the two mutant lines (Fig. 9B, second column).

Another memory test utilized was the ORM task, which assesses long-term memory. The training phase was followed by a testing phase 24 hours later. During testing, mice needed to distinguish between a familiar object already known from training and a novel object (Fig. 9C). The discrimination index indicates a preference for the novel object if values are above 0, and a preference for the familiar object if values are below 0.

Both WT GD and GD mice, as well as WT MI and MI mice showed a discrimination index above 0 (chance level), with no significant difference between the groups (WT GD: 0.3 ± 0.05 , GD: 0.5 ± 0.1 , WT MI: 0.3 ± 0.1 , MI: 0.2 ± 0.1 ; Fig. 9D, first column). These results indicated that all groups spent more time exploring the novel object (Obj2) compared to the familiar object (Obj1), as further illustrated by the before-after plots for the object interaction time (Fig. 9D, second and third column).

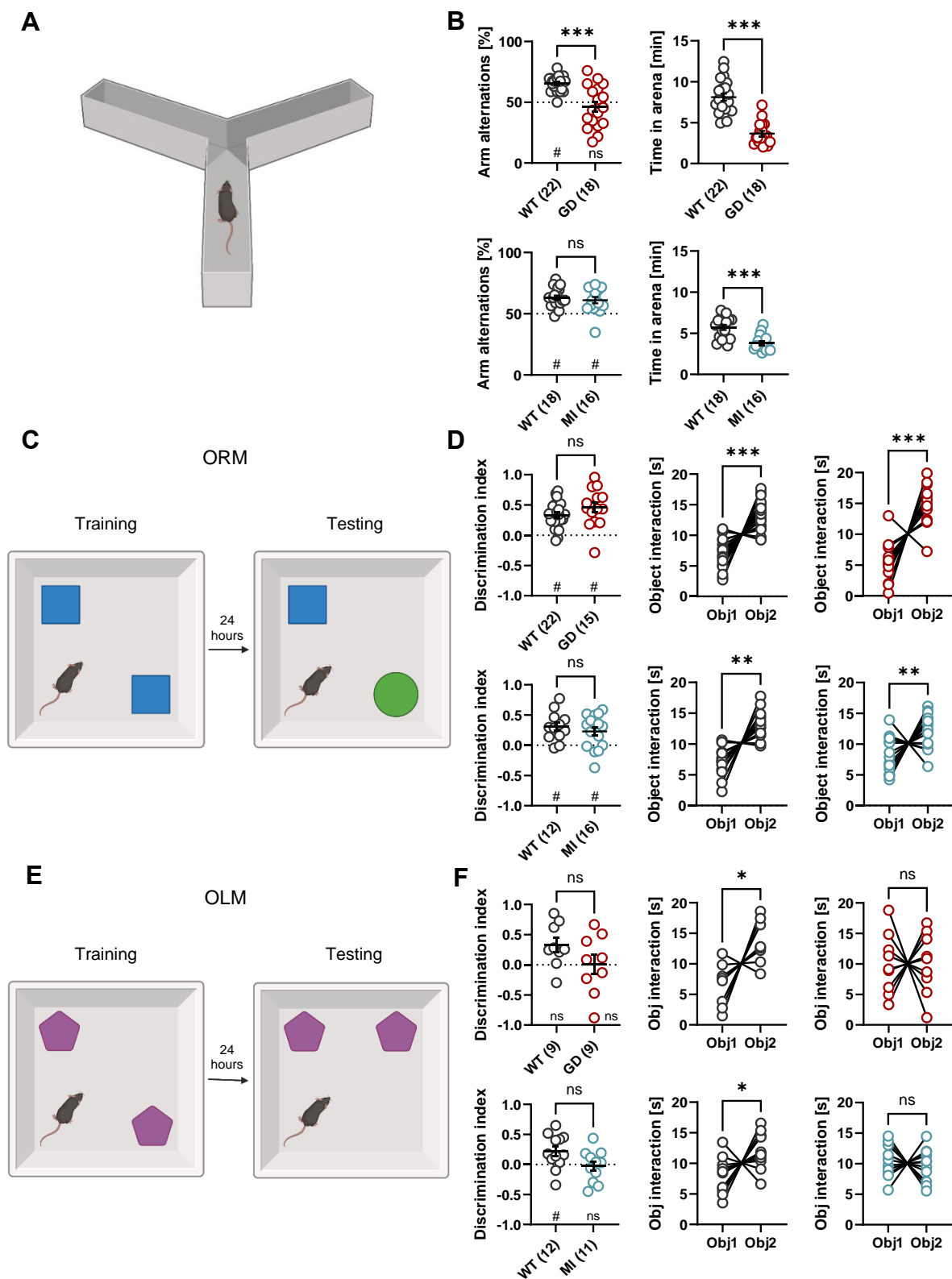


Figure 9: Cognitive functions in GD and MI animals were mildly affected.
Figure 9 continued on the next page.

Figure 9 continued: **A:** Schematic representation of the Y-maze arena testing spontaneous alternation (created by BioRender.com). **B:** Arm alternations and time spend in the arena are presented for both GD (top) and MI (bottom) mice and compared to WT littermates (ns = not significant, *** $p < 0.001$, Mann-Whitney U test). For arm alternations, the test was successful when animals performed above chance level of 50 % (ns = not significant, # $p < 0.05$, one-sample Wilcoxon test), which was not observed for GD mice and suggested an impairment. **C:** Schematic representation of object recognition memory (ORM) and **E:** object location memory (OLM) task (created by BioRender.com). **D:** Discrimination index with values > 0 indicating a preference for the new object) for ORM (# $p < 0.05$, one-sample Wilcoxon test to chance level of 0) on testing day was above chance level for all three groups. The interaction time with object 1 and object 2 indicated significantly more time spent at the new object 2. **E:** Discrimination index for OLM (ns = not significant, # $p < 0.05$, one-sample Wilcoxon test to chance level of 0) showed a performance above chance level only for WT MI mice (bottom), whereas the other groups did not perform above chance level. For WT GD and WT MI, the object interaction time with the moved object 2 was significantly increased compared to object 1, whereas this was not observed for GD and MI. Each dot indicates an individual animal with mean \pm SEM presented (except for object interaction). The number of animals used for each experiment is depicted in brackets.

The OLM task is similar to the ORM task, but instead of replacing an object, one of the identical objects was moved to a different position during testing, thereby assessing long-term spatial memory (Fig. 9E). Due to the higher difficulty of this test, only WT MI mice showed a discrimination index above chance level. No significant difference was observed between WT GD (0.3 ± 0.1) and GD (0.01 ± 0.2) mice, or between WT MI (0.2 ± 0.1) and MI (-0.03 ± 0.1) mice (Fig. 9F, first column). Analysis of the object interaction time demonstrated that both WT groups spent more time at the moved object (Obj2), while no significant difference in interaction time between Obj1 and Obj2 was detected for GD and MI mice (Fig. 9F, second and third column).

Overall, these results suggest that while both GD and MI mice exhibit locomotor hyperactivity, their cognitive deficits differ, with GD mice exhibiting broader and stronger cognitive impairments in spatial orientation and memory.

3.3.4 | Changes in anxiety-like behavior in GD and MI

The EPM is a behavioral assay used in rodents to evaluate anxiety-like behavior (Fig. 10A). Normally, mice tend to spend more time in closed arms (CAs) compared to open arms (OAs) because they feel safer in CAs. Here, GD mice spent significantly less time in the CAs (21.8 ± 6.0 s) and significantly more time in the OAs (115.9 ± 7.9 s) compared to WT GD littermates, as indicated by the mean arm preference with values near 1 (WT: -0.3 ± 0.1 , GD: 0.7 ± 0.1 ; Fig. 10B, first row). For MI mice, the time spent in the CAs was comparable to WT MI littermates, but overall, they spent more time in the

OAs, with a mean arm preference of 0.04 ± 0.1 compared to WT MI littermates (-0.3 ± 0.1 ; Fig. 10B, second row).

Another behavioral paradigm, the CFC, was used to assess associative learning and memory involving the hippocampus and the amygdala. Here, mice were placed in a chamber with a grid (context). After two minutes of baseline, mice received several mild electric foot shocks. During recall, 24 hours later, mice were placed back into the chamber without receiving foot shocks (Fig. 10C). During baseline, it was observed that all groups exhibited nearly no freezing moments (Fig. 10D, first column). On the second day during recall, WT GD and WT MI mice increased the time they spent in total immobility to 25.1 ± 2.9 % and 16.3 ± 3.3 %, respectively. A slight increase was also observed in MI mice (8.8 ± 3.9 %) without a significant difference to WT MI littermates. However, GD mice (1.3 ± 0.6 %) still exhibited nearly no freezing behavior during the recall (Fig. 10D, second column).

Overall, GD mice demonstrate changes in anxiety-like behavior with an impaired fear conditioning response, which was not as strongly observed in MI. Importantly, it should be noted that the observed hyperactivity in these mice may contribute to the reduced freezing behavior, likely due to increased movement.

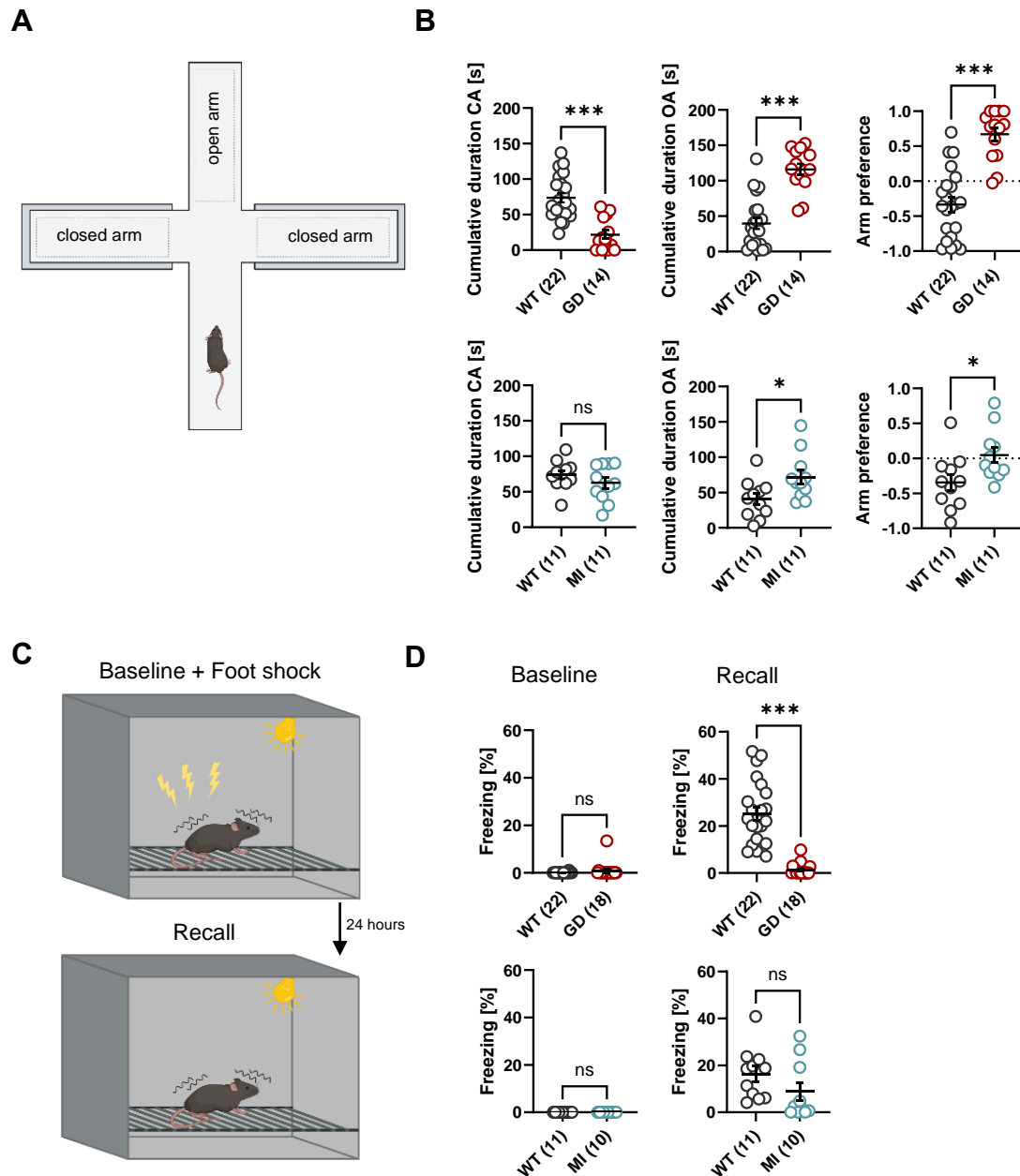


Figure 10: Changes in anxiety-like behavior in GD and MI mice. **A:** Schematic representation of the elevated plus maze (EPM) with two closed arms (CA) and two open arms (OA; created by BioRender.com). **B:** Cumulative duration of CA and OA, with GD and MI mice spending significantly more time in the OA compared to WT littermates (ns = not significant, * $p < 0.05$, *** $p < 0.001$, Mann-Whitney U test). The arm preference indicated the same, with GD and MI mice showing levels above 0, and WT mice levels below 0. Note: For the analysis of EPM, the first three minutes of the test were included because after that, most of the GD mice either jumped or climbed down from the OA. **C:** Schematic representation of contextual fear conditioning (CFC) indicating baseline and foot shock on one day and recall 24 hours later (created by BioRender.com). **D:** Freezing in percentage is shown for baseline (first two minutes of the test, before any foot shock was applied) and recall, indicating significantly reduced freezing levels for GD mice compared to WT during recall, but not for MI mice (ns = not significant, *** $p < 0.001$, Mann-Whitney U test). Each dot indicates an individual animal with mean \pm SEM presented. The number of animals used for each experiment is depicted in brackets.

3.4 | Reduced cortical low and high gamma oscillation frequency and power during REM sleep in GD mice

Besides using telemetric ECoG recordings to identify spontaneous epileptic seizures in GD and MI mice, these ECoG recordings were also used to investigate differences in interictal activity. From 24-hour baseline recordings, REM, SWS, and ACTIVE (wake behavior) periods were analyzed. The implanted transponders with a 1-200 Hz bandwidth facilitated the identification of low and high gamma frequency oscillations in the cortex. REM sleep is characterized by a prominent theta band (6-9 Hz), as well as low gamma (40-60 Hz) and high gamma (60-100 Hz) activity (Bueno-Junior et al., 2022; Buzsáki and Wang, 2012). SWS predominantly demonstrates delta frequency (0.5-4 Hz), while ACTIVE periods show a broad range of frequencies (Panagiotou et al., 2017).

REM, SWS, and ACTIVE state analyses focused on theta, low, and high gamma frequency oscillation. PSD plots demonstrated distinct peaks at these frequencies in WT, GD, and MI mice during REM, although these peaks were less pronounced during SWS and ACTIVE states (Fig. 11A). The *fooof* analysis revealed that, compared to WT mice (8 ± 0.1 Hz), GD mice (8.4 ± 0.1 Hz) exhibited a slight increase in theta oscillation during REM sleep with no difference in power. Both low and high gamma frequencies were strongly reduced in GD mice (low gamma: 65.5 ± 0.9 Hz; high gamma: 107.5 ± 1.3) compared to WT (low gamma: 71.3 ± 1.1 Hz; high gamma: 129.5 ± 1.4 Hz), with a notable decrease in power (Fig. 11B, left column). In contrast, MI mice showed no significant differences compared to WT. During SWS, delta activity, particularly delta waves in the 0.1-1 Hz frequency range, could not be clearly detected due to the transponder's bandwidth. The *fooof* analysis detected a low amplitude theta peak, whereas no significant changes in either GD or MI mice were indicated (Fig. 11B, middle column). During the ACTIVE state, GD mice displayed a reduction in theta frequency (8.4 ± 0.1 Hz) compared to WT mice (8.8 ± 0.2 Hz), while MI animals showed an increase in power (3.9 ± 0.3 dB). Additionally, GD mice exhibited a slightly increase in low gamma activity (63.3 ± 0.7 Hz), whereas high gamma activity was significantly decreased in both in GD (108.6 ± 2.7 Hz) and MI mice (109.6 ± 3.3 Hz) when comparing with WT animals (low gamma: 61 ± 0.8 Hz; high gamma: 152.2 ± 6.1 Hz; Fig. 11B, right column).

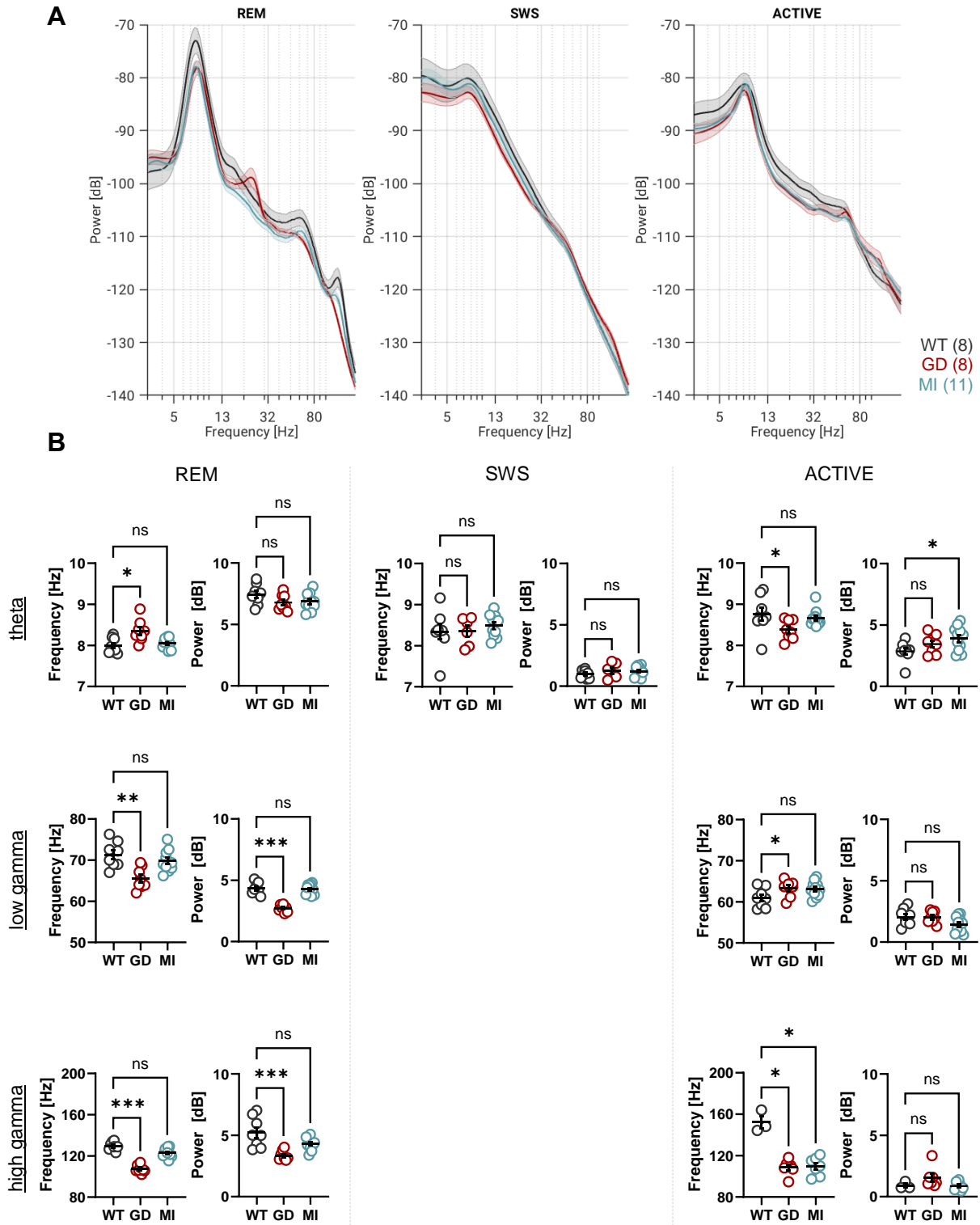


Figure 11: Reduced cortical low and high gamma oscillation frequency and power during REM sleep in GD mice.

A: Power-spectrum-density (PSD) plots with frequency in Hz and power in dB for WT, GD, and MI during REM, SWS and ACTIVE periods. The number of animals is depicted in brackets. Curves indicate mean \pm SEM.

Figure 11 continued on the next page.

Figure 11 continued: B: For nearly each mouse from WT, GD, and MI, the *foof* analysis revealed a frequency peak and the corresponding power value, which are plotted in scatter plots for REM (left column), SWS (middle column), and ACTIVE (right column) for theta (upper row), low gamma (middle row), and high gamma (lower row). Each dot indicates an individual animal with mean \pm SEM presented (ns = not significant, * $p < 0.05$, ** $p < 0.01$, *** $p < 0.001$, one-way ANOVA Kruskal-Wallis test).

Overall, the strong decrease in low and high gamma frequency during REM sleep suggests that there is a neuronal network dysfunction in GD mice linked to the mutation. Since gamma oscillations are associated with synchronous activity of excitatory and inhibitory neurons, the reduction in gamma frequency could indicate impaired synaptic transmission, reduced excitatory input from MEC to the hippocampus, or dysfunctional GABAergic interneurons (Buzsáki and Wang, 2012; Sohal et al., 2009).

3.4.1 | Beta oscillation frequency during REM sleep in GD mice

During REM sleep, in addition to theta, low gamma, and high gamma activity, GD animals also exhibited strong beta (13-30 Hz) activity (Mottaghi et al., 2021). Figure 12 shows an example ECoG recording, illustrating the transition from SWS to REM sleep, during which beta activity was clearly present (Fig. 12A). In all eight GD animals, beta oscillations were consistently observed during REM sleep at a frequency of 24.4 ± 0.2 Hz and a power of 1.9 ± 0.4 dB. Notably, this beta peak was detected in one WT mouse and one MI mouse (Fig. 12B). The emergence of beta oscillations, particularly during REM sleep, could be due to alterations in the excitation/inhibition (E/I) balance, for example caused by PV+ interneuron dysfunction. To further investigate changes in E/I balance, the aperiodic exponent (see methods 2.7.3, Fig. 3), a potential power spectral correlate of the E/I balance was examined (Donoghue et al., 2020). Analyses across the three brain states – REM, SWS, and ACTIVE – revealed that during SWS, but not during REM sleep, GD mice displayed a reduced aperiodic exponent compared to WT animals (GD: 2 ± 0.03 ; WT: 2.3 ± 0.1), indicating a reduction in the slope and potentially a reduction of inhibitory activity in GD mice (Wiest et al., 2023). No significant differences in the aperiodic exponent were observed during the other brain states or between WT and MI mice (Fig. 12C).

These results suggest that the strong beta activity observed in GD animals during REM sleep may be related to altered inhibition, since also other brain states (SWS) indicate alteration in the E/I balance.

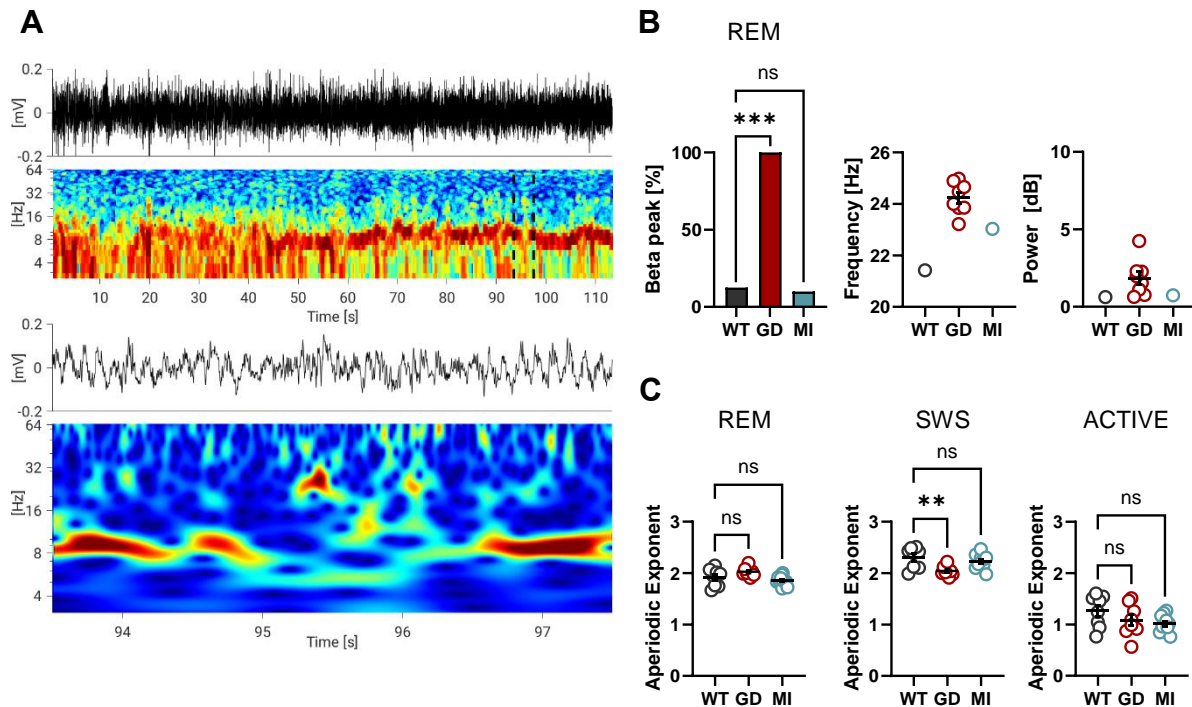


Figure 12: Beta oscillations during REM sleep and a reduced aperiodic exponent during SWS were observed in GD mice. **A:** Example of beta activity from a GD mouse. First two traces: ECoG signal in mV with corresponding time-frequency-spectrogram in seconds (s) and Hz. Note the transition from SWS to REM sleep at 52 s. Lower two traces: zoomed in area from the second trace (94-97 s). ECoG signal in mV with corresponding time-frequency spectrogram in s and Hz. Note a strong 24 Hz beta activity at 95.5 s. Warm colors indicate high power; cold colors indicate low power. **B:** Percentage of all animals, where beta activity peak was observed during REM sleep (ns = not significant, *** $p < 0.001$, Fisher's exact probability test), with frequency and power for each individual animal. Here, no statistical test was performed due to the low number of values. **C:** The aperiodic exponent during different brain states was reduced in GD mice during SWS, when comparing with WT (ns = not significant, ** $p < 0.01$, one-way ANOVA Kruskal-Wallis test). Each dot indicates an individual animal with mean \pm SEM presented.

3.5 | Anti-seizure medications paradoxically induce epileptic seizures in GD and MI mice

Several ASMs are established therapeutics used in the clinic to treat epilepsy in patients. Among these, LTG and PHT are commonly ASMs that function as sodium channel blockers. GD and MI mice received a single injection of LTG and PHT during ECoG recordings to assess their effects. Surprisingly, both ASMs paradoxically induced epileptic seizures in both mouse lines (Fig. 13). After

LTG injection, mice experienced several seizures approximately 1.5 hours post-injection (Fig. 13A). Representative seizures for both mouse lines show a stage 3 seizure in a GD mouse and a stage 6 seizure in a MI mouse, according to the modified Racine's scale. Analysis of seizure severity revealed that nearly 50 % of the MI mice reached the highest stage 6, while GD mice exhibited seizures ranging from stage 3 to 5 (Fig. 13C). After administering PHT, seizures occurred around 2.5 hours post-injection. Example seizures show a stage 3 seizure in a GD mouse and a stage 5 seizure in a MI mouse (Fig. 13B). Overall, GD mice consistently displayed seizures between stages 3 to 5, whereas some MI mice exhibited seizures up to stage 6 (Fig. 13C).

It has been reported that human patients with *HCN1*-linked DEEs treated with ASMs that included sodium channel blockers, experienced paradoxical responses to this treatment. Specifically, following ASM administration, these patients exhibited increased epileptic seizures up to status epilepticus (Bleakley et al., 2021; Marini et al., 2018). Given that these paradoxical responses occurred in unrelated patients, as well as in GD and MI mice, it is hypothesized that this may be due to functional changes associated with the mutations in *HCN1*.

In collaboration with Prof. Siegelbaum's laboratory at Columbia University, non-implanted mice were also injected with LTG and PHT, with seizures graded by the experimenter. Additionally, mice were injected with sodium valproate (VPA), which, in contrast to the other ASMs, did not induce epileptic seizures (Fig. 13C). However, VPA caused sedation in GD animals approximately 45 minutes post-injection, characterized by the lack of response to gentle touch or passive tail movement. This sedative effect was additionally observed in two out of eight MI mice. As a control injection, mice received a vehicle one week before or after ASM injections upon which no seizures were observed (Fig. 13C). WT littermates injected with LTG, PHT, and VPA did not show any seizure activity, nor did they exhibit sedative behavior (data not shown).

These results indicate that GD and MI mice, similar to human patients with *HCN1*-linked DEEs, experience an increase in seizures in response to sodium channel blockers. This suggests that the *HCN1* mutation may alter the E/I balance in the brain, leading to paradoxical responses to sodium-channel-blocking ASMs.

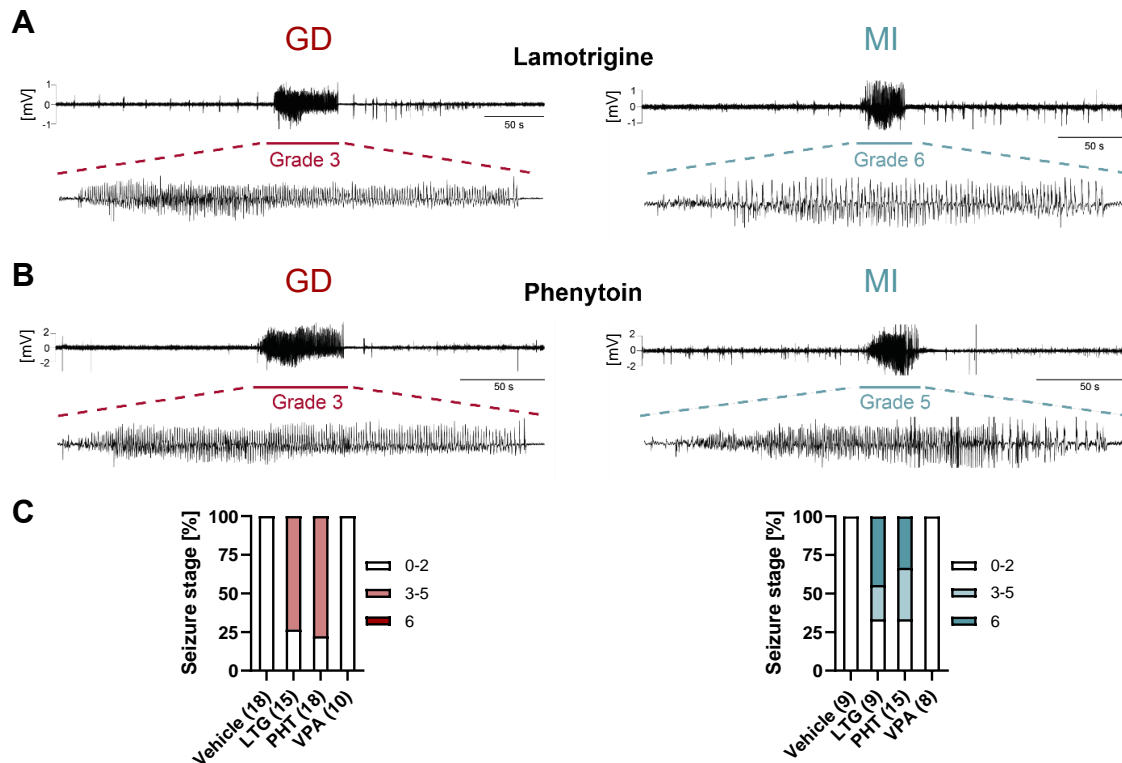


Figure 13: Anti-seizure medications (ASMs) induced epileptic seizures in GD and MI mice (modified figure from Merseburg et al., 2022). **A:** Example of electrocorticogram (ECoG) recordings after lamotrigine (LTG) injection with zoomed in traces below. Both GD and MI mice exhibited LTG-induced seizures with seizure stage 3 and 6, respectively. **B:** Example of ECoG recordings after phenytoin (PHT) injection with zoomed in traces below. Both GD and MI mice exhibited PHT-induced seizures with seizure stage 3 and 5, respectively. **C:** Seizure stage of all injected GD and MI mice after vehicle, LTG, PHT, or sodium valproate (VPA) injection. The highest seizure stage observed after injection is displayed in colors. As it was observed during spontaneous seizures, the seizure stage of MI mice increased up to the highest stage 6, whereas in GD mice, the seizure stage was between stage 3 and 5. Note: Four WT mice were injected with LTG and PHT with one week in between and none of those animals exhibited seizures (data not shown). The following animals were injected in Prof. Siegelbaum's laboratory without ECoG recordings, and the seizure behavior was noted by the experimenter: LTG: GD (13), MI (6); PHT: GD (12), MI (6); VPA: GD (10), MI (8).

3.6 | Changes in hippocampal gamma oscillations in GD and MI mice

HCN1 channels are not only highly expressed in cortical regions but are also present in the hippocampus (Bender and Baram, 2008). Consequently, the hippocampus is particularly interesting for studying differences in LFPs that may result from the two specific mutations in *Hcn1* – G380D and M142I. The SLM layer of the hippocampus is of high interest due to its high density of HCN1 channels in the distal dendrites of pyramidal neurons, as well as receiving its inputs from the entorhinal cortex (Neves et al., 2008; Nolan et al., 2007). LFP recordings were obtained from different layers in the hippocampus using a linear silicon probe (see 2.8.2, Fig. 4) in head-fixed mice in the MHC. Similar

to the analysis of ECoG recordings, hippocampal recordings were evaluated using PSD plots and *fooof* analysis. Since mice did not sleep in the MHC, REM and SWS periods could not be assessed. Instead, the analysis focused on two distinct brain states: periods of movement (RUN) and periods of immobility (NORUN; Fig. 14A). Further analysis using *fooof* indicated that theta frequency was not significantly different among the groups, but a reduction in power was noted in MI mice during NORUN periods (6 ± 0.5 dB) compared to WT mice (3.1 ± 0.5 dB; Fig. 14B, first row). Interestingly, during RUN, GD mice exhibited an increased low gamma frequency (61.1 ± 1 Hz) with a concomitant decrease in power (3.6 ± 0.3 dB) compared to WT mice (57.3 ± 0.8 Hz, 4.8 ± 0.5 dB; Fig. 14B, last row). As high gamma oscillation frequency peaks in the hippocampal LFP were not reliably detected in the PSD analysis, they were not analyzed further.

SP is a layer within the hippocampal CA1 region, containing the somas of pyramidal neurons and receiving input from PV+ basket cells, which synapse onto the somas and proximal dendrites of pyramidal neurons (Lebedeva et al., 2024). The PSD plots indicated that there are differences in SP between GD and MI mice, particularly in terms of frequency and power of gamma oscillations (Fig. 15A). *Fooof* analysis revealed no differences in theta oscillations in both GD and MI mice when comparing to WT animals (Fig. 15B, first row). However, during both RUN and NORUN periods, MI mice exhibited a significant reduction in low gamma oscillations (RUN: 51.1 ± 0.2 Hz, NORUN: 49.4 ± 0.6 Hz) compared to WT (RUN: 54.9 ± 0.2 Hz, NORUN: 51.5 ± 0.4 Hz), while GD mice showed a power reduction (RUN: 2 ± 0.3 dB, NORUN: 1.2 ± 0.1 dB; Fig. 15B, middle row). Additionally, although a high gamma frequency peak was not detected in every mouse during RUN, a slight reduction in high gamma frequency was observed in GD mice (125.1 ± 1.4 Hz) compared to WT (143.1 ± 6.1 Hz) without changes in power. This effect was more pronounced during NORUN, where GD mice exhibited a significantly decreased high gamma frequency (130 ± 1.7 Hz) compared to WT animals (148.1 ± 3 Hz; Fig. 15B, last row).

These results highlight distinct alterations in hippocampal oscillatory activity in GD and MI mice. Moreover, increased low gamma oscillations during movement in SLM indicate modifications in synaptic transmission from pyramidal cell projections from the entorhinal cortex to SLM (Neves et al., 2008). On the other hand, decreased high gamma frequency observed during immobility in SP in GD mice may indicate altered GABAergic interneuron function.

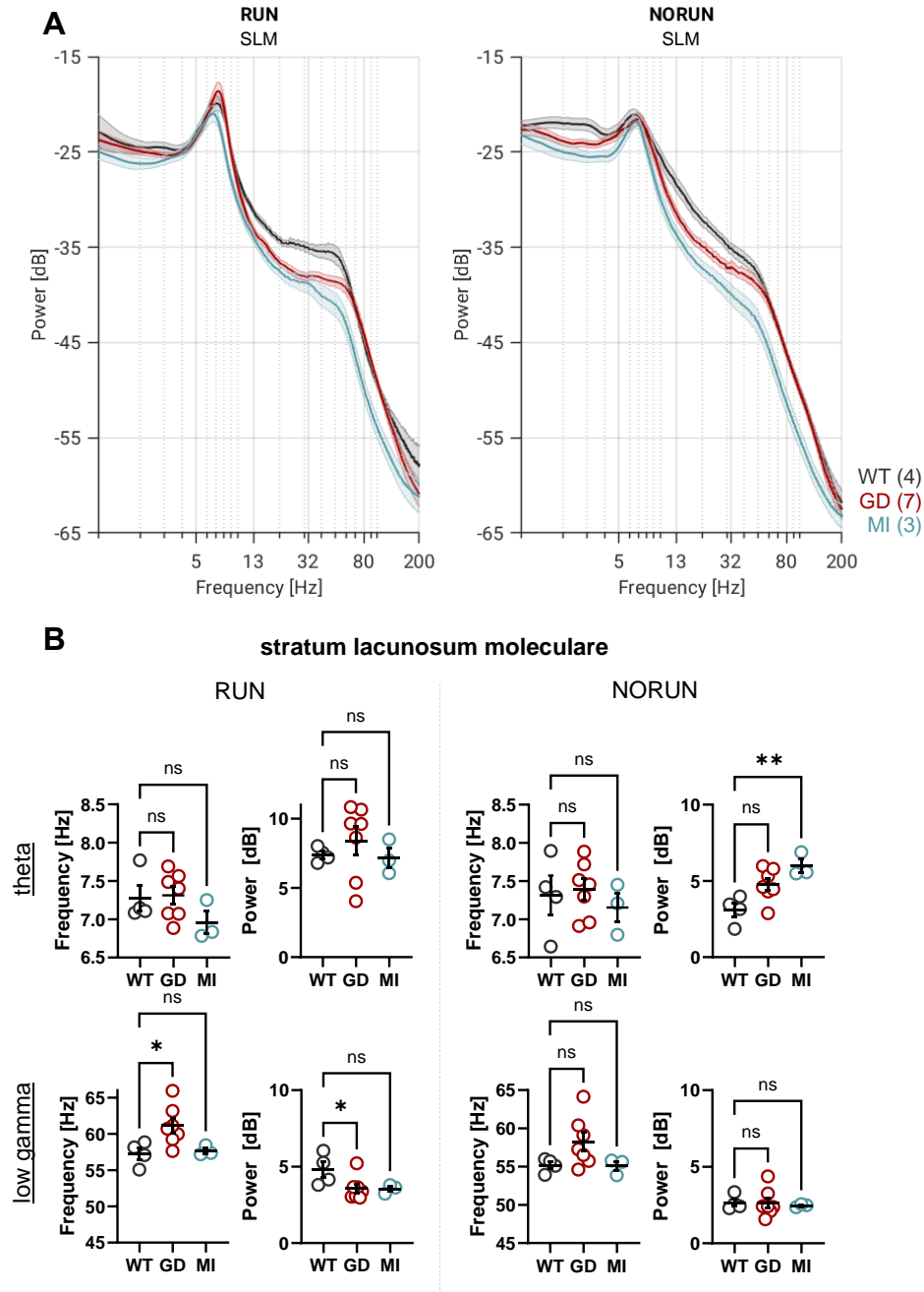


Figure 14: Increased low gamma oscillation frequency in stratum lacunosum moleculare (SLM) during movement periods in GD mice. **A:** Power-spectrum-density (PSD) plots with frequency in Hz and power in dB for WT, GD, and MI mice during RUN and NORUN periods for SLM. The number of animals is depicted in brackets. Curves indicate mean \pm SEM. **B:** The *foof* analysis was performed for each recording, each dot in the scatter plot reveals the mean value of each mouse. For nearly all mice a frequency peak and the corresponding power value was detected for RUN (left column) and NORUN (right column) periods for theta (first row) and low gamma (second row) frequency. Data represent mean \pm SEM (ns = not significant, * $p < 0.05$, ** $p < 0.01$, one-way ANOVA Kruskal-Wallis test).

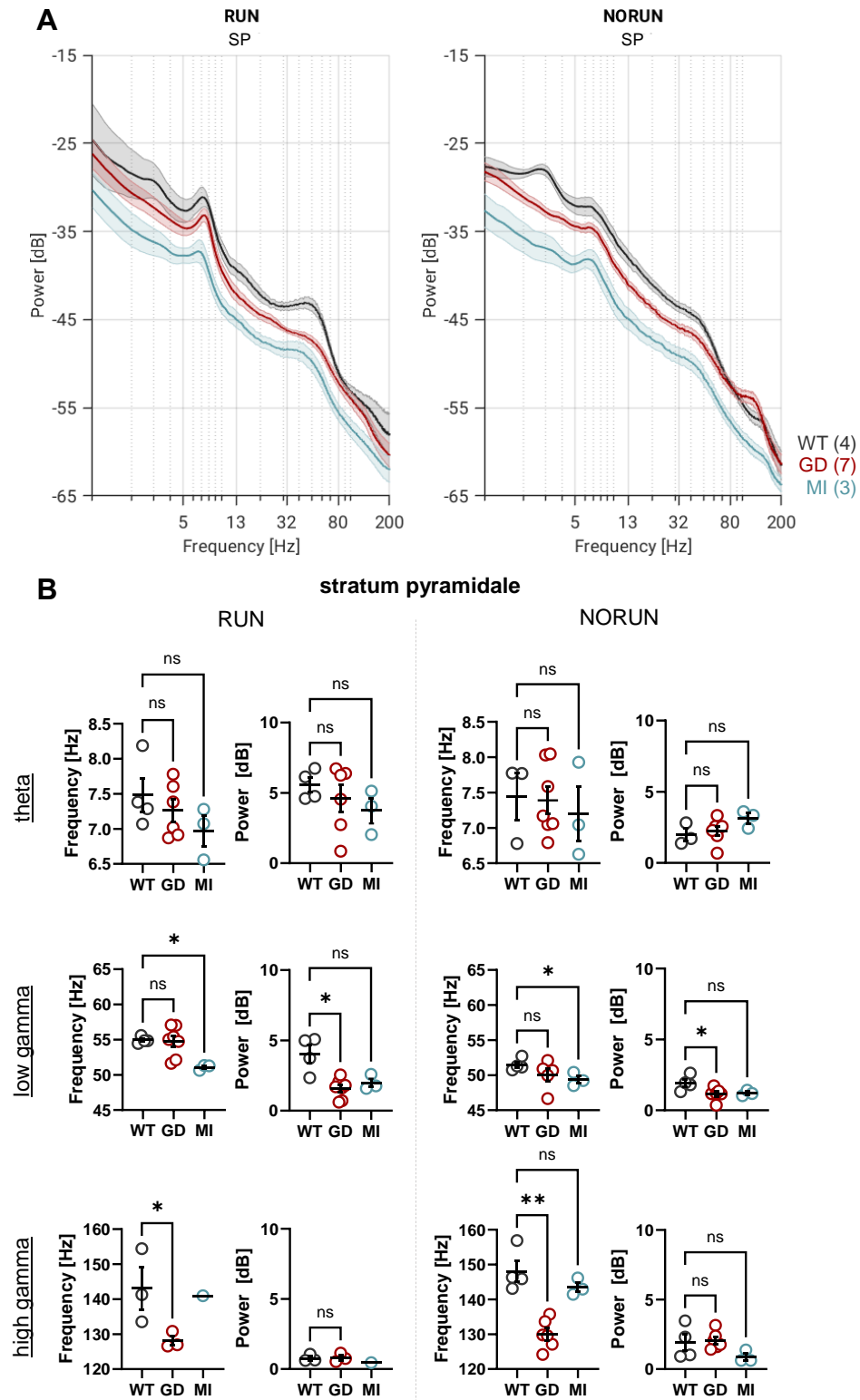


Figure 15: Reduced high gamma oscillation frequency in stratum pyramidale (SP) during immobility in GD mice.
Figure 15 continued on the next page.

Figure 15 continued: A: Power-spectrum-density (PSD) plots with frequency in Hz and power in dB for WT, GD, and MI during RUN and NORUN periods for SP. The number of animals is depicted in brackets. Curves indicate mean \pm SEM. **B:** The *foof* analysis was performed for each recording, each dot in the scatter plot reveals the mean value of each mouse. For nearly all mice a frequency peak and the corresponding power value was detected for RUN (left column) and NORUN (right column) periods for theta (upper row), low gamma (middle row), and high gamma (lower row) frequency. Data represent mean \pm SEM (ns = not significant, * $p < 0.05$, ** $p < 0.01$, one-way ANOVA Kruskal-Wallis test).

Further investigations of the aperiodic exponent in SLM during both RUN and NORUN, a reduced and therefore less steep aperiodic component was observed in GD mice (RUN: 1.5 ± 0.1 , NORUN: 2 ± 0.1) compared to WT animals (RUN: 2.0 ± 0.01 , NORUN: 2.4 ± 0.03 ; Fig. 16B). Moreover, SP revealed no difference between the three groups during RUN, but a reduced aperiodic exponent during NORUN in GD mice (1.5 ± 0.1) compared to WT mice (1.9 ± 0.1 ; Fig. 16A).

As already observed in ECoG recordings, this decreased aperiodic exponent in GD animals might relate to a shift in the E/I balance towards excitation due to altered interneuron function in the cortex, as well as in the hippocampus.

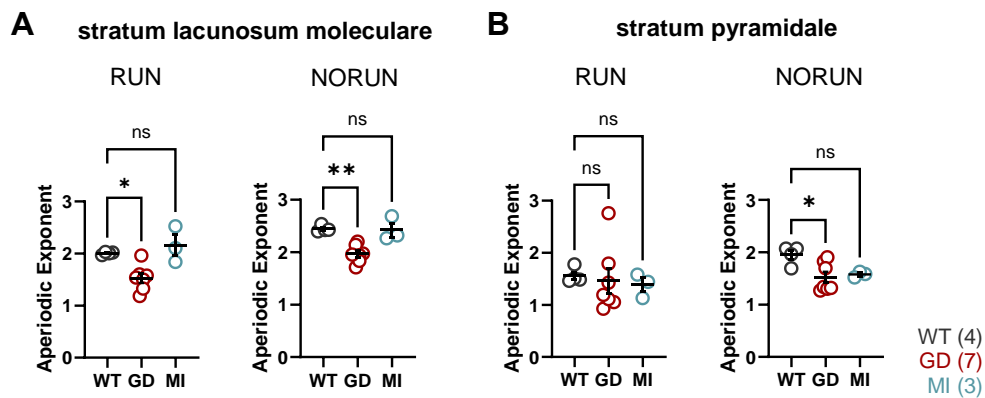


Figure 16: Reduced aperiodic exponent during movement and immobility in stratum lacunosum moleculare (SLM) and stratum pyramidale (SP) in GD mice. **A:** The scatter plot indicates the aperiodic exponent, where each dot represents the mean of a mouse from several recordings during RUN and NORUN periods for SLM, and **B:** SP. The number of animals are depicted in brackets. Data represent mean \pm SEM (ns = not significant, * $p < 0.05$, ** $p < 0.01$, one-way ANOVA Kruskal-Wallis test).

3.7 | Reduced ripple oscillation frequency and decreased neuron firing rates *in vivo* in GD mice

Ripple activity, which is crucial for memory consolidation processes and information transfer from hippocampus to cortex, was recorded from SP via linear silicon probes in the MHC during NORUN periods. The wavelet PSD plot revealed a left shift in ripple frequency and a reduction in power in GD mice compared to WT mice (Fig. 17A). Quantitative analysis showed that GD mice exhibited significantly lower ripple frequency (130.4 ± 2.5 Hz) and power (3.6 ± 0.5 dB) compared to WT mice (150 ± 3.7 Hz, 5.03 ± 0.5 dB). In contrast, MI mice demonstrated a significant reduction in power (2.7 ± 0.5 dB) but no significant difference in ripple frequency (141.5 ± 5 Hz, Fig. 17B).

Given the connection between ripple activity and memory consolidation, the impaired performance in memory tests observed in GD mice (Fig. 9) aligns with these *in vivo* findings, supporting the idea that the G380D mutation leads to memory impairment.

In addition to analyzing ripple activity, investigating neuronal firing patterns is crucial for identifying potential firing deficits in specific neuron types. The toolbox *CellExplorer* was employed to automatically distinguish between putative pyramidal neurons (Pyr, purple), putative inhibitory interneurons (IN, orange), and wide action potential-shape interneurons (Wide-IN), whereas the analysis primarily focuses on Pyr and IN. Waveforms and autocorrelograms of neurons facilitate the differentiation, as these parameters differ between Pyr and IN (Fig. 17C). The percentage of all detected neurons in two WT mice reveals that 73.8 % and 72.2 % of all cells are Pyr. However, in six GD animals, the distribution of Pyr and IN varied, with the proportion of Pyr ranging from 67.1 % down to 33.3 % (Fig. 17D). This suggests a possible reduction in Pyr numbers due to the mutation in GD animals and may either indicate pyramidal cell loss or reduced action potential rates.

The cumulative probability distribution of firing rates in putative Pyr during both RUN and NORUN periods indicates a left shift towards lower firing rates in GD neurons compared to WT (Fig. 17E, left). Although no significant difference was observed in the firing rates during RUN vs. NORUN periods within both WT and GD groups, a significant reduction in the firing rate was detected in Pyr of GD animals compared to WT in both RUN (WT: 5.6 ± 0.9 Hz, GD: 3.5 ± 0.4 Hz) and NORUN (WT: 5.2 ± 0.7 Hz, GD: 2.5 ± 0.3 Hz; Fig. 17E, right). These *in vivo* findings are supported by decreased firing properties of CA1 pyramidal neurons recorded *in vitro* in acute slices from GD mice (Fig. 6C).

In putative IN, the cumulative probability distribution also shows a left shift for GD neurons, particularly at lower firing rates. Additionally, around 10 Hz, a separation is observed in WT neurons, where their firing rates increase during RUN (13.1 ± 2.5 Hz) and decrease during NORUN (10 ± 1.6 Hz), though these differences are not statistically significant. In GD mice, this separation of firing rates during RUN (8.7 ± 1.4 Hz) and NORUN (6.7 ± 1.1 Hz) is observed around 25 Hz, without significant difference between these states (Fig. 17F). The increased firing rate during RUN suggests that these neurons may include PV+ basket cells, which are known to increase their activity during movement. Conversely, lower firing rates in GD mice may reflect other types of inhibitory interneurons, such as somatostatin-positive (SST+) interneurons. Potentially, the firing rates of putative IN may be affected by lower feed-forward excitation from Pyr.

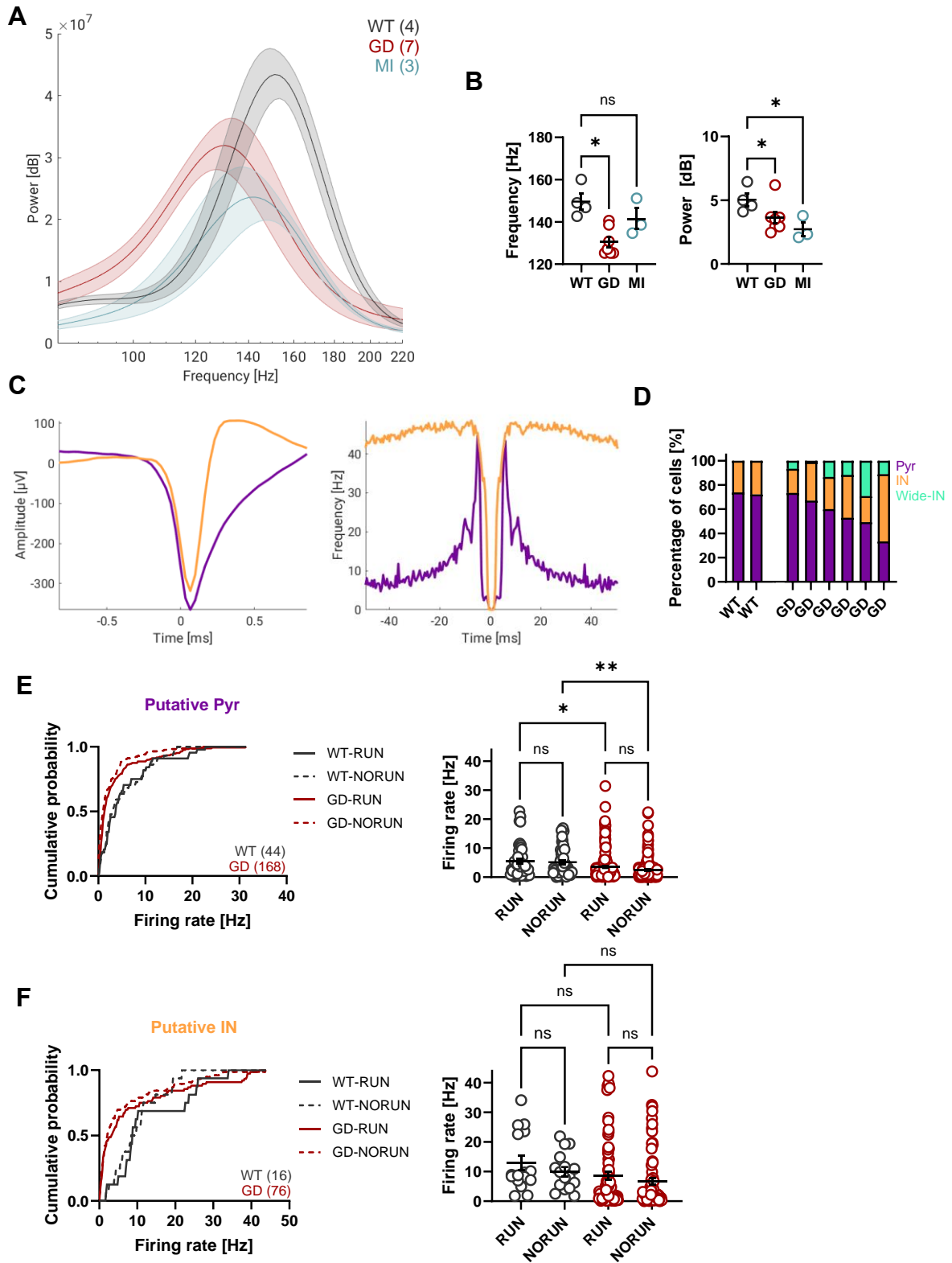


Figure 17: Reduced ripple frequency oscillations during immobility and decreased neuron firing rates of putative pyramidal neurons (Pyr) in GD mice.

Figure 17 continued on the next page.

Figure 17 continued: **A:** Wavelet power-spectrum-density (PSD) plot with mean \pm SEM is indicated using one recording per animal. **B:** The frequency and power for each detected ripple peak is indicated by the scatter plot. Each dot indicates an individual animal with mean \pm SEM presented (ns = not significant, * $p < 0.05$, one-way ANOVA Kruskal-Wallis test). **C:** Mean waveforms (left) and mean autocorrelogram (right) of a representative Pyr (purple) and IN (orange) from a GD mouse by *CellExplorer*. **D:** Percentage of cells that were recorded for two WT and six GD mice. Differentiation of cells (Pyr, IN, wide-shaped interneurons (Wide-IN)) was automatically performed by *CellExplorer*. **E:** Left: Cumulative probability distribution of the firing rate for putative Pyr during RUN and NORUN for both WT and GD indicating lower firing rates in GD neurons. Number of cells from two WT and six GD animals are indicated in brackets. Right: Firing rates of WT and GD neurons revealed significantly less firing rates in GD mice during RUN and NORUN (ns = not significant, * $p < 0.05$, ** $p < 0.01$, one-way ANOVA, Šídák's multiple comparisons test). Each dot indicates an individual neuron with mean \pm SEM presented. **F:** same as E: but for putative IN.

3.8 | Floxed GD mice exhibited spontaneous epileptic seizures comparable to GD mice

In collaboration with the *In vivo* Research Facility/Transgenic Core of the Cologne Excellence Cluster for Aging and Aging-Associated Diseases (CECAD), we generated a new mouse line, in which exon 4 of *Hcn1* containing the G380D mutation is flanked by loxP sites (Fig. 18A). This new line, here further referred to as FLHGD, exhibited spontaneous epileptic seizures, similar to GD mice without loxP sites (Fig. 18B). This observation was made in two implanted FLHGD mice via ECoG recordings. Since it was a newly generated mouse line, initial efforts focused on establishing and genotyping this mouse line.

Three distinct polymerase chain reactions (PCRs) were employed to amplify the entire construct for WT control (PCR WT), the loxP sites (PCR loxP), and the G380D mutation (PCR Mut; Fig. 18C). Unexpectedly, FLHGD mice initially displayed a higher mortality rate than that of GD animals, with survival decreasing to 43 % by the age of 24 weeks as compared to 76 % in GD animals (Fig. 18D, FLHGD-LEV). To improve survival during the establishment of the FLHGD mouse line, an ASM treatment with LEV was initiated. Unlike other sodium channel blockers, LEV had been shown to reduce epileptiform spiking activity in a gain-of-function *HCN1* mouse model *Hcn1*^{M294L/+} (Bleakley et al., 2023). LEV treatment started before birth by providing the pregnant mouse with LEV water and continued thereafter. Although the survival rate of FLHGD mice without LEV treatment (FLHGD-LEV) was not significantly different from that of FLHGD mice receiving LEV treatment (FLHGD+LEV), there was a trend towards improved survival rates, similar to those observed in GD mice. The survival rate of FLHGD+LEV stabilized at 68 % after around 19 weeks of age (Fig 18D).

Overall, these findings suggest that LEV treatment had a beneficial effect on this mouse line, as it modestly improved the survival rate of FLHGD mice. Due to the loxP sites, these mice were used for further breeding with cre-driver mouse lines to remove the mutated allele from distinct neuron types.

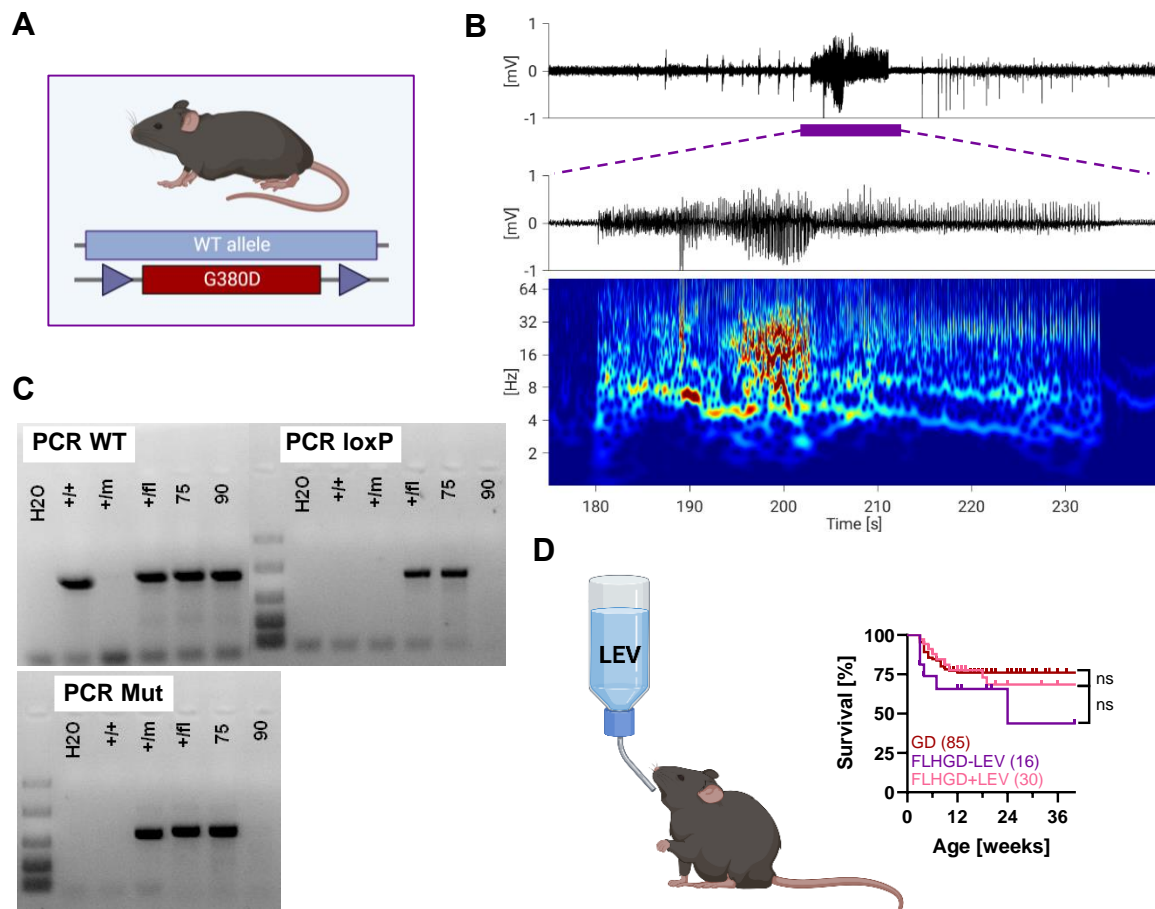


Figure 18: FLHGD mice exhibited spontaneous epileptic seizures similar to those observed in GD mice. **A:** Schematic representation of the G380D mutation flanked by loxP sites in FLHGD mice (created by BioRender.com). **B:** Example of a spontaneous seizure in an FLHGD mouse. Upper trace: ECoG signal in mV with the seizure marked by a purple bar. Middle trace: zoomed-in section of the ECoG signal in mV. Lower trace: corresponding time-frequency spectrogram in seconds and Hz, with warm colors indicating high power and cold colors indicating low power. **C:** Genotyping examples distinguishing WT from FLHGD mice. PCR WT amplified a large DNA construct in exon 4, including both the mutation and the loxP sites; PCR loxP amplified the loxP sites; PCR Mut amplified the G380D mutation. H₂O = water control, +/+ = WT, +/m = G380D mutation, +/fl = loxP sites including the mutation. In this example, number 75 represented an FLHGD mouse and number 90 represented a WT mouse. **D:** Left: Schematic illustration of an FLHGD mouse receiving levetiracetam (LEV) treatment through the drinking water (created by BioRender.com). Right: Kaplan-Meier survival curves comparing the mortality of FLHGD treated without (FLHGD-LEV) or with (FLHGD+LEV) LEV, using the survival of GD mice as a reference (ns = not significant, log-rank Mantel-Cox test).

3.9 | Removing the G380D mutation from Gad2+ interneurons resulted in seizure-free GDGAD mice

Due to the presence of loxP sites flanking the G380D mutation, the newly established mouse line FLHGD+LEV was used to conditionally remove this mutation in a neuron-specific manner. In detail, by crossing FLHGD+LEV male mice with Gad2-cre female mice, the resulting mouse line, referred to as GDGAD, had the mutation removed in all Gad2-positive (Gad2+) interneurons (Fig. 19A), rendering the mutant allele non-functional and effectively creating a heterozygous HCN1 knockout in these neurons. Since the offspring from these breedings included WT, WT-Gad2-cre, FLHGD, and GDGAD mice, LEV treatment continued until genotyping was completed. After genotyping, LEV-water was replaced by regular drinking water for WT, WT-Gad2-cre and GDGAD mice, with no adverse effects observed in these groups (data not shown). FLHGD mice continued with LEV treatment. Consequently, all GDGAD mice in this study received LEV until approximately six weeks of age.

ECoG recordings were conducted on six GDGAD mice to examine their cortical activity and the absence or presence of seizure. No spontaneous epileptic seizures were observed in any of the GDGAD mice during the recorded period of one to two weeks (Fig. 19B). Additionally, administration of LTG to one animal did not induce epileptic seizures (data not shown). There were no cases of spontaneous death among GDGAD mice, resulting in a survival rate of 100 % (Fig. 19C). Notably, both male (11 ± 1.2 g) and female (10.6 ± 0.4 g) GDGAD mice remained significantly lighter than WT animals at four weeks of age, similar to the results obtained for GD mice (Fig. 19D). Furthermore, when tested in the OF (Fig. 19E), GDGAD mice displayed an increased distance moved, lack of habituation to the arena, and higher velocity compared to WT animals. However, unlike GD mice, the occupation ratio indicating time spent in the border area versus the center area did not differ significantly from WT mice, (Fig. 19F).

In summary, although GDGAD mice did not exhibit seizures or an increased mortality rate, they still presented with behavioral comorbidities, such as reduced body weight and locomotor hyperactivity, similar to GD mice.

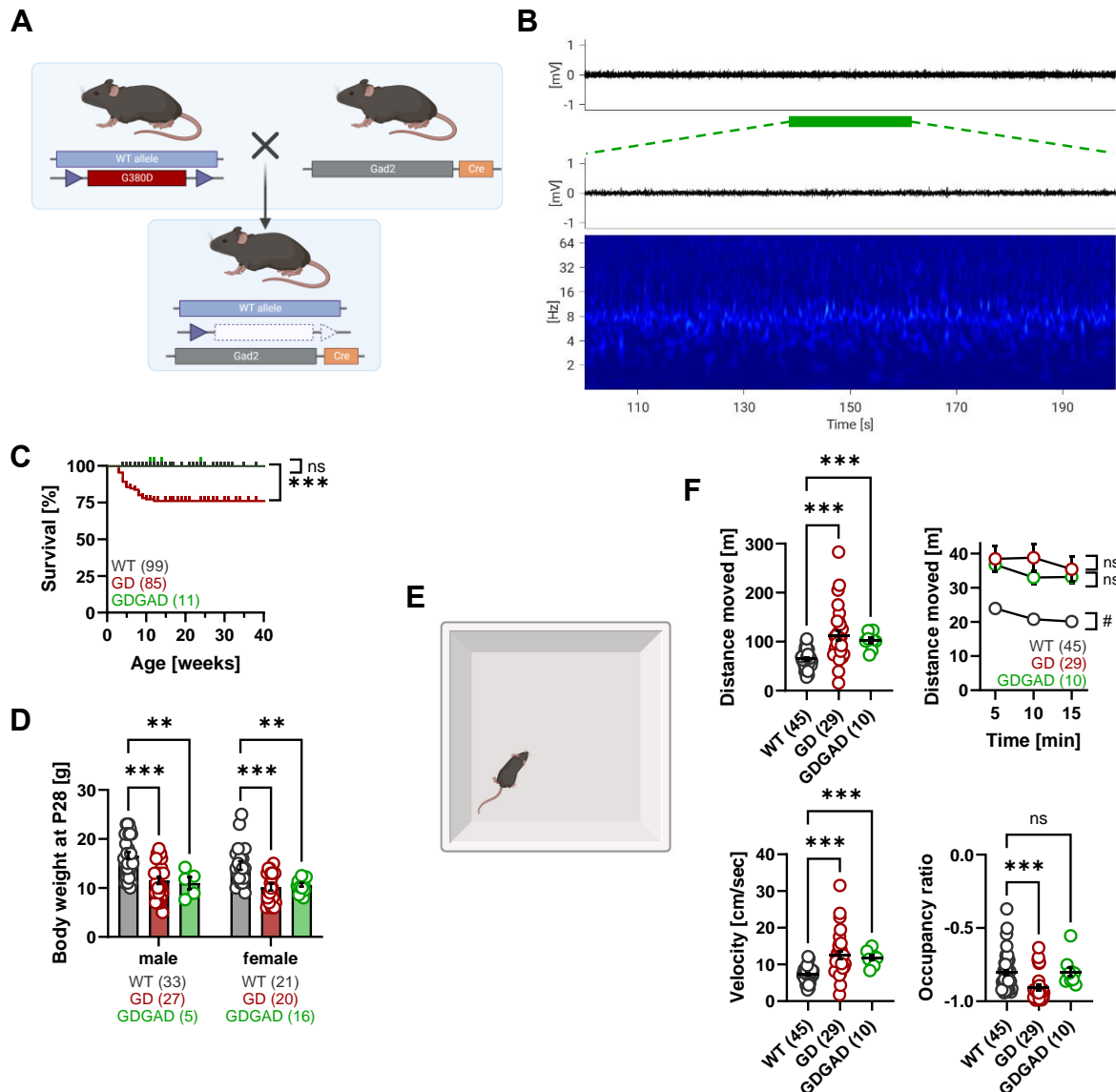


Figure 19: GDGAD mice did not exhibit spontaneous epileptic seizures, but still had behavioral comorbidities.

A: Scheme of crossing FLHGD mice with Gad2-cre animals that resulted in GDGAD mice, where the G380D mutation was removed from all Gad2+ interneurons (created by BioRender.com). **B:** Example of normal brain activity in a GDGAD mouse. Upper trace: ECoG signal in mV with the green bar marking the zoomed in part displayed in the middle trace. Lower trace: corresponding time-frequency spectrogram in seconds and Hz, respectively. Warm colors indicate high power; cold colors indicate low power. In a total of six GDGAD mice, no spontaneous epileptic seizures were detected during the recorded time period. Note: these mice received LEV in the first six weeks of life. **C:** Kaplan-Meier survival curve indicated no spontaneous death in GDGAD mice compared to WT animals (ns = not significant, *** $p < 0.001$, log-rank Mantel-Cox test). **D:** Body weights at P28 comparing male and female WT, GD, and GDGAD mice, with GD and GDGAD mice being lighter than WT littermates. **E:** Schematic representation of the open field (OF) arena (created by BioRender.com). **F:** GD and GDGAD mice showed increased total distance moved and velocity, but the occupation ratio indicated that GDGAD mice spent more time at the center area of the arena as observed for WT littermates (ns = not significant, *** $p < 0.001$, Mann-Whitney U test). Each dot indicates an individual animal with mean \pm SEM presented.

Figure 19 continued on the next page.

Figure 19 continued: For distance moved over time, GD and GDGAD mice did not show a habituation to the arena, as observed in WT mice (ns = not significant, # $p < 0.05$, effect of *time*, two-way repeated-measures ANOVA having *genotype* and *time* as grouping factors). Data represent mean \pm SEM (note that smaller error bars may be hidden by the circles representing the mean). Note: ten WT animals from GDGAD mouse line were additionally added to the WT GD mice. The number of animals is depicted in each plot in brackets. For visualization and comparison, the data from GD animals is also displayed.

3.9.1 | DeltaFosB immunoreactivity in the hippocampus

DeltaFosB is an activity-dependent transcription factor commonly used to identify the presence of epileptic seizures by marking increased activity of cells. Unlike other epileptic markers, deltaFosB accumulates in the cells due to its relatively long half-life (Corbett et al., 2017). In the hippocampus, the granule cell layer of the dentate gyrus of mice expressing G380D in all neurons prominently displays increased deltaFosB staining, indicating increased neuronal activity (Fig. 20). Representative images from mice carrying the G380D mutation, including GD, FLHGD-LEV, and FLHGD+LEV, showed a strong deltaFosB staining in the granule cell layer, whereas this was not observed in WT and GDGAD (Fig. 20A). Quantifications of the staining intensity demonstrated significantly higher average grey values for GD (3695 ± 365 au), FLHGD-LEV (3219 ± 488 au), and FLHGD+LEV (4396 ± 254 au) compared to WT mice (1628 ± 31 au). There was no significant difference in deltaFosB staining between WT and GDGAD mice (GDGAD: 1478 ± 44 au), suggesting that GDGAD mice did not exhibit spontaneous epileptic seizures or increased activity, likely due to the removal of the G380D mutation from all *Gad2*⁺ interneurons, as confirmed by the absence of seizures in six ECoG-recorded GDGAD animals. Despite a slight improvement in the survival rate of FLHGD+LEV following LEV treatment, it did not change the seizure phenotype (Fig. 20B).

These results support the hypothesis that the G380D mutation causes an interneuronopathy, as evidenced by the absence of epileptic seizures in GDGAD mice, as well as in brain tissue after deltaFosB staining. However, it remains unclear to what extent LEV treatment during the early weeks of life may have influenced brain activity in GDGAD mice.

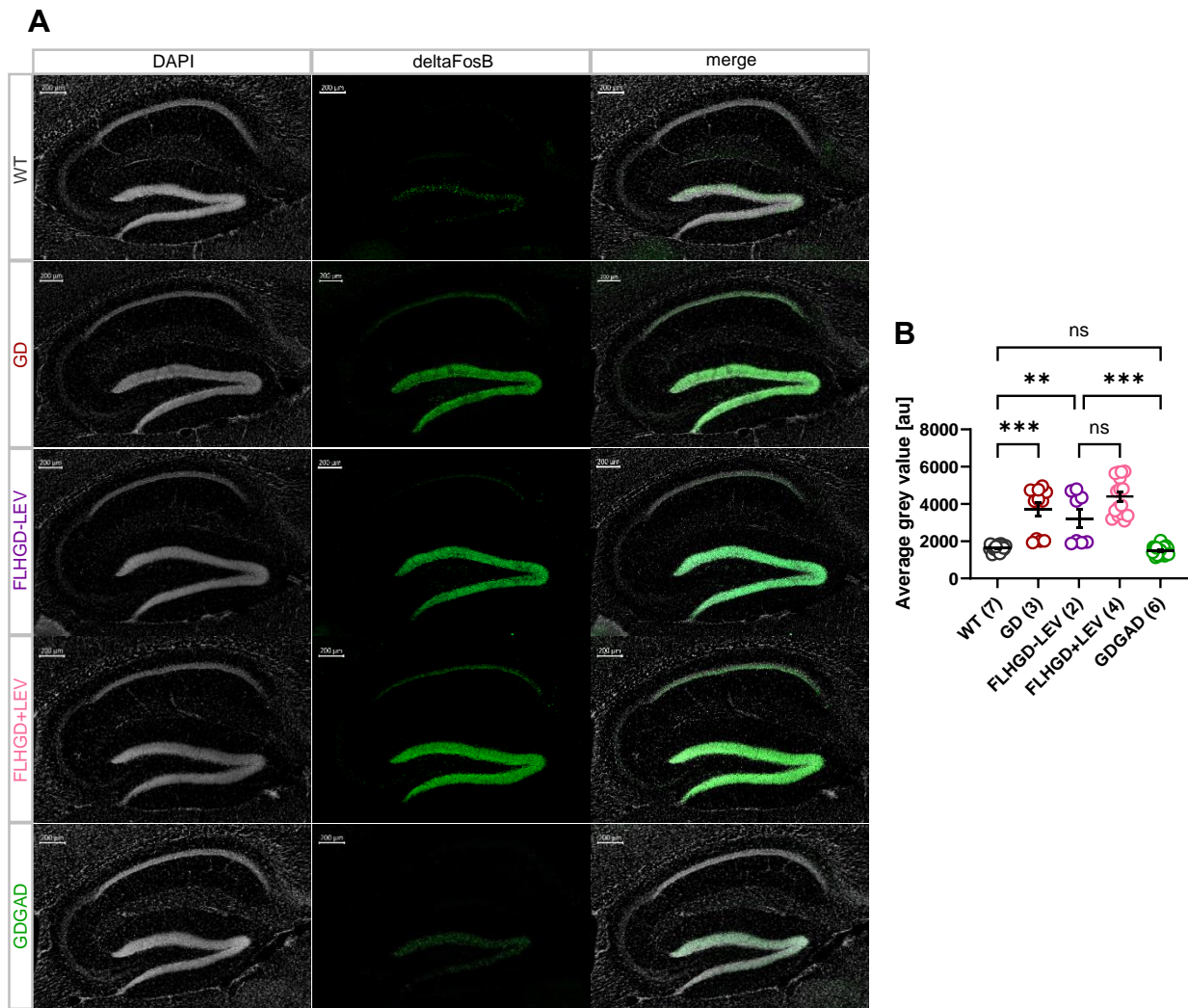


Figure 20: DeltaFosB immunoreactivity in hippocampal brain tissue in different mouse models (modified figure from Weber, Bachelor's Thesis, 2024). **A:** Representative sagittal brain sections stained for deltaFosB are displayed for the following groups (from top to bottom): WT, GD, FLHGD-LEV, FLHGD+LEV, and GDGAD. The first column represents 4',6-diamidino-2-phenylindole (DAPI) staining with marked cell nuclei in grey, the second column displays deltaFosB in green, and the third column shows the merged image of DAPI and deltaFosB. Images were captured using the AxioScan.Z1-068 microscope and processed with ZenBlue software. The scale bar represents 200 μ m. **B:** Quantification of deltaFosB immunoreactivity was performed in the granule cell layer of the dentate gyrus of the hippocampus for the five groups. The average grey value in arbitrary units (au) indicated the summed pixel intensity of the detected emission divided by the number of pixels (ns = not significant, ** $p < 0.01$, *** $p < 0.001$, one-way ANOVA Kruskal-Wallis test). The following numbers of brain sections were used: WT (26), GD (12), FLHGD-LEV (8), FLHGD+LEV (16), GDGAD (23). All mice were between 11 and 16 weeks old. The number of animals is depicted in brackets. Each dot indicates an analyzed brain section with mean \pm SEM presented.

3.9.2 | Reduced cortical low and high gamma oscillation frequency and power during REM sleep in GDGAD mice

GDGAD mice did not exhibit spontaneous epileptic seizures or spontaneous deaths. However, they displayed developmental and behavioral comorbidities, such as changes in body weight and locomotion. To determine whether cortical activity differs in these mice, similar to what was observed in GD animals, ECoG recordings were used to analyze REM, SWS, and ACTIVE periods, comparing the results with those from WT and GD animals. PSD plots (Fig. 21A) and the corresponding *foof* analysis (Fig. 21B) revealed that during REM sleep, unlike GD animals, GDGAD mice exhibited theta frequency oscillations similar to WT mice but with a reduced theta power (5.4 ± 0.7 dB versus 7.4 ± 0.3 dB). Similar to GD mice, GDGAD mice demonstrated reduced low gamma (64 ± 0.6 Hz) and high gamma (110.3 ± 1.1 Hz) frequencies along with decreased power (Fig. 21B, left column). During SWS, GDGAD mice indicated decreased theta frequency (7.8 ± 0.2 Hz) compared to WT animals, unlike GD mice (Fig. 21B, middle column). During the ACTIVE period, GDGAD mice, like GD animals, exhibited reduced theta (8.3 ± 0.1 Hz) and high gamma (97.4 ± 6.8 Hz) frequency compared to WT (Fig. 21B, right column).

Overall, these findings indicate that while GDGAD mice did not display epileptic seizures, their cortical activity still seemed to be altered compared to WT mice, particularly in theta and gamma frequencies. This suggests that the G380D mutation, even when removed from interneurons, still impacts cortical network function, resulting in specific electrophysiological changes.

Figure 21 continued on the next page.

Figure 21 continued: A: Power-spectrum-density (PSD) plots with frequency in Hz and power in dB for WT, GD, and GDGAD during REM, SWS and ACTIVE periods. The number of animals is depicted in brackets. Curves indicate mean \pm SEM. **B:** For nearly each mouse from WT, GD, and GDGAD, the *fooof* analysis revealed a frequency peak and a corresponding power value, which are plotted in scatter plots for REM (left column), SWS (middle column), and ACTIVE (right column) periods for theta (upper row), low gamma (middle row), and high gamma (lower row). Data represent mean \pm SEM (ns = not significant, * $p < 0.05$, ** $p < 0.01$, *** $p < 0.001$, one-way ANOVA Kruskal-Wallis test).

In contrast to GD animals, GDGAD mice did not demonstrate beta activity (Fig. 21A), unlike the strong beta peak observed in GD mice. Furthermore, the reduced aperiodic exponent investigated in GD mice during SWS was not present in GDGAD mice (Fig. 22). Here, no significant difference in the aperiodic exponent was observed when comparing GDGAD with WT mice across the brain states REM, SWS, and ACTIVE.

These findings suggest that the removal of the G380D mutation from *Gad2*⁺ interneurons in GDGAD mice may have normalized the E/I balance, preventing the shift observed in GD mice, and thus epileptic seizures.

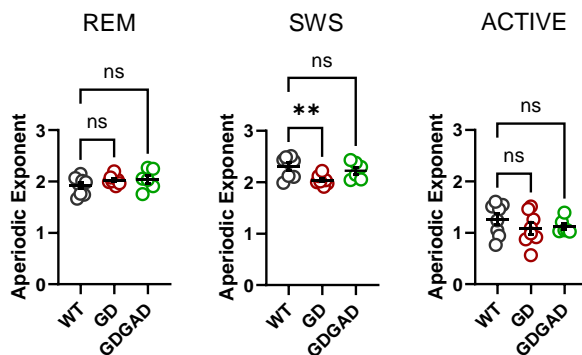


Figure 22: The aperiodic exponent was not different during SWS in GDGAD mice compared to WT, as observed in GD mice. For different brain states, the aperiodic exponent indicated a reduction for GD mice during SWS, when comparing with WT mice, but not for GDGAD animals (ns = not significant, ** $p < 0.01$, one-way ANOVA Kruskal-Wallis test).

4. | Discussion

This study aimed at characterizing two mouse lines, each carrying a *de novo* human point mutation in *Hcn1* associated with DEEs. Mice with the G380D variant (*Hcn1*^{G380D} or GD) and the M142I variant (*Hcn1*^{M142I} or MI) both exhibited spontaneous epileptic seizures. This is a key feature for studying these mutations in more detail, as the seizures closely mimic the human condition, making these mouse lines valuable models for epilepsy research. In addition to spontaneous seizures, mice with these heterozygous point mutations displayed high mortality rates and reduced body weights at different ages (Kasemir, Master's Thesis, 2020).

As established previously, ECoG recordings were used to detect spontaneous epileptic seizures in these mice. Video monitoring revealed that the seizure severity was greater in MI mice compared to GD mice. Furthermore, administration of ASM like LTG and PHT led to an increase in seizure activity in both mouse lines, indicating a paradoxical adverse response to those sodium channel blockers.

Given that human patients with *HCNI* mutations present various comorbidities, behavioral characterization showed that both GD and MI mice exhibited locomotor hyperactivity, memory impairment in OLM task, and reduced anxiety levels. Moreover, GD mice also showed minor changes in somatomotor development regarding neonatal reflex tests, with persistent motor coordination deficits in adult mice, and deficits in spatial working memory in the Y-maze. Furthermore, analysis of ECoG recordings revealed altered cortical oscillations in GD mice with reduced low and high gamma frequencies and power during REM sleep. Hippocampal oscillatory changes in SLM and SP were observed when mice were recorded in the MHC using silicon probes. While MI mice exhibited a more severe epilepsy phenotype, GD mice demonstrated broader impairments in cortical and hippocampal oscillations due to the mutation.

To explore the role of G380D in specific neuronal populations, a conditional mouse line (FLHGD) was generated, with the G380D mutation flanked by loxP sites. Crossing these mice with Gad2-cre animals resulted in GDGAD mice, which did not exhibit spontaneous epileptic seizures, but behavioral comorbidities like reduced body weight, locomotor hyperactivity, and decreased gamma frequency during REM sleep were observed.

4.1 | Dysfunctional HCN1 channels result in epileptic seizures

In human patients with the G391D variant in *HCN1*, NOEE is characterized by prolonged daily tonic-clonic seizures, microcephaly, and early death. This mutation is located at the S6 transmembrane domain near the pore region of the channel. The glycine-to-aspartic acid substitution causes a conformational change that leads to strong binding of K^+ ions inside the channel. As a result, the channel malfunctions, allowing Na^+ ions to pass through the pore, leading to a “leaky” HCN1 channel (Marini et al., 2018; Merseburg et al., 2022). Furthermore, this persistent Na^+ influx shifts the RMP to more depolarized potentials, making those neurons more excitable and vulnerable to action potential generation, as observed in the corresponding GD mouse model (Fig. 6). In addition to this gain-of-function Na^+ leak current, the G380D variant in mice further leads to a loss-of-function channel, characterized by reduced HCN1 activation and protein expression, possibly due to impaired stability or membrane targeting (Porro et al., 2021). In GD mice, current clamp experiments indicated that CA1 pyramidal neurons showed significantly reduced action potential firing rates upon one-second-long depolarization and a nearly absent voltage sag (Fig. 6). In addition to pyramidal neurons, HCN1 channels are also expressed in PV+ interneurons, particularly in cerebellar basket cells. Here, the HCN1 protein expression was nearly absent in GD mice, suggesting impaired trafficking, misfolding, or degradation of these channels in GD animals (Merseburg et al., 2022). Furthermore, in the “pinceau” structure, where basket cell terminals contact the axon initial segment of Purkinje neurons, the expression of K^+ channels like $K_v1.2$ and the Na^+/K^+ pump were also significantly reduced (Merseburg et al., 2022). Since HCN1 channels and the Na^+/K^+ pump interact in PV+ interneurons, and because these interneurons are more susceptible to cellular and oxidative stress, the reduced protein expression might contribute to the epilepsy phenotype (Kann, 2016; Roth and Hu, 2020).

Human patients carrying the M153I variant exhibit EIEE with weekly to daily focal and tonic-clonic seizures. This mutation – located at the S1 transmembrane domain – causes a gain-of-function in HCN1 channels, leading to activation of I_h at more depolarized membrane potentials, as demonstrated in HEK-cells (Marini et al., 2018). Similar to GD mice, MI mice showed reduced action potential firing and voltage sag in CA1 pyramidal neurons (Fig. 6). While HCN1 protein levels were slightly reduced in the distal dendrites of pyramidal neurons compared to WT neurons, the expression of HCN1 in PV+ interneurons, as well as $K_v1.2$ and the Na^+/K^+ pump labeling remains normal in MI mice

(Merseburg et al., 2022). However, the mutation accelerated channel activation kinetics resulting in faster and higher Na^+ ion flow, which might be the cause of the seizure phenotype (Marini et al., 2018).

4.2 | Paradoxical response to anti-seizure medications in both GD and MI mice

Administration of LTG or PHT to GD and MI mice induced epileptic seizures for both medications about 1.5-2.5 hours after injection (Fig. 13). LTG is a sodium channel blocker and a well-established ASM used to treat various types of epileptic seizures, including focal and tonic-clonic seizures, as well as Lennox-Gastaut syndrome (Brigo et al., 2021). PHT, which also acts as a sodium channel blocker, has been shown to reduce seizures in other channelopathies, such as those involving gain-of-function mutations in *SCN2A* (Dilena et al., 2017). However, despite their efficacy in human patients, our mouse models GD and MI demonstrated paradoxical responses to these ASMs, as previously reported in patients with *HCN1*-linked DEE (Marini et al., 2018; Nava et al., 2014). This phenomenon was also reported for patients with Dravet syndrome (Perucca and Perucca, 2019). Dravet syndrome patients carry a loss-of-function mutation in *SCN1A* encoding for the sodium channel $\text{Na}_v1.1$, and it was investigated that epileptic seizures are generated by reduced excitability of inhibitory interneurons – a condition referred to as interneuronopathy (Catterall, 2018). In this context, sodium channel blockers may further suppress the already impaired inhibitory function, leading to increased network excitability. In PV⁺ interneurons, high firing rates depend on Na^+/K^+ pumps, which are highly expressed at the axons, where Na^+ influx activates the pump, leading to hyperpolarization (Peng et al., 1997). HCN channels are also highly expressed at axonal terminals in PV⁺ interneurons, and they may co-interact with Na^+/K^+ pumps to facilitate fast firing and action potential propagation. Blocking HCN channels in PV⁺ interneurons resulted in reduced action potential firing and diminished perisomatic inhibition (Roth and Hu, 2020). In GD and MI mice, dysfunctional HCN1 channels might lead to decreased GABAergic inhibitory input onto excitatory neurons, disrupting the balance between excitation and inhibition. This imbalance could be further destabilized by sodium channel blockers, as observed in Dravet syndrome patients, which might indicate altered GABAergic inhibition also in our mouse models.

4.3 | Behavioral comorbidities are potentially due to *HCN1* mutations

Similar to human patients carrying *HCN1* mutations, the GD and MI mouse models, which mimic the two human point mutations, exhibited behavioral comorbidities in addition to epileptic seizures. While the G391D mutation in two patients led to NOEE and early intellectual disabilities, GD pups did not display major impairments in various reflex tests during their first week of life (Fig. 7). They showed slightly delayed performances in the righting reflex but performed better during the geotactic reflex test (Fig. 7). Although the developmental stage of mice from P2 to P8 aligns with the *in utero* period around the third trimester in humans (Clancy et al., 2001; Delage et al., 2021), further behavioral testing of GD mice is required to replicate the full spectrum of comorbidities observed in human *HCN1* patients. However, preliminary data from our laboratory revealed spontaneous epileptic seizures in GD mice at P6 during acute silicon probe recordings, potentially indicating that abnormal network activity may be present in human patients already before birth.

A study by Fadila et al. (2020) found that Dravet syndrome mice exhibited locomotor hyperactivity in the open field before the onset of epileptic seizures, suggesting that behavioral comorbidities may be independent of convulsive seizures (Fadila et al., 2020). Conversely, another study demonstrated that induction of frequent seizures can trigger spontaneous seizures, cognitive deficits, as well as locomotor hyperactivity (Fadila et al., 2020; Salgueiro-Pereira et al., 2019). Although a conclusion cannot be made about whether the behavioral comorbidities observed in GD and MI mice – such as locomotor hyperactivity (Fig. 8), motor coordination deficits (Fig. 8), altered memory (Fig. 9), and anxiety behavior (Fig. 10) – are a consequence or cause of epileptic seizures, it indicates that the dysfunctional *HCN1* channels caused by the G380D and M142I mutations led to these behavioral comorbidities in GD and MI mice, respectively.

The hippocampus plays essential roles in memory encoding and consolidation processes for tests like alternation in the Y-maze and OLM, as well as CFC (Barker and Warburton, 2011; Hölder et al., 2015; Maren et al., 2013). Given that *HCN1* channels are highly expressed in the hippocampus (Santoro and Shah, 2020), abnormal channel function due to the two mutations in GD and MI mice led to altered performance in these behavioral tests compared to WT. This is consistent with findings that showed *HCN1* knockdown in the prefrontal cortex impaired memory function in these mice (Thuault et al., 2013).

In the EPM and CRC experiments assessing anxiety, both GD and MI mice displayed reduced anxiety-like behavior. It is possible that, due to their hyperactivity, these mice exhibited flight responses rather than freezing during the CFC, potentially masking fear-related behavior. This flight behavior was also observed in a mouse model of autism spectrum disorder (Anstey et al., 2022), as well as in mice mimicking schizophrenia. These schizophrenia mice had reduced IPSCs in cortex and hippocampus, and besides hyperactivity, they showed decreased freezing levels (Mao et al., 2009). However, the results from GD and MI mice make it difficult to definitely conclude reduced anxiety levels. In the OF test, for instance, mice with increased anxiety typically spent more time at the border area rather than in the center of the arena (Seibenhener and Wooten, 2015). This was also observed for GD and MI mice that spent more time at the border area (Fig. 8B). A possible explanation for this behavior may be impaired vision. Previous studies on another HCN1 variant mouse model (*Hcn1*^{M294L}) revealed decreased photoreceptor sensitivity to light (Zhao et al., 2023). Since HCN1 channels are expressed in retinal photoreceptors (Moosmang et al., 2001), mutations in these channels could potentially result in visual impairment. The preference of GD and MI mice for the border area could, therefore, also be linked to impaired vision. We observed that these mice often run along the border for orientation, frequently bumping into the corners of the arena to change running direction. Additionally, GD mice struggled to grasp the tip of the pole during the Pole test and ran off the edge of open arms in the EPM, which may further suggest visual deficits. Unfortunately, due to the locomotor hyperactivity, the Optodrum test (Kretschmer et al., 2015) yielded inconclusive results and visual acuity in GD mice could not be behaviorally tested.

4.4 | Alterations in cortical oscillations in GD mice result from dysfunctional HCN1 channels

After performing ECoG recordings and analyzing cortical oscillations, we observed that GD mice exhibited reduced low and high gamma oscillation frequencies and power, particularly during REM sleep (Fig. 11B). Gamma activity, which occurs not only during wakefulness but also during sleep, is a hallmark of high-frequency brain activity (Buzsáki and Wang, 2012). REM sleep is characterized by both theta and gamma oscillations, with gamma rhythms that are driven by fast-spiking GABAergic interneurons providing rhythmic inhibitory inputs to pyramidal neurons (Buzsáki and Wang, 2012; Byron et al., 2021). These interneurons, primarily PV⁺ interneuron basket cells expressing the

Ca^{2+} -binding protein parvalbumin, are critical for maintaining gamma oscillations, as inhibiting them suppresses gamma activity *in vivo* (Sohal et al., 2009). Moreover, gamma oscillations reflect the synchronous firing of neuronal populations and depend on rhythmic inhibitory postsynaptic potentials (IPSPs). Early studies in the hippocampus demonstrated that intracellular recordings from CA1 and CA3 pyramidal neurons in rats showed currents linked to gamma oscillations (Colgin and Moser, 2010; Soltesz and Deschênes, 1993). Here, chloride injections induced depolarizing potentials in pyramidal neurons, which synchronized with gamma rhythms, supporting the idea that gamma oscillations represent IPSPs in pyramidal neurons. Further recordings from PV+ basket cells confirmed their phase-locked firing to gamma oscillations and their direct role in generating IPSPs in pyramidal neurons (Colgin and Moser, 2010; Penttonen et al., 1998). Alterations in gamma oscillations have previously been reported for other types of neurodegenerative diseases, such as schizophrenia, autism spectrum disorder, and Alzheimer's disease, where dysfunctional inhibitory interneurons have been implicated (Byron et al., 2021; Rojas and Wilson, 2014; Uhlhaas and Singer, 2010).

In our GD mice, reduced cortical gamma oscillations during REM sleep suggest deficits in GABAergic interneuron function due to the G380D mutation. This reduced inhibition may indicate an imbalance between excitation and inhibition, as reflected by the altered aperiodic exponent during SWS (Fig. 12C). Such an imbalance could also contribute to the spontaneous epileptic seizures observed in these mice. No seizures were detected during sleep or sleep-wake transitions; they predominantly occurred during wakefulness (data not shown). A slight reduction in high gamma frequency during AWAKE period (Fig. 11B) further supports the hypothesis of an interneuronopathy in GD animals.

In addition to reduced gamma activity, GD mice exhibited beta oscillations during REM sleep (Fig. 12A+B). However, this finding was not observed for WT or MI mice. The correlation between a neurodegenerative disease and increased beta oscillations has been identified in other models, such as a transgenic mouse model, where beta activity was observed exclusively during REM sleep (Jeantet et al., 2013). Moreover, a study by Chen et al. (2017) investigated beta and gamma oscillations in the primary visual cortex and found that beta oscillations were primarily associated with SST+ interneurons, while PV+ interneurons were linked to gamma oscillations (Chen et al., 2017). Both SST+ and PV+ interneurons play crucial roles in regulating cortical oscillations, with HCN1 channels being expressed in PV+ interneuron axonal terminals, and in SST+ interneurons HCN channels are found at the soma and in dendrites (Albertson et al., 2017). Although SST+ interneurons mainly express the HCN2 subunit, it is proposed that HCN1 and HCN2 form a heterotetrameric structure,

particularly in hippocampal oriens-lacunosum moleculare region (Matt, Doctoral Thesis, 2010). This suggests that altered HCN1 function in these neuron types may underlie the increased beta activity in GD mice.

4.5 | Alterations in hippocampal oscillations in GD mice result from dysfunctional HCN1 channels

In addition to cortical data from ECoG recordings, hippocampal analysis of SP LFPs revealed significantly reduced high gamma oscillations in GD mice compared to WT during immobility periods in the MHC (Fig. 15B). These reduced oscillations may be attributed to dysfunctional inhibition of PV+ interneurons onto pyramidal neurons in GD mice. Several mechanisms could explain this dysfunction. One possibility is a firing deficit of PV+ interneurons due to the G380D mutation. The analysis of neuron firing rates showed a significant reduction in pyramidal neuron activity during RUN and NORUN periods (Fig. 17E). These extracellular *in vivo* recordings align with *in vitro* findings from CA1 pyramidal neurons, where a reduction in action potential firing was observed in GD mice (Fig. 6C). Together, these observations suggest that the G380D mutation in HCN1 channels leads to reduced CA1 excitatory neuron activity.

Normal brain function relies on a balance between excitation and inhibition (Sohal and Rubenstein, 2019). The reduced firing rates in CA1 pyramidal neurons may lead to less excitation of inhibitory interneurons and thus suggests deficits in inhibition, that may disrupt network balance. This imbalance could result from deficits in feed-forward inhibition, where excitatory neurons typically activate inhibitory neurons, which in turn suppress the target neuron activity (Panthi and Leitch, 2019; Sohal et al., 2009). In a previous study, chronic silencing of CA1 pyramidal neuron neurotransmission in a conditional mouse model led to a significant reduction in feedback inhibition, highlighting the critical role of excitation-inhibition interplay (Adaikkan et al., 2024). Unit recordings from hippocampal CA1 showed reduced firing rates in pyramidal neurons in GD animals, possibly resulting in less excitation of putative inhibitory interneurons (Fig. 17F). Although no significant difference was found in putative inhibitory interneurons between WT and GD neurons during RUN and NORUN periods, the left shift in the firing rates below 15 Hz suggests that not only fast-spiking PV+ basket cells, but also

axo-axonic PV⁺ cells (chandelier cells), bistratified PV⁺ cells, or SST⁺ interneurons may have reduced firing rates in our GD mouse model (Tzilivaki et al., 2023; Varga et al., 2014).

Despite PV⁺ interneurons being identified by their fast-spiking properties, recordings from the somatosensory cortex in WT and a Dravet syndrome mouse model showed lower firing rates (1-15 Hz) without significant differences between the groups (De Stasi et al., 2016). For higher firing rates (> 15 Hz), WT neurons fired more during RUN than NORUN periods (Fig. 17F). These neurons could indicate PV⁺ interneurons, which are known to increase their action potential firing with increased movements (Yao et al., 2020). In GD mice, this difference between RUN-NORUN firing rates was less pronounced, suggesting potential deficits in PV⁺ interneuron activity, although this conclusion is preliminary due to the small sample size.

Another potential cause of dysfunctional inhibition may have its origin in synaptic transmission deficits of neurons. Since preliminary data suggests no major differences in interneuron firing between WT and GD neurons, synaptic transmission from PV⁺ interneurons onto pyramidal neurons might be altered by the G380D mutation. HCN1 channels are expressed presynaptically in PV⁺ interneurons and modulate hippocampal activity (Bock et al., 2022). These ion channels help regulate action potential initiation and persistent firing in PV⁺ interneurons (Elgueta et al., 2015; Roth and Hu, 2020). Presynaptically, HCN1 channels are involved in inhibitory synaptic transmission. Blocking HCN1 channels with ZD7288 or using an *Hcn1* knockout mouse model showed reduced amplitudes of inhibitory postsynaptic currents (IPSC) in pyramidal neurons (Bock et al., 2022; Nolan et al., 2003). The G380D mutation could similarly alter IPSCs, leading to deficits in GABA-filled vesicle release and reduced inhibitory input to pyramidal neurons, which could explain the reduced firing rates observed.

Another possibility is that structural changes in the synaptic cleft might contribute to synaptic transmission deficits. In mammals, the synaptic cleft is approximately 20 nm wide (Zuber et al., 2005). Changes involving an increase in the synaptic cleft, which could mean that although GABA-filled vesicles are released at the presynapse from PV⁺ interneurons, the amount of neurotransmitter may be too small and insufficient to generate an inhibitory effect. Altered synaptic transmission might also be found in the observed increased gamma oscillations in SLM of GD mice (Fig. 14B). Inputs to SLM originate from MEC layer III (Neves et al., 2008), and increased low gamma activity could result from altered excitatory neurotransmitter release, potentially driven by the *HCN1* mutation.

In a Dravet syndrome mouse model, ripple oscillations – critical for both short-term and long-term memory and learning – were found to have reduced frequency and diminished occurrence compared to WT animals (Cheah et al., 2019). Ripple activity depends on the proper function of PV+ interneurons, which closely interact with pyramidal neurons to generate fast oscillations in a 140-220 Hz frequency range (Schlingloff et al., 2014). Similar to Dravet syndrome mice, GD mice also showed a reduction in ripple frequency during immobility (Fig. 17A). Additionally, GD mice demonstrated poor performance in memory tasks such as the Y-maze and OLM. This aligns well with the significantly reduced awake ripple frequency observed in these animals in the MHC. As in the Dravet syndrome model, impaired PV+ interneuron function likely contributes to the reduced ripple activity observed in GD mice (Cheah et al., 2019). Together, these findings strongly support the hypothesis that GD animals exhibit an interneuronopathy.

4.6 | The HCN1 G380D variant results in an interneuronopathy

Given the more severe phenotype observed in human patients with the p.G391D variant (Marini et al., 2018) and in the GD mouse model, FLHGD mice were generated with the G380D mutation in exon 4 flanked by loxP sites. This approach allowed a conditional removal of the mutation from specific neuron types. Since most findings in GD mice pointed towards an interneuronopathy, it was hypothesized that removing the mutation from all inhibitory interneurons would prevent the epilepsy phenotype. To test this idea, FLHGD mice were crossed with Gad2-cre animals, resulting in GDGAD mice that expressed the G380D variant in all cells except Gad2+ interneurons. Gad2 is expressed as early as embryonic day 11 in mice (Taniguchi et al., 2011; Trifonov et al., 2014), meaning that the early removal of the mutation by the cre-recombinase prevented the development of dysfunctional HCN1 channels in inhibitory interneurons. Notably, it was confirmed that GDGAD mice did not exhibit spontaneous epileptic seizures, indicating that the deletion of the G380D mutation from Gad2+ interneurons prevented the epilepsy phenotype.

While the limited duration of telemetry recordings only provided a brief insight into ECoG data over several days, the absence of increased deltaFosB activity in the granule cell layer of the dentate gyrus suggests no increased neuronal activity or epileptic seizures in adult GDGAD mice (Fig. 20). Additionally, further analysis of the hippocampus using *Wisteria floribunda* agglutinin (WFA) to

mark perineuronal nets (Härtig et al., 2022), glial fibrillary acidic protein (GFAP) to label astrocytes (Hol and Pekny, 2015), and neuropeptide Y (NPY) found in GABAergic interneurons (Colmers and El Bahh, 2003) revealed normal staining intensities in GDGAD mice, similar to WT (Weber, Bachelor's thesis, 2024). In contrast, GD mice displayed increased staining intensities in all of these markers, indicating neuronal excitability and epileptic seizures. These results support the conclusion that the epilepsy phenotype was prevented in GDGAD mice due to G380D removal from Gad2⁺ interneurons.

Moreover, HCN1 staining in GDGAD mice showed reduced protein levels in distal dendrites of pyramidal neurons compared to WT, while synaptotagmin 2 (Syt2), a Ca²⁺ sensor for neurotransmitter-vesicle release, was also decreased in the middle molecular layer of the dentate gyrus, corresponding to the axons of stellate cells from the MEC (Witter, 2007; Weber, Bachelor's thesis, 2024). This confirms that the G380D mutation was specifically removed only from Gad2⁺ inhibitory neurons, while excitatory neurons remained affected, displaying the same results as seen in GD mice (Weber, Bachelor's thesis, 2024).

However, despite the striking and convincing evidence that the G380D mutation leads to an interneuronopathy, GDGAD mice still exhibited reduced body weights at P28, locomotor hyperactivity in the OF (Fig. 19), and similar reduction of gamma oscillations during REM sleep, as observed in GD animals (Fig. 21). Reducing the seizure phenotype but still showing behavioral comorbidities was already observed for other epilepsy mouse models, for example one mimicking focal cortical dysplasia, where, in this case, viral overexpression of K⁺ channels resulted in decreased excitability and neurotransmitter release (Almacellas Barbanoj et al., 2024). The observed behavioral hyperactivity in GDGAD mice may be due to other dysfunctional brain circuits that do not specifically depend on an interneuron rescue. In our laboratory, another mouse model expressing a dominant-negative HCN4 subunit (HCN-DN) was developed to conditionally suppress I_h in forebrain projection neurons (Matthias et al., 2023). These HCN-DN mice did not exhibit cortical excitability or epileptic seizures but displayed hyperlocomotion and stereotypical circling behaviors. The increased locomotion in HCN-DN mice is thought to result from an altered balance between striatal direct and indirect pathways and changes in corticostriatal communication in the basal ganglia (Matthias et al., 2023). This phenotype closely mirrors the one observed in GDGAD animals. Ablation of I_h in forebrain projection neurons in HCN-DN is similar to GDGAD mice, which express the G380D mutation in all cells except Gad2⁺ interneuron, meaning that HCN1-G380D is also present in forebrain

projection neurons. It is possible that both mouse lines share similar alterations in striatal pathway function, contributing to the hyperactivity observed in GDGAD mice, which needs to be investigated further.

Although GDGAD mice did not provide a definitive answer as to how the G380D mutation leads to deficits in interneuron firing or transmission, the prevention of the epilepsy phenotype strongly suggests the presence of an interneuronopathy when the G380D mutation is expressed. However, the persistence of reduced gamma oscillations may indicate a broader rhythmopathy rather than purely an interneuron dysfunction. In a rodent model of temporal lobe epilepsy, cognitive impairments and seizures were linked to a hippocampal theta rhythmopathy characterized by reduced theta power (Shuman et al., 2017). While theta oscillations appeared normal in GDGAD (as well as in GD) mice, gamma oscillations were reduced (Fig. 21). It has been shown that impaired coupling between theta and low gamma oscillations in stratum radiatum is associated with cognitive dysfunction (Lopez-Pigozzi et al., 2016), whereas the memory performance of GDGAD mice remains to be investigated. Nevertheless, gamma rhythmopathy may possibly contribute to the remaining comorbidities in these animals, which are linked to the G380D mutation.

4.7 | Future prospects

To further investigate the role of *HCN1*-linked DEEs, studying MI mice in more detail is important, as it provides a third mouse model (besides GD and *Hcn1*^{M294L}) mirroring human point mutations that lead to DEEs (Bleakley et al., 2021; Merseburg et al., 2022). While the M142I mutation in mice also resulted in behavioral comorbidities, they were not as severe as those observed in GD mice. Although major changes in cortical network activity have not been detected, alterations in the hippocampus may exist but are, for now, difficult to identify due to the small number of animals used for MHC recordings. Since MI mice also showed reduced firing rates in CA1 pyramidal neurons *in vitro* and increased epileptic seizures after ASM administration, hippocampal changes may still be present and need to be investigated *in vivo*. Depending on the result, conditionally removing the M142I mutation from specific neuron types may be considered.

To improve hippocampal recordings, exchanging Neuronexus with Neuropixel electrodes would significantly increase the number of recorded neurons for both, GD and MI mice (Fiáth et al., 2021).

This would allow for a more extensive dataset, including both pyramidal neurons and PV+ interneurons, which would help to determine if the firing rates of PV+ interneurons in GD mice *in vivo* differ from WT animals. Preliminary data from recent patch-clamp recordings of pyramidal neurons showed no significant difference between GD and WT neurons in miniature IPSC (mIPSC) frequency, suggesting normal presynaptic function, and no difference in mIPSC amplitude, indicating normal postsynaptic response to neurotransmitter release (Sakimoto et al., 2019). The next step involves patch-clamp recordings of layer V somatosensory cortical pyramidal neurons, as previously performed in another *HCN1* mouse model (*Hcn1*^{M294L}). In this model, layer V neurons were hyperexcitable, with a more depolarized RMP and increased action potential firing frequency compared to WT mice (Bleakley et al., 2021). While these mice only displayed interictal spikes without spontaneous epileptic seizures, GD and MI mice may share similar altered activity of layer V pyramidal neurons, which could be linked to their epileptic seizures and requires further investigations.

In this study, the findings supporting an interneuronopathy furthermore strengthen the hypothesis that PV+ interneurons may specifically be responsible for the phenotype observed in GD mice. Future studies would include crossing FLHGD mice with PV-cre animals to conditionally remove the G380D mutation from all PV+ interneurons. This would allow us to determine whether the phenotype of this new mouse line is similar to GDGAD mice, and if the G380D mutation would therefore be a PV+-interneuronopathy. Additionally, conditionally removing the mutation from SST+ or vasoactive intestinal polypeptide positive (VIP+) neurons and comparing their phenotypes with GDGAD mice would be possible to assess whether the seizure phenotype is also rescued in these animals. Another recently investigated inhibitory interneuron type is the neuron-derived neurotrophic factor positive (NDNF+) interneuron, found in neocortical layer I (Hartung et al., 2024). These cells not only inhibit pyramidal neurons but also regulate VIP+ and PV+ interneuron activity in layer II/III as top-down master regulators (Hartung et al., 2024). Investigating the role of NDNF+ interneurons and how they are involved in the phenotype of GD mice could be explored by removing HCN1 channels from these interneurons.

To further support the interneuronopathy hypothesis, FLHGD mice could also be crossed with empty spiracles homeobox 1 (*Emx1*)-cre animals, to remove the G380D mutation from excitatory neurons in neocortex and hippocampus (Gorski et al., 2002). We hypothesize that these mice would still exhibit spontaneous epileptic seizures, potentially with a more severe phenotype, but this may rescue the reduced gamma oscillation phenotype because of removing G380D from inhibitory interneurons.

Moreover, using Gad2-creER mice, cre-recombinase activity could be induced with tamoxifen (Taniguchi et al., 2011), allowing a temporal control of the G380D mutation in GABAergic interneurons. Previous studies in our laboratory with other mouse models have identified vulnerable periods during the first two to three postnatal weeks, whereas after treatments in this time window specific phenotypes such as epileptic seizures and comorbidities could be restored to WT levels in adult mice (Marguet et al., 2015; Matthias et al., 2023).

Investigating the role of specific interneuron types in *HCNI*-linked DEEs will be crucial for understanding the underlying mechanisms of epilepsy and comorbidities in GD and MI mice, which may further offer therapeutic insights.

4.8 | Conclusions

Based on the analysis of the two human mutations p.G391D and p.M153I in *HCNI* across various mouse models, the findings from this study underscore the significant impact of these mutations on both cortical and hippocampal oscillatory dynamics, as well as on neuronal function and behavior. The investigation of GD mice revealed a pronounced reduction in gamma oscillations during REM sleep, indicative of potential deficits in GABAergic interneuron function. This was further supported by reduced firing rates in excitatory pyramidal neurons, suggesting an imbalance in the excitation-inhibition network that could contribute to spontaneous seizures observed in these mice.

The generation of GDGAD mice, which allowed for the conditional removal of the G380D mutation from inhibitory interneurons, provided critical insights into the pathophysiology underlying the epilepsy phenotype. The absence of spontaneous seizures in GDGAD mice highlights the role of GABAergic interneurons in mediating this effect, supporting the hypothesis of an interneuronopathy. Notably, despite preventing the seizure phenotype, GDGAD mice exhibited behavioral comorbidities such as reduced body weights and locomotor hyperactivity, which points towards the involvement of additional neural circuits beyond inhibitory interneuron function. Moreover, the persistent reduction in gamma oscillations in GDGAD mice suggests that the G380D mutation may lead to broader rhythmopathy, impacting the integration of neural circuits necessary for cognitive processes. These findings are similar to those observed in other neurodevelopmental and neurodegenerative disorders,

emphasizing the need to further explore the mechanisms by which the G380D mutation affects cortical rhythms and neuronal interactions.

In conclusion, these results illuminate the complex interplay between gene mutations, interneuron function, and network dynamics in the context of DEEs and associated behavioral phenotypes. Continued research into the G380D mutation's effects on both excitatory and inhibitory circuits is crucial for unraveling pathophysiological mechanisms underlying these disorders and for developing potential therapeutic strategies aimed at restoring normal neuronal function.

References

- Adaikkan, C., Joseph, J., Foustoukos, G., Wang, J., Polygalov, D., Boehringer, R., Middleton, S.J., Huang, A.J.Y., Tsai, L.-H., McHugh, T.J., 2024. Silencing CA1 pyramidal cells output reveals the role of feedback inhibition in hippocampal oscillations. *Nat. Commun.* 15, 2190. doi:10.1038/s41467-024-46478-3
- Albertson, A.J., Bohannon, A.S., Hablitz, J.J., 2017. HCN channel modulation of synaptic integration in gabaergic interneurons in malformed rat neocortex. *Front. Cell Neurosci.* 11, 109. doi:10.3389/fncel.2017.00109
- Almacellas Barbanoj, A., Graham, R.T., Maffei, B., Carpenter, J.C., Leite, M., Hoke, J., Hardjo, F., Scott-Solache, J., Chimonides, C., Schorge, S., Kullmann, D.M., Magloire, V., Lignani, G., 2024. Anti-seizure gene therapy for focal cortical dysplasia. *Brain* 147, 542–553. doi:10.1093/brain/awad387
- Anstey, N.J., Kapgal, V., Tiwari, S., Watson, T.C., Toft, A.K.H., Dando, O.R., Inkpen, F.H., Baxter, P.S., Kozić, Z., Jackson, A.D., He, X., Nawaz, M.S., Kayenaat, A., Bhattacharya, A., Wyllie, D.J.A., Chattarji, S., Wood, E.R., Hardt, O., Kind, P.C., 2022. Imbalance of flight-freeze responses and their cellular correlates in the *Nlgn3*-y rat model of autism. *Mol. Autism* 13, 34. doi:10.1186/s13229-022-00511-8
- Barker, G.R.I., Warburton, E.C., 2011. When is the hippocampus involved in recognition memory? *J. Neurosci.* 31, 10721–10731. doi:10.1523/JNEUROSCI.6413-10.2011
- Basu, J., Siegelbaum, S.A., 2015. The corticohippocampal circuit, synaptic plasticity, and memory. *Cold Spring Harb. Perspect. Biol.* 7. doi:10.1101/cshperspect.a021733
- Bender, R.A., Baram, T.Z., 2008. Hyperpolarization activated cyclic-nucleotide gated (HCN) channels in developing neuronal networks. *Prog. Neurobiol.* 86, 129–140. doi:10.1016/j.pneurobio.2008.09.007
- Bender, R.A., Kirschstein, T., Kretz, O., Brewster, A.L., Richichi, C., Rüschemschmidt, C., Shigemoto, R., Beck, H., Frotscher, M., Baram, T.Z., 2007. Localization of HCN1 channels to presynaptic compartments: novel plasticity that may contribute to hippocampal maturation. *J. Neurosci.* 27, 4697–4706. doi:10.1523/JNEUROSCI.4699-06.2007
- Bender, R.A., Soleymani, S.V., Brewster, A.L., Nguyen, S.T., Beck, H., Mathern, G.W., Baram, T.Z., 2003. Enhanced expression of a specific hyperpolarization-activated cyclic nucleotide-gated cation channel (HCN) in surviving dentate gyrus granule cells of human and experimental epileptic hippocampus. *J. Neurosci.* 23, 6826–6836. doi:10.1523/JNEUROSCI.23-17-06826.2003
- Bernard, G., Shevell, M.I., 2008. Channelopathies: a review. *Pediatr. Neurol.* 38, 73–85. doi:10.1016/j.pediatrneurol.2007.09.007
- Bleakley, L.E., McKenzie, C.E., Reid, C.A., 2023. Efficacy of antiseizure medication in a mouse model of HCN1 developmental and epileptic encephalopathy. *Epilepsia* 64, e1–e8. doi:10.1111/epi.17447

- Bleakley, L.E., McKenzie, C.E., Soh, M.S., Forster, I.C., Pinares-Garcia, P., Sedo, A., Kathirvel, A., Churilov, L., Jancovski, N., Maljevic, S., Berkovic, S.F., Scheffer, I.E., Petrou, S., Santoro, B., Reid, C.A., 2021. Cation leak underlies neuronal excitability in an HCN1 developmental and epileptic encephalopathy. *Brain* 144, 2060–2073. doi:10.1093/brain/awab145
- Blumenfeld, H., 2003. From molecules to networks: cortical/subcortical interactions in the pathophysiology of idiopathic generalized epilepsy. *Epilepsia* 44 Suppl 2, 7–15. doi:10.1046/j.1528-1157.44.s.2.2.x
- Bock, T., Buss, E.W., Lofaro, O.M., Leroy, F., Santoro, B., Siegelbaum, S.A., 2022. The HCN1 hyperpolarization-activated cyclic nucleotide-gated channel enhances evoked GABA release from parvalbumin positive interneurons. *BioRxiv*. doi:10.1101/2022.11.11.516205
- Brigo, F., Jones, K., Eltze, C., Matricardi, S., 2021. Anti-seizure medications for Lennox-Gastaut syndrome. *Cochrane Database Syst. Rev.* 4, CD003277. doi:10.1002/14651858.CD003277.pub4
- Bueno-Junior, L.S., Ruckstuhl, M.S., Lim, M.M., Watson, B.O., 2022. REM sleep has minute-scale rhythms in mice and humans: A non-binary continuum between phasic and tonic microstates. *BioRxiv*. doi:10.1101/2022.07.11.499612
- Butler, J.L., Hay, Y.A., Paulsen, O., 2018. Comparison of three gamma oscillations in the mouse entorhinal-hippocampal system. *Eur. J. Neurosci.* 48, 2795–2806. doi:10.1111/ejn.13831
- Buzsáki, G., 2002. Theta Oscillations in the Hippocampus. *Neuron* 33, 325–340.
- Buzsáki, G., Buhl, D.L., Harris, K.D., Csicsvari, J., Czeh, B., Morozov, A., 2003. Hippocampal network patterns of activity in the mouse. *Neuroscience* 116, 201–211. doi:10.1016/s0306-4522(02)00669-3
- Buzsáki, G., Wang, X.-J., 2012. Mechanisms of gamma oscillations. *Annu. Rev. Neurosci.* 35, 203–225. doi:10.1146/annurev-neuro-062111-150444
- Byron, N., Semenova, A., Sakata, S., 2021. Mutual Interactions between Brain States and Alzheimer’s Disease Pathology: A Focus on Gamma and Slow Oscillations. *Biology (Basel)* 10. doi:10.3390/biology10080707
- Catterall, W.A., 2018. Dravet syndrome: A sodium channel interneuronopathy. *Curr. Opin. Physiol.* 2, 42–50. doi:10.1016/j.cophys.2017.12.007
- Cheah, C.S., Lundstrom, B.N., Catterall, W.A., Oakley, J.C., 2019. Impairment of Sharp-Wave Ripples in a Murine Model of Dravet Syndrome. *J. Neurosci.* 39, 9251–9260. doi:10.1523/JNEUROSCI.0890-19.2019
- Chen, G., Zhang, Y., Li, X., Zhao, X., Ye, Q., Lin, Y., Tao, H.W., Rasch, M.J., Zhang, X., 2017. Distinct Inhibitory Circuits Orchestrate Cortical beta and gamma Band Oscillations. *Neuron* 96, 1403–1418.e6. doi:10.1016/j.neuron.2017.11.033

- Clancy, B., Darlington, R.B., Finlay, B.L., 2001. Translating developmental time across mammalian species. *Neuroscience* 105, 7–17. doi:10.1016/s0306-4522(01)00171-3
- Colgin, L.L., 2016. Rhythms of the hippocampal network. *Nat. Rev. Neurosci.* 17, 239–249. doi:10.1038/nrn.2016.21
- Colgin, L.L., Moser, E.I., 2010. Gamma oscillations in the hippocampus. *Physiology (Bethesda)* 25, 319–329. doi:10.1152/physiol.00021.2010
- Colmers, W.F., El Bahh, B., 2003. Neuropeptide Y and Epilepsy. *Epilepsy Curr* 3, 53–58. doi:10.1046/j.1535-7597.2003.03208.x
- Combe, C.L., Gasparini, S., 2021. Ih from synapses to networks: HCN channel functions and modulation in neurons. *Prog. Biophys. Mol. Biol.* 166, 119–132. doi:10.1016/j.pbiomolbio.2021.06.002
- Corbett, B.F., You, J.C., Zhang, X., Pyfer, M.S., Tosi, U., Iascone, D.M., Petrof, I., Hazra, A., Fu, C.H., Stephens, G.S., Ashok, A.A., Aschmies, S., Zhao, L., Nestler, E.J., Chin, J., 2017. Δ fosb regulates gene expression and cognitive dysfunction in a mouse model of Alzheimer's disease. *Cell Rep.* 20, 344–355. doi:10.1016/j.celrep.2017.06.040
- Craven, K.B., Zagotta, W.N., 2006. CNG and HCN channels: two peas, one pod. *Annu. Rev. Physiol.* 68, 375–401. doi:10.1146/annurev.physiol.68.040104.134728
- De Stasi, A.M., Farisello, P., Marcon, I., Cavallari, S., Forli, A., Vecchia, D., Losi, G., Mantegazza, M., Panzeri, S., Carmignoto, G., Bacci, A., Fellin, T., 2016. Unaltered network activity and interneuronal firing during spontaneous cortical dynamics in vivo in a mouse model of severe myoclonic epilepsy of infancy. *Cereb. Cortex* 26, 1778–1794. doi:10.1093/cercor/bhw002
- Delage, C., Taib, T., Mamma, C., Lerouet, D., Besson, V.C., 2021. Traumatic Brain Injury: An Age-Dependent View of Post-Traumatic Neuroinflammation and Its Treatment. *Pharmaceutics* 13. doi:10.3390/pharmaceutics13101624
- Depuydt, A.-S., Peigneur, S., Tytgat, J., 2022. Review: HCN channels in the heart. *Curr Cardiol Rev* 18, e040222200836. doi:10.2174/1573403X18666220204142436
- Dilena, R., Striano, P., Gennaro, E., Bassi, L., Olivotto, S., Tadini, L., Mosca, F., Barbieri, S., Zara, F., Fumagalli, M., 2017. Efficacy of sodium channel blockers in SCN2A early infantile epileptic encephalopathy. *Brain Dev.* 39, 345–348. doi:10.1016/j.braindev.2016.10.015
- Donoghue, T., Haller, M., Peterson, E.J., Varma, P., Sebastian, P., Gao, R., Noto, T., Lara, A.H., Wallis, J.D., Knight, R.T., Shestyuk, A., Voytek, B., 2020. Parameterizing neural power spectra into periodic and aperiodic components. *Nat. Neurosci.* 23, 1655–1665. doi:10.1038/s41593-020-00744-x
- Dyhrfjeld-Johnsen, J., Morgan, R.J., Soltesz, I., 2009. Double Trouble? Potential for Hyperexcitability Following Both Channelopathic up- and Downregulation of I(h) in Epilepsy. *Front. Neurosci.* 3, 25–33. doi:10.3389/neuro.01.005.2009

- Elgueta, C., Köhler, J., Bartos, M., 2015. Persistent discharges in dentate gyrus perisoma-inhibiting interneurons require hyperpolarization-activated cyclic nucleotide-gated channel activation. *J. Neurosci.* 35, 4131–4139. doi:10.1523/JNEUROSCI.3671-14.2015
- Etter, G., Carmichael, J.E., Williams, S., 2023. Linking temporal coordination of hippocampal activity to memory function. *Front. Cell Neurosci.* 17, 1233849. doi:10.3389/fncel.2023.1233849
- Fadila, S., Quinn, S., Turchetti Maia, A., Yakubovich, D., Ovadia, M., Anderson, K.L., Giladi, M., Rubinstein, M., 2020. Convulsive seizures and some behavioral comorbidities are uncoupled in the Scn1aA1783V Dravet syndrome mouse model. *Epilepsia* 61, 2289–2300. doi:10.1111/epi.16662
- Fiáth, R., Meszéna, D., Somogyvári, Z., Boda, M., Barthó, P., Ruther, P., Ulbert, I., 2021. Recording site placement on planar silicon-based probes affects signal quality in acute neuronal recordings. *Sci. Rep.* 11, 2028. doi:10.1038/s41598-021-81127-5
- Fisher, R.S., Acevedo, C., Arzimanoglou, A., Bogacz, A., Cross, J.H., Elger, C.E., Engel, J., Forsgren, L., French, J.A., Glynn, M., Hesdorffer, D.C., Lee, B.I., Mathern, G.W., Moshé, S.L., Perucca, E., Scheffer, I.E., Tomson, T., Watanabe, M., Wiebe, S., 2014. ILAE official report: a practical clinical definition of epilepsy. *Epilepsia* 55, 475–482. doi:10.1111/epi.12550
- Gasparini, S., DiFrancesco, D., 1997. Action of the hyperpolarization-activated current (I_h) blocker ZD 7288 in hippocampal CA1 neurons. *Pflugers Arch.* 435, 99–106. doi:10.1007/s004240050488
- George, A.L., 2004. Inherited Channelopathies Associated with Epilepsy. *Epilepsy Curr* 4, 65–70. doi:10.1111/j.1535-7597.2004.42010.x
- Girardeau, G., Benchenane, K., Wiener, S.I., Buzsáki, G., Zugaro, M.B., 2009. Selective suppression of hippocampal ripples impairs spatial memory. *Nat. Neurosci.* 12, 1222–1223. doi:10.1038/nn.2384
- Gorski, J.A., Talley, T., Qiu, M., Puelles, L., Rubenstein, J.L.R., Jones, K.R., 2002. Cortical excitatory neurons and glia, but not GABAergic neurons, are produced in the Emx1-expressing lineage. *J. Neurosci.* 22, 6309–6314. doi:10.1523/JNEUROSCI.22-15-06309.2002
- Härtig, W., Meinicke, A., Michalski, D., Schob, S., Jäger, C., 2022. Update on Perineuronal Net Staining With Wisteria floribunda Agglutinin (WFA). *Front Integr Neurosci* 16, 851988. doi:10.3389/fnint.2022.851988
- Hartung, J., Schroeder, A., Pérez Vázquez, R.A., Poorthuis, R.B., Letzkus, J.J., 2024. Layer 1 NDNF interneurons are specialized top-down master regulators of cortical circuits. *Cell Rep.* 43, 114212. doi:10.1016/j.celrep.2024.114212
- Hazan, L., Zugaro, M., Buzsáki, G., 2006. Klusters, NeuroScope, NDManager: a free software suite for neurophysiological data processing and visualization. *J. Neurosci. Methods* 155, 207–216. doi:10.1016/j.jneumeth.2006.01.017

- Hol, E.M., Pekny, M., 2015. Glial fibrillary acidic protein (GFAP) and the astrocyte intermediate filament system in diseases of the central nervous system. *Curr. Opin. Cell Biol.* 32, 121–130. doi:10.1016/j.ceb.2015.02.004
- Hölter, S.M., Garrett, L., Einicke, J., Sperling, B., Dirscherl, P., Zimprich, A., Fuchs, H., Gailus-Durner, V., Hrabě de Angelis, M., Wurst, W., 2015. Assessing cognition in mice. *Curr. Protoc. Mouse Biol.* 5, 331–358. doi:10.1002/9780470942390.mo150068
- Huang, Z., Li, G., Aguado, C., Lujan, R., Shah, M.M., 2017. HCN1 channels reduce the rate of exocytosis from a subset of cortical synaptic terminals. *Sci. Rep.* 7, 40257. doi:10.1038/srep40257
- Huang, Z., Lujan, R., Kadurin, I., Uebele, V.N., Renger, J.J., Dolphin, A.C., Shah, M.M., 2011. Presynaptic HCN1 channels regulate Cav3.2 activity and neurotransmission at select cortical synapses. *Nat. Neurosci.* 14, 478–486. doi:10.1038/nn.2757
- Huang, Z., Walker, M.C., Shah, M.M., 2009. Loss of dendritic HCN1 subunits enhances cortical excitability and epileptogenesis. *J. Neurosci.* 29, 10979–10988. doi:10.1523/JNEUROSCI.1531-09.2009
- Incorpora, G., 2009. Dravet syndrome. *Ital J Pediatr* 35, 27. doi:10.1186/1824-7288-35-27
- Jacobs, M.P., Leblanc, G.G., Brooks-Kayal, A., Jensen, F.E., Lowenstein, D.H., Noebels, J.L., Spencer, D.D., Swann, J.W., 2009. Curing epilepsy: progress and future directions. *Epilepsy Behav.* 14, 438–445. doi:10.1016/j.yebeh.2009.02.036
- Jayet Bray, L.C., Quoy, M., Harris, F.C., Goodman, P.H., 2010. A circuit-level model of hippocampal place field dynamics modulated by entorhinal grid and suppression-generating cells. *Front. Neural Circuits* 4, 122. doi:10.3389/fncir.2010.00122
- Jeantet, Y., Cayzac, S., Cho, Y.H., 2013. β oscillation during slow wave sleep and rapid eye movement sleep in the electroencephalogram of a transgenic mouse model of Huntington's disease. *PLoS One* 8, e79509. doi:10.1371/journal.pone.0079509
- Kann, O., 2016. The interneuron energy hypothesis: Implications for brain disease. *Neurobiol. Dis.* 90, 75–85. doi:10.1016/j.nbd.2015.08.005
- Kasemir, J., 2020. Characterization of mouse models for HCN1-associated epilepsy syndromes caused by *de novo* point mutations (HCN1 p.G380D, p.M153I and p.R590Q). Master's thesis. University of Cologne.
- Kim, J.-B., 2014. Channelopathies. *Korean J Pediatr* 57, 1–18. doi:10.3345/kjp.2014.57.1.1
- Kretschmer, F., Sajgo, S., Kretschmer, V., Badea, T.C., 2015. A system to measure the Optokinetic and Optomotor response in mice. *J. Neurosci. Methods* 256, 91–105. doi:10.1016/j.jneumeth.2015.08.007
- Kullmann, D.M., 2002. The neuronal channelopathies. *Brain* 125, 1177–1195. doi:10.1093/brain/awf130

- Lebedeva, J., Jappy, D., Nasretdinov, A., Vazetdinova, A., Krut, V., Sokolov, R., Dobryakova, Y., Eliava, M., Grinevich, V., Rozov, A., 2024. Excitatory neurons in stratum radiatum provide an alternative pathway for excitation flow that escapes perisomatic inhibition. doi:10.7554/eLife.94385.1
- Lerche, H., Shah, M., Beck, H., Noebels, J., Johnston, D., Vincent, A., 2013. Ion channels in genetic and acquired forms of epilepsy. *J. Physiol. (Lond.)* 591, 753–764. doi:10.1113/jphysiol.2012.240606
- Lopez-Pigozzi, D., Laurent, F., Brotons-Mas, J.R., Valderrama, M., Valero, M., Fernandez-Lamo, I., Cid, E., Gomez-Dominguez, D., Gal, B., Menendez de la Prida, L., 2016. Altered Oscillatory Dynamics of CA1 Parvalbumin Basket Cells during Theta-Gamma Rhythmpathies of Temporal Lobe Epilepsy. *eNeuro* 3. doi:10.1523/ENEURO.0284-16.2016
- Lörincz, A., Notomi, T., Tamás, G., Shigemoto, R., Nusser, Z., 2002. Polarized and compartment-dependent distribution of HCN1 in pyramidal cell dendrites. *Nat. Neurosci.* 5, 1185–1193. doi:10.1038/nn962
- Löscher, W., Potschka, H., Sisodiya, S.M., Vezzani, A., 2020. Drug resistance in epilepsy: clinical impact, potential mechanisms, and new innovative treatment options. *Pharmacol. Rev.* 72, 606–638. doi:10.1124/pr.120.019539
- Lüthi, A., McCormick, D.A., 1998. H-Current : Properties of a Neuronal. *Cell* 21, 9–12.
- Mao, R., Page, D.T., Merzlyak, I., Kim, C., Tecott, L.H., Janak, P.H., Rubenstein, J.L.R., Sur, M., 2009. Reduced conditioned fear response in mice that lack *Dlx1* and show subtype-specific loss of interneurons. *J. Neurodev. Disord.* 1, 224–236. doi:10.1007/s11689-009-9025-8
- Maren, S., Phan, K.L., Liberzon, I., 2013. The contextual brain: implications for fear conditioning, extinction and psychopathology. *Nat. Rev. Neurosci.* 14, 417–428. doi:10.1038/nrn3492
- Marguet, S.L., Le-Schulte, V.T.Q., Merseburg, A., Neu, A., Eichler, R., Jakovcevski, I., Ivanov, A., Hanganu-Opatz, I.L., Bernard, C., Morellini, F., Isbrandt, D., 2015. Treatment during a vulnerable developmental period rescues a genetic epilepsy. *Nat. Med.* 21, 1436–1444. doi:10.1038/nm.3987
- Marini, C., Porro, A., Rastetter, A., Dalle, C., Rivolta, I., et al., 2018. HCN1 mutation spectrum: from neonatal epileptic encephalopathy to benign generalized epilepsy and beyond. *Brain* 141, 3160–3178. doi:10.1093/brain/awy263
- Matt, L., 2010. HCN2 channels in local hippocampal inhibitory interneurons constrain temporoammonic LTP. Doctoral dissertation. Technical University Munich.
- Matthias, G., Merseburg, A., Erlenbeck-Dinkelmann, J., Boehm, J., Vogel, P., Marguet, S., Roeper, J., Isbrandt, D., 2023. Role of I(h) in the development of motor dysfunctions' ' 2023 Neuroscience Meeting Planner. Washington, D.C.: Society for Neuroscience, Program No. PSTRO65.09.

- Meisler, M.H., Kearney, J., Ottman, R., Escayg, A., 2001. Identification of epilepsy genes in human and mouse. *Annu. Rev. Genet.* 35, 567–588. doi:10.1146/annurev.genet.35.102401.091142
- Merseburg, A., Kasemir, J., Buss, E.W., Leroy, F., Bock, T., Porro, A., Barnett, A., Tröder, S.E., Engeland, B., Stockebrand, M., Moroni, A., Siegelbaum, S.A., Isbrandt, D., Santoro, B., 2022. Seizures, behavioral deficits, and adverse drug responses in two new genetic mouse models of HCN1 epileptic encephalopathy. *Elife* 11. doi:10.7554/eLife.70826
- Moosmang, S., Stieber, J., Zong, X., Biel, M., Hofmann, F., Ludwig, A., 2001. Cellular expression and functional characterization of four hyperpolarization-activated pacemaker channels in cardiac and neuronal tissues. *Eur. J. Biochem.* 268, 1646–1652. doi:10.1046/j.1432-1327.2001.02036.x
- Mottaghi, S., Kohl, S., Biemann, D., Liebana, S., Montaña Crespo, R.E., Buchholz, O., Wilson, M., Klaus, C., Uchenik, M., Munkel, C., Schmidt, R., Hofmann, U.G., 2021. Bilateral Intracranial Beta Activity During Forced and Spontaneous Movements in a 6-OHDA Hemi-PD Rat Model. *Front. Neurosci.* 15, 700672. doi:10.3389/fnins.2021.700672
- Nakahara, S., Adachi, M., Ito, H., Matsumoto, M., Tajinda, K., van Erp, T.G.M., 2018. Hippocampal pathophysiology: commonality shared by temporal lobe epilepsy and psychiatric disorders. *Neurosci. J.* 2018, 4852359. doi:10.1155/2018/4852359
- Nava, C., Dalle, C., Rastetter, A., Striano, P., de Kovel, C.G.F., Nabbout, R., Cancès, C., Ville, D., Brilstra, E.H., Gobbi, G., Raffo, E., Bouteiller, D., Marie, Y., Trouillard, O., Robbiano, A., Keren, B., Agher, D., Roze, E., Lesage, S., Nicolas, A., Brice, A., Baulac, M., Vogt, C., El Hajj, N., Schneider, E., Suls, A., Weckhuysen, S., Gormley, P., Lehesjoki, A.-E., De Jonghe, P., Helbig, I., Baulac, S., Zara, F., Koeleman, B.P.C., EuroEPINOMICS RES Consortium, Haaf, T., LeGuern, E., Depienne, C., 2014. De novo mutations in HCN1 cause early infantile epileptic encephalopathy. *Nat. Genet.* 46, 640–645. doi:10.1038/ng.2952
- Neves, G., Cooke, S.F., Bliss, T.V.P., 2008. Synaptic plasticity, memory and the hippocampus: a neural network approach to causality. *Nat. Rev. Neurosci.* 9, 65–75. doi:10.1038/nrn2303
- Noebels, J., 2017. Precision physiology and rescue of brain ion channel disorders. *J. Gen. Physiol.* 149, 533–546. doi:10.1085/jgp.201711759
- Nolan, M.F., Dudman, J.T., Dodson, P.D., Santoro, B., 2007. HCN1 channels control resting and active integrative properties of stellate cells from layer II of the entorhinal cortex. *J. Neurosci.* 27, 12440–12451. doi:10.1523/JNEUROSCI.2358-07.2007
- Nolan, M.F., Malleret, G., Lee, K.H., Gibbs, E., Dudman, J.T., Santoro, B., Yin, D., Thompson, R.F., Siegelbaum, S.A., Kandel, E.R., Morozov, A., 2003. The hyperpolarization-activated HCN1 channel is important for motor learning and neuronal integration by cerebellar Purkinje cells. *Cell* 115, 551–564. doi:10.1016/s0092-8674(03)00884-5
- Notomi, T., Shigemoto, R., 2004. Immunohistochemical localization of Ih channel subunits, HCN1-4, in the rat brain. *J. Comp. Neurol.* 471, 241–276. doi:10.1002/cne.11039

- Ottman, R., 1997. Genetic epidemiology of epilepsy. *Epidemiol Rev* 19, 120–128. doi:10.1093/oxfordjournals.epirev.a017934
- Panagiotou, M., Vyazovskiy, V.V., Meijer, J.H., Deboer, T., 2017. Differences in electroencephalographic non-rapid-eye movement sleep slow-wave characteristics between young and old mice. *Sci. Rep.* 7, 43656. doi:10.1038/srep43656
- Panthi, S., Leitch, B., 2019. The impact of silencing feed-forward parvalbumin-expressing inhibitory interneurons in the cortico-thalamocortical network on seizure generation and behaviour. *Neurobiol. Dis.* 132, 104610. doi:10.1016/j.nbd.2019.104610
- Peng, L., Martin-Vasallo, P., Sweadner, K.J., 1997. Isoforms of Na,K-ATPase alpha and beta subunits in the rat cerebellum and in granule cell cultures. *J. Neurosci.* 17, 3488–3502.
- Penttonen, M., Kamondi, A., Acsády, L., Buzsáki, G., 1998. Gamma frequency oscillation in the hippocampus of the rat: intracellular analysis in vivo. *Eur. J. Neurosci.* 10, 718–728. doi:10.1046/j.1460-9568.1998.00096.x
- Perucca, P., Perucca, E., 2019. Identifying mutations in epilepsy genes: Impact on treatment selection. *Epilepsy Res.* 152, 18–30. doi:10.1016/j.epilepsyres.2019.03.001
- Petersen, P.C., Siegle, J.H., Steinmetz, N.A., Mahallati, S., Buzsáki, G., 2021. CellExplorer: A framework for visualizing and characterizing single neurons. *Neuron* 109, 3594–3608.e2. doi:10.1016/j.neuron.2021.09.002
- Porro, A., Abbandonato, G., Veronesi, V., Russo, A., Binda, A., Antolini, L., Granata, T., Castellotti, B., Marini, C., Moroni, A., DiFrancesco, J.C., Rivolta, I., 2021. Do the functional properties of HCN1 mutants correlate with the clinical features in epileptic patients? *Prog. Biophys. Mol. Biol.* doi:10.1016/j.pbiomolbio.2021.07.008
- Raga, S., Specchio, N., Rheims, S., Wilmshurst, J.M., 2021. Developmental and epileptic encephalopathies: recognition and approaches to care. *Epileptic Disord.* 23, 40–52. doi:10.1684/epd.2021.1244
- Robinson, R.B., Siegelbaum, S.A., 2003. Hyperpolarization-activated cation currents: from molecules to physiological function. *Annu. Rev. Physiol.* 65, 453–480. doi:10.1146/annurev.physiol.65.092101.142734
- Rojas, D.C., Wilson, L.B., 2014. γ -band abnormalities as markers of autism spectrum disorders. *Biomark Med* 8, 353–368. doi:10.2217/bmm.14.15
- Roth, F.C., Hu, H., 2020. An axon-specific expression of HCN channels catalyzes fast action potential signaling in GABAergic interneurons. *Nat. Commun.* 11, 2248. doi:10.1038/s41467-020-15791-y
- Sakimoto, Y., Mizuno, J., Kida, H., Kamiya, Y., Ono, Y., Mitsushima, D., 2019. Learning Promotes Subfield-Specific Synaptic Diversity in Hippocampal CA1 Neurons. *Cereb. Cortex* 29, 2183–2195. doi:10.1093/cercor/bhz022

- Salgueiro-Pereira, A.R., Duprat, F., Pousinha, P.A., Loucif, A., Douchamps, V., Regondi, C., Ayrault, M., Eugie, M., Stunault, M.I., Escayg, A., Goutagny, R., Gnatkovsky, V., Frassoni, C., Marie, H., Bethus, I., Mantegazza, M., 2019. A two-hit story: Seizures and genetic mutation interaction sets phenotype severity in SCN1A epilepsies. *Neurobiol. Dis.* 125, 31–44. doi:10.1016/j.nbd.2019.01.006
- Santoro, B., Liu, D.T., Yao, H., Bartsch, D., Kandel, E.R., Siegelbaum, S.A., Tibbs, G.R., 1998. Identification of a gene encoding a hyperpolarization-activated pacemaker channel of brain. *Cell* 93, 717–729. doi:10.1016/s0092-8674(00)81434-8
- Santoro, B., Shah, M.M., 2020. Hyperpolarization-Activated Cyclic Nucleotide-Gated Channels as Drug Targets for Neurological Disorders. *Annu. Rev. Pharmacol. Toxicol.* 60, 109–131. doi:10.1146/annurev-pharmtox-010919-023356
- Schlingloff, D., Káli, S., Freund, T.F., Hájos, N., Gulyás, A.I., 2014. Mechanisms of sharp wave initiation and ripple generation. *J. Neurosci.* 34, 11385–11398. doi:10.1523/JNEUROSCI.0867-14.2014
- Seibenhener, M.L., Wooten, M.C., 2015. Use of the Open Field Maze to measure locomotor and anxiety-like behavior in mice. *J. Vis. Exp.* e52434. doi:10.3791/52434
- Shuman, T., Amendolara, B., Golshani, P., 2017. Theta rhythmopathy as a cause of cognitive disability in TLE. *Epilepsy Curr* 17, 107–111. doi:10.5698/1535-7511.17.2.107
- Sohal, V.S., Rubenstein, J.L.R., 2019. Excitation-inhibition balance as a framework for investigating mechanisms in neuropsychiatric disorders. *Mol. Psychiatry* 24, 1248–1257. doi:10.1038/s41380-019-0426-0
- Sohal, V.S., Zhang, F., Yizhar, O., Deisseroth, K., 2009. Parvalbumin neurons and gamma rhythms enhance cortical circuit performance. *Nature* 459, 698–702. doi:10.1038/nature07991
- Soltesz, I., Deschênes, M., 1993. Low- and high-frequency membrane potential oscillations during theta activity in CA1 and CA3 pyramidal neurons of the rat hippocampus under ketamine-xylazine anesthesia. *J. Neurophysiol.* 70, 97–116. doi:10.1152/jn.1993.70.1.97
- Southan, A.P., Morris, N.P., Stephens, G.J., Robertson, B., 2000. Hyperpolarization-activated currents in presynaptic terminals of mouse cerebellar basket cells. *J. Physiol. (Lond.)* 526 Pt 1, 91–97. doi:10.1111/j.1469-7793.2000.t01-1-00091.x
- Taniguchi, H., He, M., Wu, P., Kim, S., Paik, R., Sugino, K., Kvitsiani, D., Fu, Y., Lu, J., Lin, Y., Miyoshi, G., Shima, Y., Fishell, G., Nelson, S.B., Huang, Z.J., 2011. A resource of Cre driver lines for genetic targeting of GABAergic neurons in cerebral cortex. *Neuron* 71, 995–1013. doi:10.1016/j.neuron.2011.07.026
- Thuault, S.J., Malleret, G., Constantinople, C.M., Nicholls, R., Chen, I., Zhu, J., Panteleyev, A., Vronskaya, S., Nolan, M.F., Bruno, R., Siegelbaum, S.A., Kandel, E.R., 2013. Prefrontal cortex HCN1 channels enable intrinsic persistent neural firing and executive memory function. *J. Neurosci.* 33, 13583–13599. doi:10.1523/JNEUROSCI.2427-12.2013

- Trifonov, S., Yamashita, Y., Kase, M., Maruyama, M., Sugimoto, T., 2014. Glutamic acid decarboxylase 1 alternative splicing isoforms: characterization, expression and quantification in the mouse brain. *BMC Neurosci.* 15, 114. doi:10.1186/1471-2202-15-114
- Tröder, S.E., Ebert, L.K., Butt, L., Assenmacher, S., Schermer, B., Zevnik, B., 2018. An optimized electroporation approach for efficient CRISPR/Cas9 genome editing in murine zygotes. *PLoS One* 13, e0196891. doi:10.1371/journal.pone.0196891
- Tzilivaki, A., Tukker, J.J., Maier, N., Poirazi, P., Sammons, R.P., Schmitz, D., 2023. Hippocampal GABAergic interneurons and memory. *Neuron* 111, 3154–3175. doi:10.1016/j.neuron.2023.06.016
- Uhlhaas, P.J., Singer, W., 2010. Abnormal neural oscillations and synchrony in schizophrenia. *Nat. Rev. Neurosci.* 11, 100–113. doi:10.1038/nrn2774
- Van Erum, J., Van Dam, D., De Deyn, P.P., 2019. PTZ-induced seizures in mice require a revised Racine scale. *Epilepsy Behav.* 95, 51–55. doi:10.1016/j.yebeh.2019.02.029
- van Dorp, R., Roller, E., Deboer, T., 2024. Sleep and the sleep electroencephalogram in C57BL/6 and C3H/HeN mice. *J Sleep Res* 33, e14062. doi:10.1111/jsr.14062
- Varga, C., Oijala, M., Lish, J., Szabo, G.G., Bezair, M., Marchionni, I., Golshani, P., Soltesz, I., 2014. Functional fission of parvalbumin interneuron classes during fast network events. *Elife* 3. doi:10.7554/eLife.04006
- Wahl-Schott, C., Biel, M., 2009. HCN channels: structure, cellular regulation and physiological function. *Cell Mol. Life Sci.* 66, 470–494. doi:10.1007/s00018-008-8525-0
- Wang, W., Frankel, W.N., 2021. Overlaps, gaps, and complexities of mouse models of Developmental and Epileptic Encephalopathy. *Neurobiol. Dis.* 148, 105220. doi:10.1016/j.nbd.2020.105220
- Weber, V., 2024. Analysis of hippocampal brain morphology in a mouse model with global or cell-specific expression of the HCN1 p.G380D variant associated with developmental and epileptic encephalopathy. Bachelor's thesis. University of Cologne.
- Wierschke, S., Lehmann, T.-N., Dehnicke, C., Horn, P., Nitsch, R., Deisz, R.A., 2010. Hyperpolarization-activated cation currents in human epileptogenic neocortex. *Epilepsia* 51, 404–414. doi:10.1111/j.1528-1167.2009.02275.x
- Wiest, C., Torrecillos, F., Poghosyan, A., Bange, M., Muthuraman, M., Groppa, S., Hulse, N., Hasegawa, H., Ashkan, K., Baig, F., Morgante, F., Pereira, E.A., Mallet, N., Magill, P.J., Brown, P., Sharott, A., Tan, H., 2023. The aperiodic exponent of subthalamic field potentials reflects excitation/inhibition balance in Parkinsonism. *Elife* 12. doi:10.7554/eLife.82467
- Witter, M.P., 2007. The perforant path: projections from the entorhinal cortex to the dentate gyrus, in: *The Dentate Gyrus: A Comprehensive Guide to Structure, Function, and Clinical Implications*, Progress in Brain Research. Elsevier, pp. 43–61. doi:10.1016/S0079-6123(07)63003-9

- Yamamoto, J., Tonegawa, S., 2017. Direct medial entorhinal cortex input to hippocampal CA1 is crucial for extended quiet awake replay. *Neuron* 96, 217–227.e4. doi:10.1016/j.neuron.2017.09.017
- Yao, Y., Wu, M., Wang, L., Lin, L., Xu, J., 2020. Phase coupled firing of prefrontal parvalbumin interneuron with high frequency oscillations. *Front. Cell Neurosci.* 14, 610741. doi:10.3389/fncel.2020.610741
- Zhao, D., Pinares-Garcia, P., McKenzie, C.E., Bleakley, L.E., Forster, I.C., Wong, V.H.Y., Nguyen, C.T.O., Scheffer, I.E., Reid, C.A., Bui, B.V., 2023. Retinal dysfunction in a mouse model of HCN1 genetic epilepsy. *J. Neurosci.* 43, 2199–2209. doi:10.1523/JNEUROSCI.1615-22.2022
- Zhou, J., Brown, A.M., Lackey, E.P., Arancillo, M., Lin, T., Sillitoe, R.V., 2020. Purkinje cell neurotransmission patterns cerebellar basket cells into zonal modules defined by distinct pinceau sizes. *Elife* 9. doi:10.7554/eLife.55569
- Zuber, B., Nikonenko, I., Klauser, P., Muller, D., Dubochet, J., 2005. The mammalian central nervous synaptic cleft contains a high density of periodically organized complexes. *Proc. Natl. Acad. Sci. USA* 102, 19192–19197. doi:10.1073/pnas.0509527102

Acknowledgement

I would like to take this opportunity to thank all the people that have supported me throughout my PhD journey.

First of all, I would like to thank Prof. Dr. Johannes Vogt and Prof. Dr. Matteo Bergami for being part of my thesis committee. Over the years, during our annual meetings, your optimism about my project and your ideas on how to further investigate the study were greatly appreciated.

I want to thank Prof. Dr. Dirk Isbrandt for giving me the opportunity to work on this project. From my very first internship in 2019, I was very happy working in the lab. Thank you for your support, for giving me the chance to work with mice, and for teaching me various unique techniques that helped me grow as a scientist.

A special thank you goes to Andrea, who turned from a supervisor into a friend. You supported me through countless challenges, answered all my questions, and gave me the confidence to persevere during difficult times. Thanks for taking care of me the way you did, for guiding me through behavioral tests with mice, for continuing to help even after leaving the lab, for the wonderful first paper that we published, for your many thesis corrections, and for so much more! I could not have asked for a better supervisor – thank you!

Of course, I would also like to thank all the other members of the lab. It was a pleasure working with all you guys, and I am very grateful to have been warmly welcomed into the team.

Thanks to Bina Santoro, who facilitated and maintained a wonderful collaboration, and who played a crucial role in driving the publication of our first paper.

Last but not least, special thanks go to my family and friends. Thanks to my parents and especially to my twin sister, who by now managed to describe my project in detail, even without having any science background. Thanks to my partner, who made sure I survived this intensive time, always knowing when I needed a break and gently encouraging me when I needed to push forward. And to all my friends, thank you for your constant support over the years!

Statutory Declaration

Ich versichere, dass ich die von mir vorgelegte Dissertation selbstständig angefertigt, die benutzten Quellen und Hilfsmittel vollständig angegeben und die Stellen der Arbeit – einschließlich Tabellen, Karten und Abbildungen –, die anderen Werken im Wortlaut oder dem Sinn nach entnommen sind, in jedem Einzelfall als Entlehnung kenntlich gemacht habe; dass diese Dissertation noch keiner anderen Fakultät oder Universität zur Prüfung vorgelegen hat; dass sie – abgesehen von unten angegebenen Teilpublikationen – noch nicht veröffentlicht worden ist sowie, dass ich eine solche Veröffentlichung vor Abschluss des Promotionsverfahrens nicht vornehmen werde. Die Bestimmungen dieser Promotionsordnung sind mir bekannt. Die von mir vorgelegte Dissertation ist von Prof. Dr. Dirk Isbrandt betreut worden.

Ich versichere, dass ich alle Angaben wahrheitsgemäß nach bestem Wissen und Gewissen gemacht habe und verpflichte mich, jedmögliche, die obigen Angaben betreffenden Veränderungen, dem Promotionsausschuss unverzüglich mitzuteilen.

.....

Datum

.....

Unterschrift

Curriculum Vitae

Practical experiences

DZNE / University of Cologne – RG Isbrandt	04/2020 – 01/2021
Research assistant in Experimental Neurophysiology	
DZNE / University of Cologne – RG Isbrandt	11/2019 – 02/2020
Internship in Experimental Neurophysiology	
Université de Montréal, Canada – RG Dubuc	06/2019 – 08/2019
Internship in Neuroscience	
DZNE / University of Cologne – RG Isbrandt	03/2019 – 05/2019
Internship in Experimental Neurophysiology	

Education

DZNE / University of Cologne – RG Isbrandt	02/2021 – 12/2024
Research assistant, PhD student	
University of Cologne, Mat-Nat Faculty	04/2018 – 09/2020
Master of Biological Science , 9 th Sept 2020 (final grade 1.5)	
University of Cologne, Mat-Nat Faculty	10/2014 – 03/2018
Bachelor of Science, Biology , 8 th March 2018 (final grade 2.3)	
Bodelschwingh-Gymnasium Herchen, Windeck	08/2005 – 06/2013
University Entrance Qualification , 29 th June 2013 (final grade 2.4)	

Publications

- Merseburg A, Kasemir J, ..., Santoro B (2022). Seizures, behavioral deficits and adverse drug responses in two new genetic mouse models of HCN1 epileptic encephalopathy. **eLife**, 11.
- Ryczko D, ..., Kasemir J, ..., Dubuc R (2020). Descending Dopaminergic Inputs to Reticulospinal Neurons Promote Locomotor Movements. **J Neurosci**. 40(44):8478-8490.

Certification

Statistics For Experimental Life Scientists	02/2024
Poster Design	07/2023
Advanced Scientific Writing	07/2023
Best Poster Presentation (IPMM Days 2023)	05/2023
Research Ethics and Theory of Science	02/2022
FELASA-B	11/2019